EDITORIAL BOARD

Editor-in-Chief
V.P. Melnikov, Full Member of Russian Academy of Sciences

Associate chief editor
V.M. Kotlyakov, Full Member of Russian Academy of Sciences

Executive secretary
V.E. Tumskoy

Editors:

J. Brown, professor (USA); *A.V. Brouchkov*, professor; *A.A. Vasiliev*; *P. Williams*, professor (UK); *M.L. Vladov*, professor; *M.N. Grigoriev*; *D.S. Drozdov*, professor; *V.A. Istomin*, professor; *M.V. Kirov*; *I.N. Modin*, professor; *A.N. Nesterov*; *E.-M. Pfeiffer*, professor (Germany); *V.E. Romanovsky*, professor (USA); *G.L. Stenchikov*, professor (Saudi Arabia); *K. Flaate*, professor (Norway); *S. Harris*, professor (Canada); *H. Hubberten*, professor (Germany); *N.I. Shiklomanov*, professor (USA); *Yu.L. Shur*, professor (USA); *I.N. Esau*, professor (Norway)

Councilors:

V.R. Alekseev, professor; *F.E. Are*, professor; *A.D. Duchkov*, professor; *M.N. Zheleznyak*; *Yu.D. Zykov*, professor; *N.S. Kasimov*, Full Member of RAS; *I.A. Komarov*, professor; *F.M. Rivkin*; *E.M. Rivkina*; *E.A. Slagoda*; *A.V. Soromotin*; *V.T. Trofimov*, professor; *L.N. Khrustalev*, professor; *V.G. Cheverev*; *G.A. Cherkashev*

Editorial Office of *Earth's Cryosphere (Kriosfera Zemli)*
Institute of Geography, Russian Academy of Sciences
37 Vavilov St., office 22, Moscow, 117312, Russia
Editorial staff: *N.V. Arutyunyan, N.G. Belova, O.M. Lisitsyna, G.E. Oblogov*
Phone: +7(985) 957-10-01, e-mail: kriozem@gmail.com
Editor of the English translation: *D.E. Konyushkov*

Journal promoted by
Russian Academy of Sciences, Siberian Branch, Novosibirsk
Earth's Cryosphere Institute, Tyumen Scientific Centre SB RAS, Tyumen
Melnikov Permafrost Institute, SB RAS, Yakutsk

Editorial Manager *M.A. Trashkeeva*
Designed by *N.F. Suranova*
Typeset by *N.M. Raizvikh*

RUSSIAN ACADEMY OF SCIENCES
SIBERIAN BRANCH
EARTH'S CRYOSPHERE INSTITUTE, TYUMEN SCIENTIFIC CENTRE
MELNIKOV PERMAFROST INSTITUTE

EARTH'S CRYOSPHERE
SCIENTIFIC JOURNAL

Founded in January 1997	6 issues per year	Vol. XXVI, No. 5	September–October 2022

CONTENTS

PHYSICAL AND CHEMICAL PROCESSES IN FROZEN GROUND AND ICE

Shavlov A.V., Yakovenko A.A., Yakovenko E.S. Experimental studies and a new model of the Workman–Reynolds freezing potential 3

SURFACE AND GROUND WATERS IN TERRESTRIAL PERMAFROST REGION

Iudina (Kurovskaia) V.A., Chernomorets S.S., Krylenko I.N., Vinogradova T.A., Krylenko I.V., Savernyuk E.A., Gulomaydarov A.G., Zikillobekov I.I., Pirmamadov U.R., Raimbekov Yu.Kh. Assessment of possible consequences of outburst floods: case study of the Bodomdara River valley (Tajikistan) 12

CRYOGENIC PHENOMENA IN SEAS AND OCEANS

May R.I., Ganieva K.R., Topaj A.G., Yulin A.V. Frequency of occurrence of fast ice calculated from polygons of digitized ice charts using the example of the Kara Sea 25

GASES AND GAS HYDRATES IN THE EARTH'S CRYOSPHERE

Zadorozhnaya N.A., Oblogov G.E., Vasiliev A.A., Streletskaya I.D., Malkova G.V., Semenov P.B., Vanshtein B.G. Methane in frozen and thawing sediments of Western Russian Arctic 35

SNOW COVER AND GLACIERS

Mavlyudov B.R. Superimposed ice on the Bellingshausen dome, King George island, Antarctica. 48

CHRONICLE

Lytkin V.M., Pavlova M.R., Shaposhnikov G.I., Vasilieva A.N., Galanina I.A. Aleksey Aleksandrovich Galanin (*February 25, 1969 – September 8, 2002*) 61

Copyright © 2022 Siberian Branch of the RAS
Copyright © 2022 Earth's Cryosphere Institute,
Tyumen Scientific Centre SB RAS
Copyright © 2022 Melnikov Permafrost Institute, SB RAS

EARTH'S CRYOSPHERE
SCIENTIFIC JOURNAL

Earth's Cryosphere, 2022, vol. XXVI, No. 5, pp. 3–11

PHYSICAL AND CHEMICAL PROCESSES IN FROZEN GROUND AND ICE

EXPERIMENTAL STUDIES AND A NEW MODEL OF THE WORKMAN–REYNOLDS FREEZING POTENTIAL

A.V. Shavlov[1,*], A.A. Yakovenko[2], E.S. Yakovenko[2]

[1] *Earth Cryosphere Institute, Siberian Branch of the Russian Academy of Sciences,*
Malygina St. 86, Tyumen, 625000 Russia
[2] *Tyumen Industrial University, Volodarskogo St. 38, Tyumen, 625000 Russia*

**Corresponding author; e-mail: shavlov@ikz.ru*

New experimental data have been obtained on the Workman–Reynolds freezing potential of water and the electric current from an external source through the ice melting front. We propose a new model of the phenomenon that considers capturing the protons and hydroxide ions by interstitials of the ice lattice serving as charge traps. The model provides a semiquantitative explanation of the observed features of the phenomenon.

Keywords: *Workman–Reynolds freezing potential, crystallization rate, melting, proton, interstitial, electrical breakdown.*

Recommended citation: Shavlov A.V., Yakovenko A.A., Yakovenko E.S., 2022. Experimental studies and a new model of the Workman–Reynolds freezing potential. Earth's Cryosphere **26** (5), 3–11.

INTRODUCTION

The Workman–Reynolds electric freezing potential appears at the ice/water interface while freezing of pure water or diluted aqueous solutions [*Workman, Reynolds, 1950*]. This phenomenon was discovered more than a half-century ago and still arouses unrelenting interest among researchers in fundamental and applied sciences. In terms of fundamental science, it is a challenge to find out the mechanism of the freezing potential at the molecular level. The solution to this problem would strengthen the development of applied sciences searching for the connection of this phenomenon, for example, with the origin of lightning electricity [*Workman, Reynolds, 1950; Pruppacher et al., 1968; Orville, 2001*] or with the acceleration of chemical reactions while freezing of the solutions [*Sergeev, Batyuk, 1978; Moskovits, Ozin, 1979; Kazakov, Lotnik, 1987*]. In geocryology, possible relationship between the Workman–Reynolds potentials and the observed acceleration of corrosion of metal constructions and structures in contact with ice and permafrost is considered [*Hanley, 1985; Shavlov et al., 2006; Velikotskiy, 2010*]. The possibility of accelerating water migration and increasing frost heaving intensity are also associated with the Workman–Reynolds potentials [*Korkina, 1965; Yarkin, 1982*]. The latter is consistent with the experimentally established fact of frost heaving intensification within an external electric field [*Novikova, 1985*]. Thus, the interest of scientists to investigate the mechanism of freezing potential is substantiated by the importance of solving applied problems.

Let us consider the main physical characteristics of the Workman–Reynolds freezing potential. It reaches maximum values of ~10^2 V for pure water and diluted aqueous solutions with concentrations of $<10^{-4}$ M and pH 6.8, which is close to the pH of pure water [*Kachurin et al., 1967*]. While freezing of the distilled water, the ice becomes positively charged with respect to water. Depending on the time after the crystallization start, the potential increases from zero to maximum value within ~10^2 s and then slowly decreases [*Wilson, Haymet, 2008a,b, 2010; Haymet, Wilson, 2017*]. Depending on the crystallization rate, the potential passes through its maximum at the rate of ~10^{-5} m/s [*Kachurin et al., 1967; Melnikova, 1969*]. The thickness of charged ice layer adjacent to the crystallization front is ~10^{-3} m [*Cobb, 1964; LeFebre, 1967; Mel'nikova, 1969; Rozental', Chetin, 1974*]. Almost all of the electric potential change between ice and solution is concentrated exactly within this layer. The thickness of charged layer ahead of the crystallization front in solution does not exceed several molecular layers [*Melnikova, 1969*]. The contribution of this layer to the freezing potential is insignificant. With the opposite direction of the phase transformation (ice melting), interfacial potentials are not observed [*Rozental', Chetin, 1974*].

Different models have been proposed for the physical explanation of the freezing potential origin. A popular one is the ionic model [*Chernov, Melnikova, 1971a,b*], based on the unequal capture of cations and anions of the initial solution by growing ice. In this

Copyright © 2022 A.V. Shavlov, A.A. Yakovenko, E.S. Yakovenko, All rights reserved.

model, the main potential drop by about 1 V was reached in the ice phase. In the solution, the potential drop was an order of magnitude smaller. The crystallization potential weakly depended on the impurity concentration, distribution coefficients of anions and cations, and did not depend on the crystallization rate. Since the freezing potential reaches maximal values in the pure water and diluted aqueous solutions, a model based on the own charge carriers of water and ice – protons and hydroxide ions – was proposed [*Kachurin, 1970*]. Potential difference (10–10^2 V) between water and ice was created by unhindered penetration of protons into the solid phase. A model of the phenomenon on its own charge carriers was also proposed [*Rozental', Chetin, 1974*]. It was supposed that protons and hydroxide ions come from the liquid phase to the crystallization front due to Brownian motion and are irrevocably captured by ice. Since the Brownian velocity of protons is higher than that of hydroxide ions, ice acquires a positive electrical charge relative to water.

The mechanism of charge separation, which includes, in addition to protons and hydroxide ions, also own charge carriers – orientational defects – was considered in [*Shavlov, 2005*]. Recall that orientational defects are formed at energetically unfavorable orientations of water molecules with respect to one another [*Eisenberg, Kauzmann, 1969*]. A positively charged *D*-type orientational defect corresponds to an orientation when two protons are located on the line connecting two neighboring oxygen atoms, and a negatively charged *L*-type defect corresponds to a situation where there is not a single proton on the line. A one proton on the line is a no-defect state. According to the model proposed in that work, protons and hydroxide ions, as well as orientational defects, are partially rejected by the crystallization front and accumulate in the liquid phase. The accumulation process depends on the distribution coefficients and diffusion coefficients of charge carriers and leads to interfacial electrification. This model can explain the sign and magnitude of freezing potentials ~10^2 V in the pure water but cannot correctly describe the thickness of the charged layer in ice and the time it takes to reach the maximum potential after the onset of crystallization. The model gives too low values of these parameters – 10^{-5} m and 1 s, respectively, while the observed values are 10^{-3} m и 10^2 s.

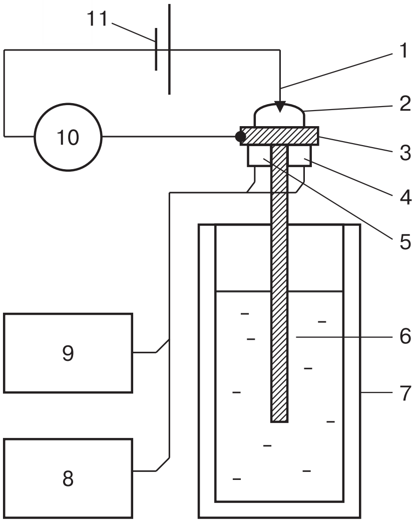

Fig. 1. Experimental setup for measuring the freezing potential of water and current from an external source through the water/ice interface.

(1) Upper electrode, (2) water drop, (3) lower electrode, (4) thermal sensor, (5) heater, (6) cold rod, (7) Dewar vessel with liquid nitrogen, (8) power supply for the heater, (9) temperature recording unit, (10) electrometer, (11) galvanic cell.

Note that all of the above models are described by nonlinear electro-diffusion equations with the corresponding boundary conditions at the crystallization front, and their solutions are found by numerical methods. Although the freezing potential has been studied by many researchers, there are no convincing models to date to describe its occurrence [*Ozeki et al., 1991, 1992; Haymet, Wilson, 2017*]. Further experimental studies and new physical models are therefore required. This work aims to solve these tasks.

NEW EXPERIMENTAL DATA ON THE WORKMAN–REYNOLDS POTENTIAL

In this section, we present our new experimental data on the freezing potential for the pure water and data on the electrical conductivity of the water/ice interface (in the direction perpendicular to the boundary plane) while melting of ice. These data can be useful for establishing a new physical model of water freezing potential.

Authors observed the freezing potential while freezing a drop of bidistilled water using the facility shown on Fig. 1. We placed the drop of ~5 mm in diameter at the electrode 3. The electrode was in thermal contact with the upper end of the cold metal rod 6. The lower end of the metal rod was lowered into a Dewar vessel with liquid nitrogen 7. Thermal sensor 4 and electric heater 5 were fixed on the metal rod. The thermal sensor, together with the temperature recording unit 9, allowed determination of the electrode temperature with an error of ±1 K. An electric heater with power supply 8 provided heating or cooling of the electrode at a rate of ~0.5 K/s. Electrode 3, as well as the upper thin-wire electrode 1 touching the water drop, were connected to an electrometer. In the voltage measurement mode, the input resistance of the electrometer was 10^{12} Ohm (this is a typical value of the input resistance in experiments on Workman–Reynolds potentials described in the literature). It did not significantly shunt the freezing potential of the drop. In the current measurement mode, the input resistance of the electrometer was many times less than the internal resistance of a water drop, which in our experiments was no less than $2 \cdot 10^5$ Ohm. The current in the circuit was excited by a galvanic cell 11 with a voltage of 7.5 V. In the experiments, the freezing front of the drop (or the melting front) was located approximately parallel to the electrode surface 3.

The typical temperature dependence of the freezing potential of a drop during cooling of the lower electrode at a rate of 0.5 K/s is shown on Fig. 2. The drop has been freezing during 3–5 s from the beginning of the crystallization. The difference in potentials between ice and water was also observed for 3–5 s and reached 10–20 V. Ice was positively charged. In Fig. 2, we also show the temperature dependence of the drop melting potential with the rise in temperature. It was close to zero.

Figure 3 shows the temperature dependence of current from an external source during freezing and melting of a drop. This current has nothing to do with the freezing or melting current that occurs when an external circuit is closed in the absence of an external source. The figure shows that the current from an external source flowing through the drop slowly decreases with decreasing temperature, then sharply tends to zero when the drop freezes and its electrical conductivity decreases. While heating the frozen drop, the current increases abruptly at the moment of its melting, then quickly decreases several times, tending to the initial value of the current in water. The freeze–thaw cycle with little changing result can be repeated many times.

Note that the results of the authors' experiments with freezing potentials differ slightly in magnitude and sign of the potentials from the results described in the literature and reflected in the Introduction section. New here are the data on the current from an external source through the drop during freezing and melting. These data indicate that mobile charge carriers in ice – protons, hydroxide ions, and orientational defects – are captured by traps and remain in the trapped state for a long time during freezing. Upon melting, they are released from the traps and give an increase in the current until their concentration decreases to a thermodynamically equilibrium value due to recombination. Since the electrical conductivity of pure water is controlled by protons and hydroxide ions, and orientational defects play an auxiliary role, the concentration of traps should exceed the equilibrium concentration of protons and hydroxide ions in water, which is approximately equal to 10^{20} m^{-3} [*Eisenberg, Kauzmann, 1969*]. Only in this case can a surge of current be observed in the experiment (passage of the current through a maximum) during melting. The concentration value of 10^{20} m^{-3} can easily be obtained using the pH value of pure water (6.8) by applying equation $N[\text{mol/L}] = 10^{-\text{pH}}$. It is important to consider the presence of such charge traps in ice in the new numerical model of the phenomenon.

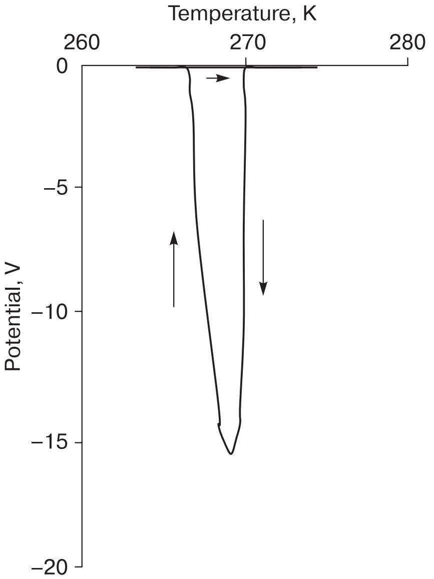

Fig. 2. Thermal dependence between the freezing potential at cooling conditions and melting potential at heating conditions of a drop.

Temperature change rate is 0.5 K/s. Arrows indicate the direction of temperature change in the experiment.

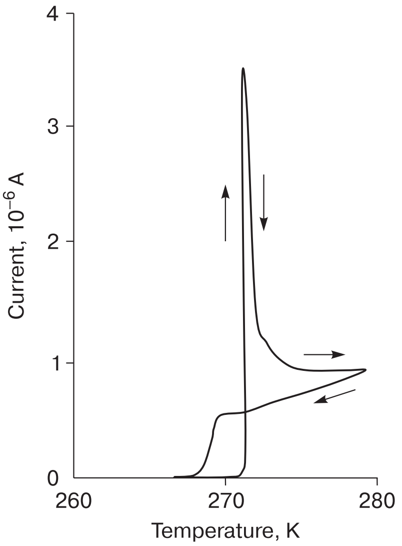

Fig. 3. Temperature dependence of the current from an external source during freezing and melting of a drop.

Temperature change rate is 0.5 K/s.

NEW MODEL OF THE WORKMAN–REYNOLDS POTENTIALS

In this study, we deal with the freezing potential of pure bidistilled water. Therefore, we do not consider ions of chemical impurities as participants in interfacial charge separation during crystallization. Obviously, ions of chemical impurities are present in water and ice in residual (uncontrolled) amounts, but their concentration is several orders of magnitude lower than the concentration of intrinsic ice lattice defects (up to 10^{-5}–10^{-4} M) capable of capturing an electric charge and participating in interfacial electrical processes. The role of such intrinsic lattice defects must be analyzed first.

Own slow-moving defects of the ice lattice – interstitials and vacancies – can claim to be charge traps in ice made from pure water. An estimate of the concentration of interstitials in ice at a temperature close to the melting point is $N_I = 10^{23}$ m^{-3} (10^{-4} M) [*Hondon et al., 1987*]. The concentration of vacancies is considered to be several orders of magnitude lower. For comparison, the concentration of mobile orientational defects in ice is $N_{D,L} = 10^{22}$ m^{-3}, the concentration of protons and hydroxide ions $N_{\mathrm{H,OH}} = 10^{17}$ m^{-3} [*Eisenberg, Kauzmann, 1969*]. In [*Koning, Antonelli, 2008; Truffer, 2013*] concentration of interstitials $N_I = 3{\cdot}10^{22}$ m^{-3}; the concentration of vacancies $N_V = 3{\cdot}10^{17}$ m^{-3}. Thus, interstitials are the most numerous inherent slow-moving defects of the ice lattice and therefore they are more suitable for the role of charge traps in ice than other defects.

The process of accumulating the electrical charge by traps can be as follows. Let us assume that charge traps (lattice interstitials) are formed together with ice in the course of water crystallization. Then, these traps capture protons and form positively charged complexes. The possibility of the formation of such complexes was shown in [*Koning, Antonelli, 2008*]. Let us estimate the time of filling the traps with protons. In the physical sense [*Ryvkin, 1963*], the time equals $\tau_{\mathrm{H}} = (\upsilon_{\mathrm{H}}\,\sigma_{\mathrm{H}}\,N_{\mathrm{H}})^{-1} = 0.3$ s, where $\upsilon_{\mathrm{H}} = 10^3$ m/s is the thermal velocity of the proton, $\sigma_{\mathrm{H}} = 3{\cdot}10^{-20}$ m^2 is the capture cross section comparable to that of a water molecule. Further, positively charged traps can capture negatively charged hydroxide ions. The trap filling time is $\tau_{\mathrm{OH}} = (\upsilon_{\mathrm{OH}}\,\sigma_{\mathrm{OH}}\,N_{\mathrm{OH}})^{-1} = 30$ s, where $\upsilon_{\mathrm{OH}} = 10$ m/s is the thermal velocity of the hydroxide ion (it is 10^2 times less than the proton velocity, because the diffusion coefficients of these particles differ by the same factor [*Eisenberg, Kauzmann, 1969*]), $\sigma_{\mathrm{OH}} = 3{\cdot}10^{-20}$ m^2 is the hydroxide ion capture cross section. We assume that the proton and hydroxide ion captured by the trap cannot recombine with one another. The traps can also capture charged orientational D- and L-defects, which also do not recombine with one another. The time of filling the traps with D- and L-defects is relatively short and amounts to $\tau_{D,L} = 10^{-2}$ s. It is quite probable that the traps already contain D- and L-defects by the time they are filled with protons and hydroxide ions. We assume that the traps that have captured a proton and a hydroxide ion, as well as a pair of orientational defects, become inactive with respect to subsequent captures of particles. Based on this, we conclude that ice is positively charged while its growing for the time τ_{OH} after the beginning of crystallization.

The thickness of the charged layer is $l_{\mathrm{OH}} = \upsilon\tau_{\mathrm{OH}}$, where υ is the linear crystallization rate. Ice layers separated from the front by a distance exceeding l_{OH}, are electrically neutral. To ensure the overall electrical neutrality of the crystallizing medium, the water layer ahead of the front of crystallization must carry a negative charge. It must contain an increased amount of hydroxide ions.

Let us formulate the model of the phenomenon mathematically. The space charge of ice during crystallization is mainly formed by trapped protons and hydroxide ions, and the contribution of orientational defects is small due to small values of $\tau_{D,L}$ and the small thickness of the layer charged by them, accordingly. Therefore, we will consider protons, hydroxide ions, and traps in the model, without considering orientational defects. The energy model of protons and hydroxide ions in water and ice is explained in Fig. 4. In ice, the energy of free protons and hydroxide ions is indicated by numbers 1 and 4, respectively. They are formed in pairs due to thermal ionization of water molecules. The pair formation energy is 0.98 eV. Protons and hydroxide ions can be trapped at energy levels 2 and 3, respectively. Capture processes are indicated by arrows. Reverse thermally activated transitions from the trapped to the free state are unlikely. We will not consider them. In water, the energies of free protons and hydroxide ions are indicated by numbers 6 and 5, respectively. The energy of pair formation is ~0.5 eV. To transfer protons and hydroxide ions from water to ice, it is necessary to overcome the energy barrier. Therefore, both these and other charge carriers are largely rejected by ice during crystallization and accumulate in water.

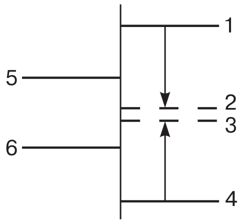

Fig. 4. Energy model of protons and hydroxide ions.

In ice: 1 and 4 are the energies of the free proton and hydroxide ion, respectively; 2 and 3 are the energies of the proton and hydroxide ion captured by the trap, respectively. In water: 5 and 6 are the energies of the free hydroxide ion and proton, respectively.

In ice, numerous traps charged with trapped protons and hydroxide ions give the main contribution to the electrical neutrality equation. The contribution of free protons and hydroxide ions is small because of their low concentration. In addition, the volumetric charge of free protons and hydroxide ions can be concentrated near the crystallization front in a narrow layer with a thickness equal to the carrier diffusion length $(D_H\tau_R)^{0.5} = 10^{-5}$ m, where $D_H = 2\cdot10^{-7}$ m^2/s, $\tau_R = 7\cdot10^{-4}$ s are diffusion coefficient and proton recombination time in ice, respectively [*Eisenberg, Kauzmann, 1969*]. The thickness of the layer with charged traps is presumably 10^2 times higher. Therefore, the contribution of free protons and hydroxide ions to the volumetric charge of ice can be neglected. We assume that their concentration is equal to the equilibrium concentration $N_H = N_{OH} = 10^{17}$ m^{-3}.

Let us obtain equations and find analytical solutions for the concentrations of trapped protons p and hydroxide ions n at energy levels 2 and 3, respectively. For this, we use the continuity equation. For example, for p:

$$\frac{\partial p}{\partial t} = -\mathrm{div}\left(j_p\right) + \gamma_H N_H \left(S-p\right) = -\mathrm{div}\left(j_p\right) + \frac{S-p}{\tau_H}, \quad (1)$$

where $j_p = vp$ is the flux of traps with captured protons (diffusion and electric current are absent); $\gamma_H = v_H\sigma_H$ is the coefficient of proton capture by traps; S is the concentration of traps; and v is the linear crystallization rate. The second term on the right side of (1) describes the profit of protons at level 2 due to capture from level 1. This profit is proportional to the concentration of free protons N_H at level 1 and the concentration of empty traps $(S-p)$ at level 2. From (1) we obtain in the stationary case:

$$\begin{gathered} \frac{\partial p}{\partial t} = -v\frac{\partial p}{\partial x} + \gamma_H N_H \left(S-p\right) = 0, \\ \frac{dp}{dx} = -\frac{\gamma_H N_H}{v}\left(p-S\right). \end{gathered} \quad (2)$$

The solution of Eq. (2) at a boundary condition $p\big|_{x=0} = 0$ is as follows:

$$p = S\left(1-\exp\left(-\frac{x}{l_H}\right)\right),$$

where $l_H = \dfrac{v}{\gamma_H N_H}$.

We obtain a similar solution for the concentration n of hydroxide ions captured by traps:

$$n = S\left(1-\exp\left(-\frac{x}{l_{OH}}\right)\right),$$

where $l_{OH} = \dfrac{v}{\gamma_{OH} N_{OH}}$.

Using the Poisson equation $\dfrac{dE}{dx} = \dfrac{e}{\varepsilon_I\varepsilon_0}\left(p-n\right)$, we determine the field E and the potential U in ice at boundary conditions $E\big|_{x=\infty} = 0$, $U\big|_{x=0} = 0$, where ε_I is dielectric permittivity of ice, ε_0 is electrical constant, and e is the elementary charge.

$$E = \frac{eS}{\varepsilon_I\varepsilon_0}\left(l_{OH}\exp\left(-\frac{x}{l_{OH}}\right) - l_H\exp\left(-\frac{x}{l_H}\right)\right); \quad (3)$$

$$U = \frac{eS}{\varepsilon_I\varepsilon_0}\left(l_{OH}^2\left(1-\exp\left(-\frac{x}{l_{OH}}\right)\right) - l_H^2\left(1-\exp\left(-\frac{x}{l_H}\right)\right)\right). \quad (4)$$

Further, to ensure the overall electrical neutrality of the system in water, many nonequilibrium hydroxide ions are concentrated, compensating for the charge of ice. They are concentrated in the layer equal in thickness to the diffusion length. Diffusion length in water equals to $(D_{OH}\tau_R)^{0.5} = 10^{-6}$ m, where $D_{OH} = 7\cdot10^{-9}$ m^2/s, $\tau_R = 7\cdot10^{-5}$ s are the diffusion coefficient and recombination time of hydroxide ions, respectively [*Eisenberg, Kauzmann, 1969*].

The field strength in water near the crystallization front is equal to $E_W\big|_{x=-0} = E\big|_{x=0}\dfrac{\varepsilon_I}{\varepsilon_W}$, where ε_W is dielectric permittivity of water. The potential drop is $U_W = E_W\big|_{x=-0}\left(D_{OH}\tau_R\right)^{0.5}$. For example, the potential drop will not exceed a few fractions of a Volt at the maximum value of the electric field strength in water, equal to the breakdown value $E_W = 5\cdot10^7$ V/m [*Korobeynikov, 2000*]. Thus, it should be expected that the main contribution to the freezing potential will be made by the space charge of ice, while the contribution of the space charge of water will be insignificant.

DISCUSSION

To calculate the freezing potential, we used the following values of the charge carrier's parameters in ice: concentrations of protons and hydroxide ions $N_H = N_{OH} = 10^{17}$ m^{-3}, concentration of traps $S = 10^{22}$ m^{-3}, capture coefficients $\gamma_H = 3\cdot10^{-17}$ m^3/s, $\gamma_{OH} = 3\cdot10^{-19}$ m^3/s, dielectric permittivity $\varepsilon_I = 10^4$. The value of the ice dielectric permittivity should be discussed separately. The permittivity of ice is known [*Noll, 1978*] to be depended on the frequency of the electric field (Fig. 5). The traditionally mentioned value of the permittivity $\varepsilon_I = 10^2$ is valid for the kilohertz frequency range. The phenomenon of freezing potential generation considered here lies in a different frequency range of about 10^{-1} to 10^{-2} Hz (the time for the freezing potential to reach its maximum value is tens to hundreds of seconds). In this range, the dielectric permittivity of ice is a hundred times

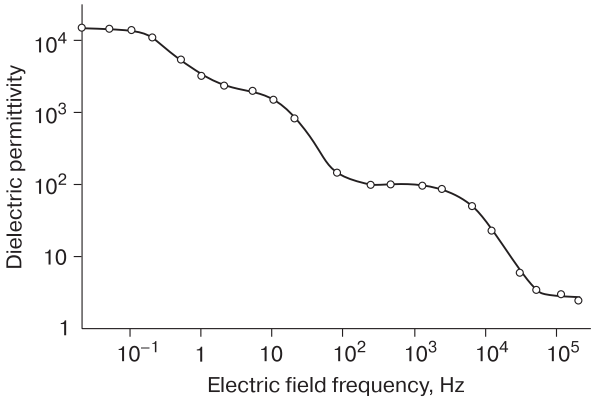

Fig. 5. Dependence between the dielectric permittivity of ice at –3 °C and the electric field frequency [*Noll, 1978*].

higher, i.e., $\varepsilon_I = 10^4$. A value close to this, $\varepsilon_I = 5{\cdot}10^4$, was obtained in the freezing potential study in the work [*Kachurin, Grigorov, 1977*]. Note that the above-discussed time of trap filling with hydroxide ions was several tens of seconds. It is quite possible that the polarization of traps (lattice interstitials) with protons, hydroxide ions, and orientational defects bound to them is responsible for the high values of the permittivity of ice at low frequencies.

Figure 6 shows the dependences of the concentration of protons captured by traps p, hydroxide ions n, and the volume charge density $(p-n)$ in ice (in units of elementary charge) on the distance x to the crystallization front at a crystallization rate often used in experiments $v = 10^{-5}$ m/s. At low distance from the front $x < 10^{-6}$ m, traps are free of charge carriers and electrically neutral, at 10^{-6} m $< x < 10^{-3}$ m traps are filled with protons and thus positively charged, at $x > 10^{-3}$ m they are filled with protons and hydroxide ions and are electrically neutral again.

Figure 7 shows the behavior of the electric field strength E and the freezing potential U with increasing distance x from the crystallization front at crystallization rate $v = 10^{-5}$ m/s. The field strength decreases from $6{\cdot}10^6$ V/m to zero at a distance of 10^{-3} m from the front. The freezing potential increases at this distance from zero to $2{\cdot}10^3$ V and then remains unchanged as x increases.

From Figs. 6 and 7 it can be concluded that space electric charge in ice is concentrated near the phase front in a layer of ice with a thickness of 10^{-3} m (at $v = 10^{-5}$ m/s); in the same layer, the freezing potential increases to the maximum value. Further, the graph of the potential in Fig. 6 could be plotted not depending on the distance x to the front but depending on the time $t = x/v$ from the beginning of crystallization. Then, we would see that the freezing potential reaches its maximum value in 10^2 s after the onset of crystallization. We obtain that the thickness of the charged ice layer is 10^{-3} m, the time for the potential to reach its maximum value of 10^2 s, and the large potential value of 10^3 V are in satisfactory agreement with the experiments described in the Introduction.

We note that the field strength in ice near the crystallization front is $6{\cdot}10^6$ V/m. From this value, it is easy to calculate the field strength in water near the phase front. It will be $\varepsilon_I/\varepsilon_W = 10^2$ times higher than in ice, that is $6{\cdot}10^8$ V/m. This value is an order of magnitude higher than the breakdown value of the field strength in water equal to $5{\cdot}10^7$ V/m. Thus, electrical breakdown can take place in water near the crystallization front. This conclusion can explain why the crystallization front is a source of pulsed electromagnetic radiation, as well as acoustic radiation, as it was found in experiments described in [*Kachurin et al.,*

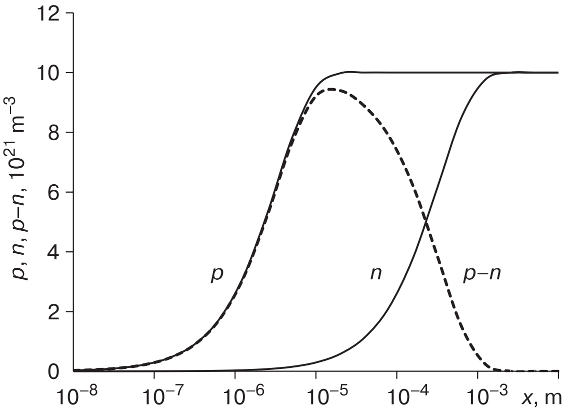

Fig. 6. Concentration of protons (p) and hydroxide-ions (n) captured by traps, and the density of space charge ($p-n$) in ice depending on the distance (x) to the crystallization front at crystallization rate $v = 10^{-5}$ m/s.

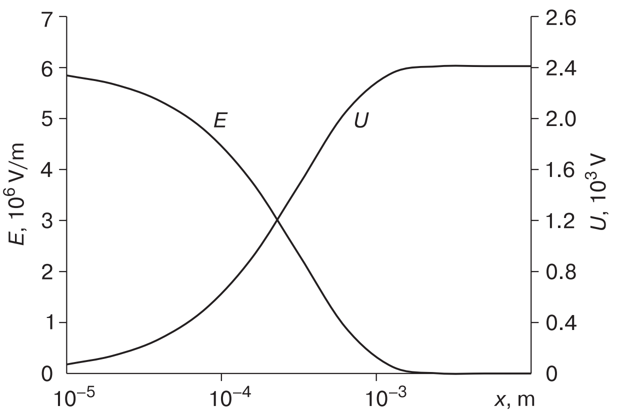

Fig. 7. Dependence of electrical field (E) and freezing potential (U) on the distance (x) to the crystallization front at crystallization rate $v = 10^{-5}$ m/s.

1982; Shibkov et al., 2002]. Electromagnetic radiation of the megahertz range was observed in the form of packets of oscillations (as in pulsed discharges) with the frequency of packets rapidly increasing with an increase in the freezing potential (up to 10 packets per second at a freezing potential of 10^2 V). Note that the authors of the cited papers have also associated electromagnetic and acoustic radiation with electric discharges in ice between crack edges due to ice cracking, but not in water. The weak point in this hypothesis seems to be precisely ice cracking, since this process requires orders of magnitude higher freezing rates [*Trokhan et al., 1984*] than in experiments on the study of Workman–Reynolds potentials.

For electrical breakdown in water, the following concepts are currently developed, such as described in [*Korobeynikov, 2000*]. Ionization processes (partial discharges according to the Paschen's Law) arise on air bubbles that previously existed in the water under the action of a breakdown electric field. After the discharge, the field in the bubble decreases due to screening of the external field by the charges deposited on the bubble walls. This causes weakening or termination of ionization processes in the bubble. The action of the field on the settled charge leads to the motion of the bubble wall and the elongation of the bubble along the field. As a result, the voltage in the bubble increases, which leads to a repeated partial discharge and the movement of a new wave of charges. This model of electrical breakdown in a liquid makes it possible to semiquantitatively explain almost all experimental dependences of the breakdown strength: on pressure, temperature, viscosity, and on the duration of the acting electrical pulse.

Fluctuations in the size of gas bubbles in a liquid during electrical breakdown, apparently, are the cause of the acoustic emission that accompanies the occurrence of freezing potentials. Density fluctuations in a thin water layer near the crystallization front were confirmed experimentally [*Bilgram et al., 1978; Bilgram, 1982*]. According to these papers, the intensity of the light scattered by the crystallization front increases sharply relative to the background value, when the crystallization rate exceeds 10^{-6} m/s. Further, a sharp increase is replaced by a more gradual increase in the intensity of scattered light with further growth of the rate of crystallization (Fig. 8). As the crystallization rate decreases from the maximum value in the experiment to zero, the scattering intensity decreases monotonously to the background value. Apparently, the electric field strength in water reaches a threshold value at a crystallization rate of 10^{-6} m/s and electrical breakdown occurs for the first time.

If we check the value of the field from Eq. (3) at crystallization rate of 10^{-6} m/s, we obtain the field strength in ice $6{\cdot}10^5$ V/m. Then, the field strength in water will be 10^2 times higher $6{\cdot}10^7$ V/m – the breakdown value of the electric field strength for water. This estimate is quite good. Here the question arises: why the intensity of light scattering does not decrease abruptly to the background value, but decreases monotonously as the crystallization rate decreases? Apparently, this happens because the electric strength of water decreases as the time of water exposure to electric discharges increases [*Korobeynikov, 2000*].

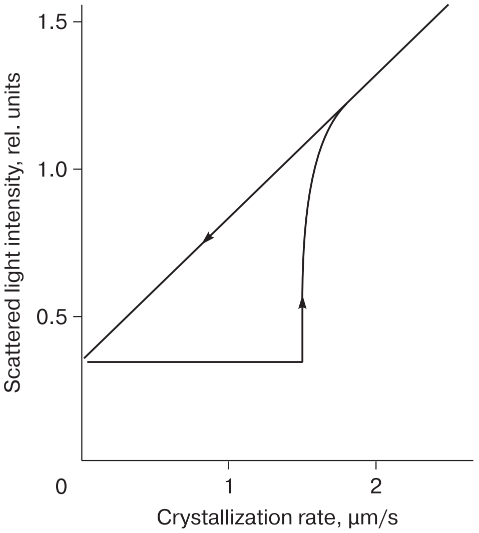

Fig. 8. Dependence between the intensity of light scattered by crystallization front and the crystallization rate [*Bilgram et al., 1978*].

Let us consider another issue formulated in the paper [*Haymet, Wilson, 2017*]. Why the freezing potential does not remain unchanged over time having reached its maximum after the onset of crystallization, but begins to slowly decrease, while the crystallization rate remains approximately constant? The time for half-reducing the potential is 15–20 min. The decrease in the crystallization potential with time can also be explained (within the framework of the model proposed here) using the idea of the existence of an electrical breakdown of water ahead of the crystallization front. During the breakdown of water, dissociation products corresponding to the phenomenon – ionized water molecules and electrons that are transformed into a hydrated state – are formed. They accumulate ahead of the front over time. They can partially be captured by the growing ice; another part is rejected by the front. Electrons are smaller and more easily embedded into the solid phase. In ice, electrons can form complexes with free protons, lowering their equilibrium concentration. Due to the ionic equilibrium ($N_{\mathrm{H}}N_{\mathrm{OH}}$ = const), the concentration of free hydroxide ions will increase (shift of the chemical equilibrium towards the alkaline side), and, as a result, the freezing potential will decrease. This can be shown using Eq. (4). According to this equation, the potential aside from the front is equal to

$$U = \frac{eS}{\varepsilon_I \varepsilon_0} \frac{v^2}{\gamma_{OH}^2 N_{OH}^2}.$$

To decrease the freezing potential by half, the concentration of free hydroxide ions N_{OH} should increase by 1.4 times. The dependence of the freezing potential on the crystallization rate with a maximum at the rate of 10^{-5} m/s can also be explained by the accumulation of electrical breakdown products of water and the shift of chemical equilibrium in ice to the alkaline side, which is more pronounced at rates of more than 10^{-5} m/s. For the formation of a maximum, it is necessary that the concentration of N_{OH} hydroxide ions grows slightly faster at $v > 10^{-5}$ m/s than the crystallization rate v.

Note that in the proposed model the authors do not consider the presence of ions of chemical impurities. This is permissible, if their concentration is much less than the concentration of intrinsic defects – interstitials with a concentration of 10^{-5}–10^{-4} M. At a high concentration of ions of chemical impurities, their contribution to interfacial electrical processes can no longer be neglected, and the model must be developed further.

CONCLUSIONS

We briefly summarize the results achieved in this work.

We have obtained a new experimental data on the Workman–Reynolds freezing potentials and the electric current through the water-ice interface in distilled water.

We propose a new freezing potential model based on charge accumulation by traps in ice, which can be represented by interstitials – intrinsic defects of the ice lattice. The proposed model can partially quantitatively and qualitatively describe most of the features of the phenomenon listed in the Introduction section. The model can also explain the new experimental data on the increase in electric current during ice melting. This is related to ceasing of the trapping of electric charges by the interstitials and ice turning into ordinary water molecules while melting. In this case, released are protons, hydroxide ions, and orientational defects associated with them are released. During the relaxation time, they all contribute to the increase in electrical conductivity up to values exceeding equilibrium ones.

The model of the Workman–Reynolds phenomenon considered by the authors can initiate further experimental studies of electrical processes during freezing of water. It can also serve as a further development of applied research, i.e., to advance understanding of the mechanisms of chemical reactions' acceleration at the crystallization front of solutions. This is important for improving the technologies of non-destructive storage of food, biological objects, and drugs in a frozen state. The model can also be useful for understanding the mechanism and improving the technology of reducing the rate of metal structure corrosion in contact with ice.

References

Bilgram J.H., 1982. Die Dynamik des Gefrierens. *Naturwissenschaften* **69**, 472–478 (in German).

Bilgram J.H., Guttinger H., Kanzig W., 1978. Fluctuations of the ice-water interface during solidification. *Phys Rev. Lett.* **40** (21), 1394–1397.

Chernov A.A., Melnikova A.M., 1971a. Theory of electrical phenomena accompanying crystallization. I. Electric field in a crystallizing water solution of electrolyte. *Crystallografiya* **16**, 477–487 (in Russian).

Chernov A.A., Melnikova A.M., 1971b. Theory of electrical phenomena accompanying crystallization. II. Potential difference between phases during crystallization of ice and naphthalene. *Crystallografiya* **16**, 488–491 (in Russian).

Cobb A.W., 1964. *Interfacial Electrical Effects Observed during the Freezing of Water. Unpublished Report*. New Mexico Institute of Mining and Technology, Socorro, New Mexico.

Eisenberg D., Kauzmann W., 1969. *The Structure and Properties of Water*. New York, Oxford Univ. Press, 280 pp.

Hanley T.O.D., 1985. Electrical freezing potentials and corrosion rates in clay sludge. *Can. Geotech.* **22**, 599–604.

Haymet A.D.J., Wilson P.W., 2017. TheWorkman–Reynolds "Freezing Potential": A new look at the inherent physical process.*J. Molecular Liquids* **228**, 243–246.

Hondon T., Azuma K., Higashi A., 1987. Self-interstitials in ice. *J. de Physique* **48** (3), 183–187.

Kachurin L.G., 1970. Electrokinetic phenomena arising during the crystallization of liquids. *Electrokhimiya* **6** (9), 1294–1299 (in Russian).

Kachurin L.G., Bekryayev V.I., Psalomshchikov V.F., 1967. Experimental study of the electrokinetic phenomenon arising during the crystallization of aqueous solutions. *Dokl. Akad. Nauk SSSR* (Moscow) **174** (5), 1122–1130 (in Russian).

Kachurin L.G., Grigorov N.O., 1977. Electro-crystallization potentials and permittivity of aqueous solutions. *Zh. Fizich. Khimii* **51** (11), 2864–2868 (in Russian).

Kachurin L.G., Kolev S., Psalomshchikov V.F., 1982. Pulsed radio emission arising from the crystallization of water and some dielectrics. *Dokl. Akad. Nauk SSSR* (Moscow), **267**, 347–350 (in Russian).

Kazakov V.P., Lotnik S.V., 1987. *Low-Temperature Chemiluminescence*. Moscow, Nauka, 176 pp. (in Russian).

Koning M., Antonelli A., 2008. Modeling equilibrium concentrations of Bjerrum and molecular point defects and their complexes in ice.*J. Chem. Phys.* **128**, 164502.

Korkina R.I., 1965. Electric potentials in freezing solutions and their influence on migration. In: *Processes of Heat and Mass Transfer in Frozen Rocks*. Moscow, Izd. Akad. Nauk SSSR, pp. 35–39 (in Russian).

Korobeynikov S.M., 2000. *Dielectric materials. Textbook*. Novosibirsk, Izd. Novosibirsk Gos. Univ., 66 pp. (in Russian).

LeFebre V., 1967. The freezing potential effect.*J. Colloid Interface Sci.* **25** (2), 263.

Mel'nikova A.M., 1969. Separation of charges during crystallization. *Kristallografiya* **14** (3), 548–563 (in Russian).

Moskovits M., Ozin G., 1979. *Cryochemistry*. Moscow, Mir, 594 pp. (in Russian).

Noll G., 1978. The influence of the rate of deformation on the electrical properties of ice monocrystals. *J. Glaciol.* **21** (85), 277–289.

Novikova E.V., 1985. On the method of studying the effect of an electric field on cryogenic migration in finely dispersed soils. In: *Methods for Studying Seasonally Freezing and Frozen Soils*. Moscow, Stroyizdat, pp. 9–13 (in Russian).

Orville R., 2001. *Glossary of Meteorology*. – http://www.met.tamu.edu/personnel/faculty/orville/Glossary.htm (13 Mar. 2001).

Ozeki S., Sashida N., Kakei K., Suzuki T., Kaneko K., 1991. Fine-structure of freezing potential of aqueous lithium-chloride solutions and its oscillation due to trace ethanol. *Langmuir* **7**, 821–823.

Ozeki S., Sashida N., Samata T., Kaneko K., 1992. Oscillation of the freezing potential of aqueous lithium-chloride solutions containing ethanol. *J. Chem. Soc. Faraday Trans.* **88**, 2511–2516.

Pruppacher H.R., Steinberger E.H., Wang T.L., 1968. On the electrical effects that accompany the spontaneous growth of ice in supercooled aqueous solutions. *J. Geophys. Res.* **73**, 571–584.

Rozental' O.M., Chetin F.Ye., 1974. *Multilayer Structural Ordering in Heterogeneous Processes of Ice Formation*. Sverdlovsk, Izd. Gos. Pedag. Inst., 134 pp. (in Russian).

Ryvkin S.M., 1963. *Photoelectric Phenomena in Semiconductors*. Moscow, Fizmatlit, 494 pp. (in Russian).

Sergeev G.B., Batyuk V.A., 1978. *Cryochemistry*. Moscow, Khimiya, 296 pp. (in Russian).

Shavlov A.V., 2005. Electric potential of crystallization of water and solutions. The role of protons and orientation defects. *Zh. Fizich. Khimii* **79** (8), 1626–1630 (in Russian).

Shavlov A.V., Pisarev A.D., Ryabtseva A.A., 2006. Dynamics of electrical conductivity of metal films in ice during its structural transformation. Recombination-proton mechanism of corrosion acceleration. *Kriosfera Zemli* **10** (3), 42–48 (in Russian).

Shibkov A.A., Golovin Yu.I., Zheltov M.A., Korolev A.A., Leonov A.A., 2002. In situ monitoring of growth of ice from supercooled water by a new electromagnetic method. *J. Crystal Growth* **236**, 434–440.

Trokhan A.M., Lapshin A.I., Gudzenko O.I., 1984. Cryoluminescence of liquids. *Dokl. Akad. Nauk SSSR* **275** (1), 83–86 (in Russian).

Truffer M., 2013. *Ice Physics*. Fairbanks, USA, University of Alaska, 120 pp.

Velikotskiy M.A., 2010. Corrosion activity of soils in various natural zones. *Byull. Mosk. Gos. Univ. Ser. 5. Geogr.*, no. 1, 21–27 (in Russian).

Wilson P.W., Haymet A.D.J., 2008a. Workman–Reynolds freezing potential measurements between ice and dilute salt solutions for single ice crystal faces. *J. Phys. Chem.* **112** (37), 15260–15261.

Wilson P.W., Haymet A.D.J., 2008b. New measurements of the Workman Reynolds Freezing Potential between ice and dilute salt solutions for single ice crystal faces. *J. Phys. Chem. B*. **112** (37), 11750–11755.

Wilson P.W., Haymet A.D.J., 2010. The effect of ice growth rate on the measured Workman-Reynolds freezing potential between ice and dilute NaCl solutions. *J. Phys. Chem. B*. **114** (39), 12585–12588.

Workman E.J., Reynolds S.E., 1950. Electrical phenomena occurring during freezing of dilute aqueous solutions, and their possible relationship to thunderstorm activity. *Phys. Rev.* **78**, 254–259.

Yarkin I.G., 1982. Soil polarization during freezing and its relationship with water migration and frost heaving. In: *Proc. Research Institute of Foundations and Underground Structures*. Issue. 75. Moscow, Stroyizdat, pp. 53–59 (in Russian).

Received August 3, 2021
Revised June 26, 2022
Accepted September 20, 2022

Translated by Yu.A. Dvornikov

EARTH'S CRYOSPHERE
SCIENTIFIC JOURNAL

Earth's Cryosphere, 2022, vol. XXVI, No. 5, pp. 12–24

SURFACE AND GROUND WATERS IN TERRESTRIAL PERMAFROST REGION

ASSESSMENT OF POSSIBLE CONSEQUENCES OF OUTBURST FLOODS: CASE STUDY OF THE BODOMDARA RIVER VALLEY (TAJIKISTAN)

V.A. Iudina (Kurovskaia)[1,*], S.S. Chernomorets[1], I.N. Krylenko[1,2], T.A. Vinogradova[3], I.V. Krylenko[1], E.A. Savernyuk[1], A.G. Gulomaydarov[4], I.I. Zikillobekov[4], U.R. Pirmamadov[4], Yu.Kh. Raimbekov[4]

[1] *Lomonosov Moscow State University, Faculty of Geography, Leninskie Gory 1, Moscow, 119991 Russia*
[2] *Water Problems Institute, Russian Academy of Sciences, Gubkina St. 3, Moscow, 119333 Russia*
[3] *Research and Production Association Gidrotekhproekt LLC, Oktyabr'skaya St. 55a, Valdai, Novgorod oblast, 175400 Russia*
[4] *Branch of the Aga Khan Agency for Habitat in the Republic of Tajikistan, Rudaki Ave. 34, Dushanbe, 737450 Tajikistan*

**Corresponding author; e-mail: viktoriiakurovskaia@gmail.com*

The prerequisites and modeling of possible outburst floods in the valley of the Bodomdara River (Tajikistan) are considered using detailed field data. According to the route survey results, Upper Bodomdara Lake is a supraglacial lake, which assumes possibility of its outburst leading to a cascade outburst flood. The depression of Lower Bodomdara Lake is relatively stable, and its outburst is possible without cascade flooding at anomalously high temperatures, upon snowmelt combined with extreme rainfall. Two probable scenarios are considered: (I) the outburst of Lower Bodomdara Lake (its volume comprised 328,000 m^3 according to the bathymetric survey of 2020) and (II) the cascade outburst flood of Upper Bodomdara Lake (700,000 m^3). Digital elevation model (DEM) ALOS PALSAR (12.5 m) and DEM based on images from an unmanned aerial vehicle for the Bodomdara River alluvial fan were used for predicting flood consequences. The outburst flood hydrographs for scenarios I and II were obtained using the lake outburst model developed by Yu.B. Vinogradov and an empirical formula, respectively. The material increment was estimated in the transport-shift model of debris flow formation. The resulting hydrograph was applied for zoning the Bodomdara and Shakhdara river valleys with a total length of 75 km based on the FLO-2D model. According to the modeling, the maximum water discharge at the top of the alluvial cone of the Bodomdara River will reach 143 m^3/s under scenario I and 348 m^3/s under scenario II.

Keywords: *outburst floods, debris flows, transport-shift model, FLO-2D model, model of lake outburst, Tajikistan.*

Recommended citation: Iudina (Kurovskaia) V.A., Chernomorets S.S., Krylenko I.N., Vinogradova T.A., Krylenko I.V., Savernyuk E.A., Gulomaydarov A.G., Zikillobekov I.I., Pirmamadov U.R., Raimbekov Yu.Kh., 2022. Assessment of possible consequences of outburst floods: case study of the Bodomdara River valley (Tajikistan). *Earth's Cryosphere* **26** (5), 12–24.

INTRODUCTION

Climate change leads to the degradation of mountain glaciation in Central Asia [*Jansky et al., 2009; Mergili et al., 2011; Wang et al., 2013; Harrison et al., 2018*]. The retreat of glaciers in the Pamir Mountains is mainly associated with an increase in air temperature [*Glazyrin et al., 2018*]. There are 6730 glaciers on the Pamir territory with a total area of 7493 km^2 [*Kotlyakov et al., 2011*]. In the eastern Pamir, glaciers revealed a tendency to accelerate melting from the late 1970s to 2001; the area of glaciers decreased by 7.8% in 1978–1990 and by 11.6% in 1990–2001 [*Khromova et al., 2006, 2014*]. The retreat of glaciers leads to the formation of glacial lakes.

Identification of potentially outburst-prone lakes is carried out using remote sensing data and route surveys [*Kääb et al., 2005; Quincey et al., 2007*]. The inventory of lakes in the upper reaches of the Amu Darya River on the basis of satellite images showed the presence of 1642 lakes, including 652 glacial lakes; 73% of all lakes are located above 4000 m asl. A tendency for a shift in the area of active growth of glacial lakes from the southwestern Pamir to the central and northern Pamir was also noted [*Mergili et al., 2013*]. According to the analysis of satellite images in 2007, 172 glacial lakes existed in the basins of the Gunt and Shakhdara rivers in the southwestern Pamir [*Mergili, Schneider, 2011*]. Most of them are located at 4400–4700 m asl and have been formed or at least significantly increased in size since 1968. The retreat of almost all glaciers and the growth of glacial lakes are observed in the southwestern Pamir [*Mergili, Schneider, 2011*]. In 2018, more than 600 mountain lakes were discovered in the Gunt River basin using multispectral images; most of them had been

Copyright © 2022 V.A. Iudina (Kurovskaia), S.S. Chernomorets, I.N. Krylenko, T.A. Vinogradova, I.V. Krylenko, E.A. Savernyuk, A.G. Gulomaydarov, I.I. Zikillobekov, U.R. Pirmamadov, Yu.Kh. Raimbekov, All rights reserved.

formed in recent decades [*Kidyaeva et al., 2020*]. A catalog of mountain lakes of the Gunt River basin with indication of their areas and genetic type of lake depressions was created. A strong outburst flood followed by a debris flow in the Pamir occurred in 2002 in the valley of the Dasht River [*Mergili et al., 2011*]. It was caused by the outburst of a thermokarst lake through underground flow channels. The area of the lake before the outburst was estimated at 37,000 m^2; according to other estimate [*Dokukin et al., 2020*], it reached 44,600 m^2).

As glacial lakes are located, as a rule, in hard-to-reach areas without systematic observations, it is quite difficult to predict outbursts. One of the ways to assess the risks associated with the outbursts of glacial lakes is mathematical modeling. If a glacial lake is located in the upper reaches of a river with a significant slope of its course, and if there is a sufficient amount of coarse-grained material in the bottom of the valley and on the adjacent slopes, the outburst of the lake is accompanied by debris flows with enormous destructive force. The complexity of the formation and movement of debris flows necessitated the development of a large number of mathematical models [*Hutter et al., 1994; Jan, Shen, 1997; Mikhailov, 2011*]. In various publications, models based on the equation of motion of a viscous fluid are often used to calculate debris flows. Hydrodynamic models are based on the solution of the Navier–Stokes equations of motion of a viscous fluid in explicit form or in the depth-integrated hydraulic form – the Saint-Venant equations of motion. According to [*Mikhailov, Chernomorets, 2011*], the FLO-2D hydrodynamic model is one of the most common in scientific research [*Cesca, d'Agostino, 2008; Mergili et al., 2011; Petrakov et al., 2012; Wu et al., 2013*]. Also, many models use a single-phase approach (similar to the Voellmy avalanche method), for example, the RAMMS (Rapid Mass Movements) model. The hydraulic model proposed by Voellmy does not take into account shear deformations [*Voellmy, 1995*]. In our study, a transport-shift model of debris flow formation was used to estimate the increment of material in a debris flow source [*Vinogradov, 1980; Vinogradov, Vinogradova, 2010*].

The aim of this study was to assess potential flooding zones in the valleys of the Bodomdara and Shakhdara rivers based on detailed field data using a set of mathematical models.

RESEARCH AREA

The research area includes Upper and Lower Bodomdara lakes located in the valley of the Darmaidovan River (Fig. 1), a large left tributary of the Bodomdara River.

The Bodomdara River flows into the Shakhdara River 49.5 km above the confluence of the latter with the Gunt River near the city of Khorog, the administrative center of the Gorno-Badakhshan Autonomous Region, Tajikistan. The length of the Darmaidovan River is 12 km [*Surface..., 1967*], and its catchment area is 65.6 km^2. The Darmaidovan River basin is elongated; its length is about 14 km, and the maximum width (in the middle part) is up to 5.5 km. The length of the Bodomdara River from the source of its left component Lyadzhvardara River is 27 km; the basin area is 318 km^2. The area of open glaciers in the studied part of the valley (without the Lyadzhvardara River basin) as estimated for August 11, 2020 was 6.66 km^2, and the total area of water reservoirs was 0.2 km^2. The length of the Shakhdara River is 142 km, the basin area is 4180 km^2.

In the upper reaches of the Darmaidovan River, the valley is composed of hornblende and biotite-hornblende gneiss with marble interlayers of the Yamchin formation; in the middle reaches, rocks of the Garmchashmin formation consist of biotite, sillimanite, and kyanite gneisses and migmatites predominate; in the lower reaches, granite-biotite gneisses of the Ptups formation occur.

According to the leading exogenous relief-forming processes in the valley of the Darmaidovan River, the following characteristic areas are quite clearly distinguished: a glacial moraine complex in the upper reaches of the valley (glaciers and sources); a section of moraine deposits in the upper part of the trough valley; a section of a stepped riverbed in the middle and lower parts of the valley; an estuary step; and an estuary section with sediment accumulation (with a superposed debris cone).

The mouth of the Darmaidovan River is located in the center of a flattened widening of the Bodomdara River valley with a length of about 1.2 km and a width of 100–160 m; the bottom of the valley is completely filled with alluvial deposits. At 600 m downstream, the slopes of the Bodomdara valley become noticeably higher on a step of the debris cone formed by right tributary. Further downstream toward the debris cone near the confluence with the Shakhdara River, the riverbed has a steplike profile. The average slope of the Bodomdara River downstream the Darmaidovan River is about 0.03.

The averaged longitudinal profile of the Darmaidovan riverbed is close to the slope of the bottom of the trough valley. The Darmaidovan River flows along the base of the right slope of a deep V-, sometimes U-shaped valley, between moraine deposits on the left bank and talus cones on the right bank. The width of the torrential flow in summer is 6–8 m increasing to 8–12 m in the lower reaches; the flow depth is about several dozens of centimeters with a maximum of about 1 m. In narrow parts, the river flow occupies the full bottom of the valley (6–7 to 10–15 m in width). Channel deformations are limited; the river channel is slightly curvy or straight, with numerous rapids and waterfalls. The bends of the

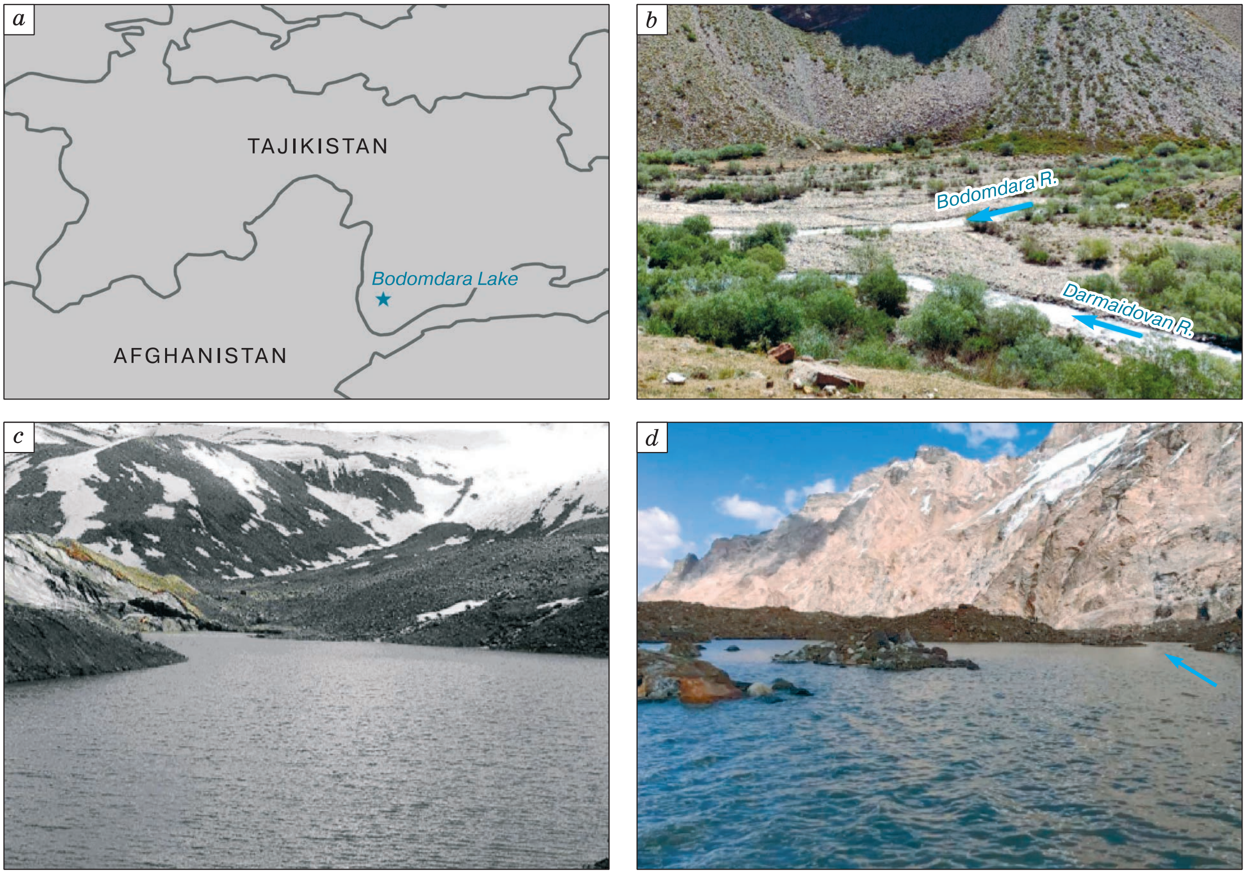

Fig. 1. Layout of the Bodomdara lakes:

(*a*) location of the Bodomdara lakes; (*b*) widening of the Bodomdara River valley at the junction with the Darmaidovan River (13.2 km upstream from the Bodomdara River mouth); (*c*) Upper Bodomdara Lake, a view of the southern part of the reservoir from the northwestern shore; (*d*) Lower Bodomdara Lake, a view of the lowering at the source of the lake (indicated by the blue arrow) from the southwest.

channel are determined due to the impact of large debris cones in the mouths of tributaries or talus cones at the footslopes.

A specific characteristic of the Darmaidovan River as present is the absence of indications of debris flows. The slopes and bottom of the channel are overloaded with loose not rounded talus material; the vegetation cover with moss pillows in the middle reaches is traced directly to the water edge (Fig. 2), old-aged and low forest stands occupy widenings of

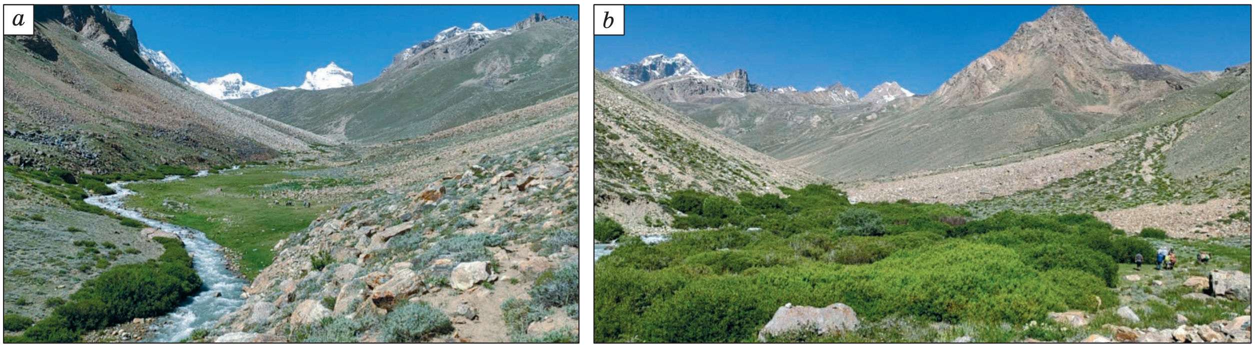

Fig. 2. Widenings of the bottom of the Darmaidovan River valley:

(*a*) 8 km upstream from the mouth, (*b*) 6.4 km upstream from the mouth; flattened area is completely overgrown with old stunted forest. In the distance, on the left slope, high moraine terraces and tributary valleys with rock bars in the lower reaches are seen.

the valley bottom in the lower reaches, and there are no characteristic debris flow-shaped landforms (U-shaped cuts, debris flow levee, terraces, etc.). There is no debris cone extended into the Bodomdara River valley in the mouth of the Darmaidovan River.

Glacial-moraine complex and lakes. A comparison of the positions the edges of active ice tongues on satellite images of 2008 and 2020 (Fig. 3) attests to their retreat by 50–120 m over 12 year; thus, the rate of retreat was up to 10 m/yr). The edge of the glacial-moraine complex is stable, but the ice wall above the river source has also retreated by 35–40 m (3 m/yr).

Lakes in the Darmaidovan River valley are located inside the glacial-moraine complex (Fig. 3), closer to the left side of the valley. These lakes are of different ages. Lower Bodomdara Lake appeared no later than in the last quarter of the 20th century; it is mentioned in the report of a tourist group that visited the valley in 1974. However, it is not mentioned in the description of the territory during a field survey of the Darmaidovan valley (up to the glacier) by P.N. Luknitsky performed on August 12, 1931 [*Luknitsky, 1955*].

According to the KH-9 satellite image from August 13, 1975 [*https://earthexplorer.usgs.gov*] the area of Lower Bodomdara Lake was 20,000 m^2, i.e., 2.6 times smaller than in 2020. According to the topographic map on a scale of 1:100 000 [*J-42-108 (Roshtkala), 1988*] fixing the situation for 1978–1984, the configuration of the lake resembled its modern configuration in that time.

Upper Bodomdara Lake appeared in the recent decade; it is absent on the satellite image obtained in August 2008, when only separate depressions with water existed in this area (Fig. 3). According to Landsat 7 image from August 20, 2010 [*https://earthexplorer.usgs.gov*], several large depressions that appeared in 2005 merged together, and the length of the lake reached 300 m. Since that time, the lake began rapidly increase in size; in 2020, its area was 56,100 m^2. Presumably, Upper Bodomdara Lake is the supraglacial lake, and glacier ice is still preserved under its bed. The lake is released from the ice cover for a short time at the end of July – the beginning of August and becomes covered with ice at the end of September.

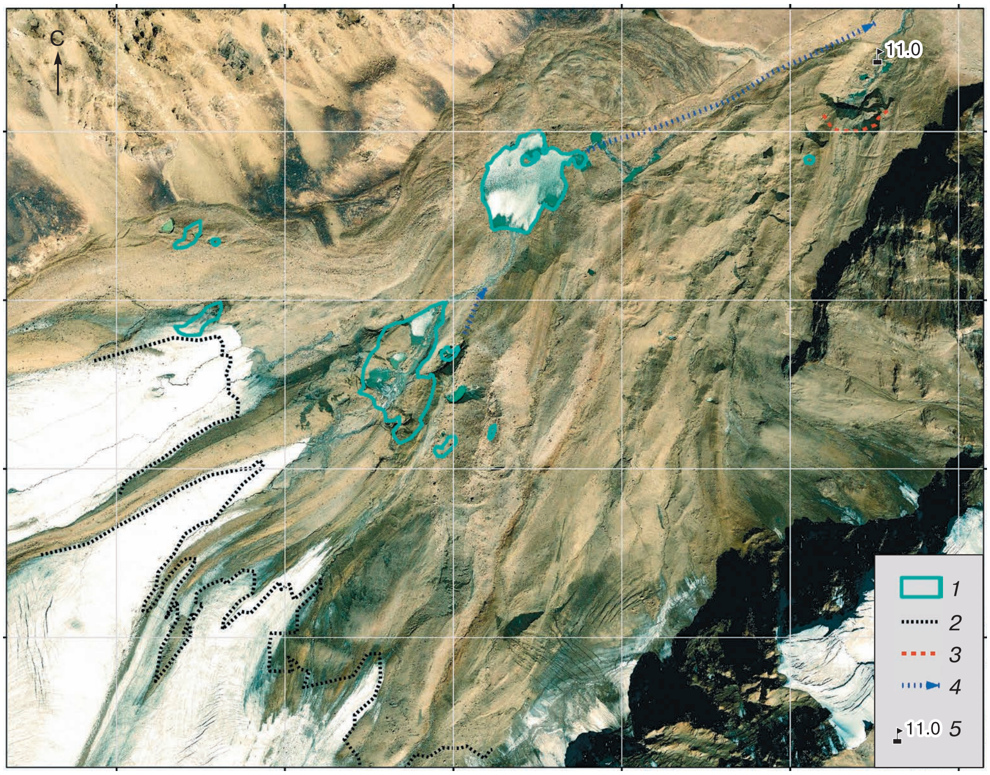

Fig. 3. The layout of lakes on the glacial-moraine complex in the upper valley of the Darmaidovan River (satellite image, August 2008).

(*1*) boundaries of lakes and ephemeral reservoirs on June 11, 2020; (*2*) edge of pure ice (active glaciers) on August 11, 2020; (*3*) edge of the ice wall at the source of the river on August 11, 2020; (*4*) the most likely ways of passing a possible outburst flood; and (*5*) distance from the mouth of the Darmaidovan River. The size of coordinate grid cell is 500 × 500 m.

Table 1. **Morphometric characteristics of the Bodomdara glacial lakes according to the bathymetric survey on July 30, 2020 (Lower Lake) and Sentinel-2B image for August 11, 2020 [*https://apps.sentinel-hub.com/eo-browser/*] (Upper Lake)**

Lake	Abs. height, m	Water area, m^2	Length along long axis, m	Max width, m	Average/max measured depth, m	Lake volume, million m^3
Lower	4289	54,000	300	235	6.2/21.8	0.328
Upper	4361	56,100	360	200	No data	No data

In 2020, both lakes had approximately the same water areas size (Table 1).

The supraglacial position of Upper Bodomdara Lake suggests further active deformation of its bed and shores as a result of melting/ retreat of the glacier. Further subsidence of its bottom and retreat and change in the outlines of its shores can be expected. The dam of the lake is unstable, which, in combination with the expansion of the lake, can lead to its outburst/water drain.

The bowl of Lower Bodomdara Lake is relatively stable. On the map of the 1988, the lake area is 40,900 m^2; at the end of the warm season in August 2008, the water area reached 49,200 m^2 (an increase by about 20%); in 2020 (after 12 years), its area increased to 52,000 m^2 (by of about 5%). Initially, the lake extended to the south and east due to active ice melting from the west side of the median moraine ridge. In the recent decade, its shoreline has been stable, and some increase in the area (taking into account the possible error) may be due to a decrease in the area of moraine islands in the lake. Currently, the lake is located in the depression made by the glacier. The depths in the center of the basin reach 22 m (Fig. 4).

The rectangular hydraulic network, along with the presence of lake-like expansion and the disappearance of surface flow into the loose material, indicates the presence of buried glacier cracks inside the dam of the lower lake. Further degradation of the dam body may lead to the isolation of individual blocks with an ice-frozen core inside and subsequent subsidence of the surface. A completely stable lake dam with a consolidated ice core and a frozen moraine cover may become unstable if current climate trends are preserved [*Harrison et al., 2018*]. An increase in the duration of the ablation period and higher summer temperatures will contribute to an increase in glacial runoff. An increase in the probability of extreme weather events (abnormal heat, sudden snowmelt, precipitation) against the background of increased runoff also poses the risk of an outburst of the lower lake.

Taking into account the unstable state of the Upper lake depression and the dam, a cascade outburst scenario – the outburst of the Upper lake as a trigger for the outburst of the lower lake – is also very likely. A possible outburst of Lower Bodomdara Lake will lead to a rapid erosion of its dam and the discharge of up to 200,000–400,000 m^3 of water. The formation of the erosional cut may follow the old flow path from the Lower lake (Fig. 4) with access to the current river cut 300–400 m downstream the current source. Loose material on the lower slope of the glacial-moraine complex is likely to be washed away to pure ice.

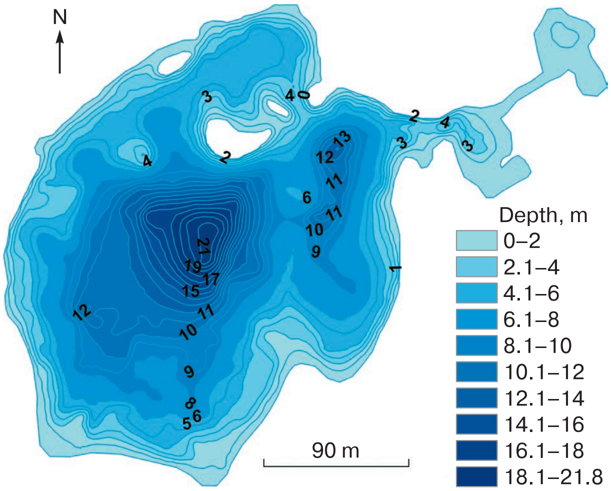

Fig. 4. Bathymetric map of Lower Bodomdara Lake (July 31, 2020).

The debris cone in the mouth of the Bodomdara River and the section of the Shakhdara River floodplain downstream the confluence with the Bodomdara River are insignificantly developed areas. In the Shakhdara River valley, numerous fragments of the Khorog–Pamir highway, including bridges over the Shakhdara River, individual buildings, and numerous agricultural lands downstream the mouth of the Bodomdara River are under threat of a possible outburst flood.

MATERIALS AND METHODS

To identify potential flood zones in the valleys of the Bodomdara and Shakhdara rivers, the following studies were carried out:

(1) field survey of the valley, bathymetric survey of the Lower lake, and survey of the debris cone of the Bodomdara River (Aga Khan Agency for Habitat (AKAH));

(2) data analysis, including interpretation of satellite images for different time periods, development of outburst scenarios, and construction of digital elevation model (DEM) for further modeling;

(3) outburst modeling actually, including (a) Lower Bodomdara Lake outburst simulation [*Vi-*

nogradov, 1976], (b) calculation of sediment increment in the area of a potential debris flow source using the transport-shift model [*Vinogradova, Vinogradov, 2017*], and (c) zoning of the Bodomdara valleys using hydrodynamic model FLO-2D [*O'Brien et al., 1993*].

In this study, we used archival satellite data *[https://services.arcgisonline.com/ArcGIS/rest/services/World_Imagery/MapServer; https://earthexplorer.usgs.gov/]* and new field materials. The bathymetric survey of Lower Bodomdara Lake was performed on July 31 by the AKAH team from a motor inflatable boat with a Lowrance Hook 5 echo sounder. The length of the water routes was about 4 km. Most of the lake area was covered by measurements. Sentinel-2 image from August 6, 2020 was used to correct the shoreline of the lake [*https://apps.sentinel-hub.com/eo-browser/*]. The survey of the Bodomdara River valley debris cone was also carried out by the AKAH team using a SenseFly eBee UAV.

The Agisoft Metashape Version 1.5.5 software package was used to process stereo images and create an orthophotoplan and a digital elevation model (DEM) of the territory. A large number of trees in the lower reaches of the Bodomdara River led to the appearance of a "levee" on the DEM. The use of machine learning methods allowed the Agisoft Metashape program to automatically classify a dense cloud of points into several classes. A classification was carried out for the "high vegetation" class. All classes were used in the construction of the DEM.

Software packages Reef Master v. 1.8.41 (viewing and visualization of echolocation data, saving of initial data of echograms) and ArcGIS 10.8.5 (processing and visualization of initial and final data) were used to process materials and build a bathymetric map.

Computational scenarios for modeling. Two scenarios of the development of an outburst flood were considered, and a set of mathematical models were used for the calculation (Fig. 5). In scenario I, the formation of an outburst flood from Lower Bodomdara Lake was assumed. The current volume of the lake (328,000 m^3) was taken into account to calculate the hydrograph of the lake outburst according to the outburst model for a lake dammed by a glacier proposed by Yu.B. Vinogradov [*Vinogradov, 1976, 1977*] was used. Then, this hydrograph was used in the transport-shift model of debris flow formation [*Vinogradov, Vinogradova, 2010*], modernized by the authors [*Iudina (Kurovskaia) et al., 2022*] to calculate sediment increment in the potential debris flow source. The obtained hydrograph was used to find the depth and velocity of the debris flow using two-dimensional hydrodynamic model FLO-2D [*O'Brien et al., 1993*].

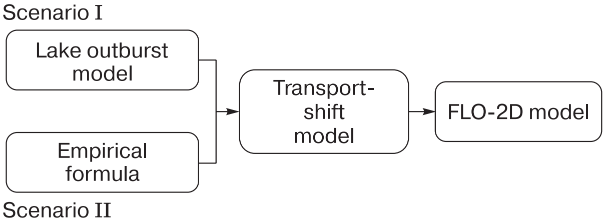

Fig. 5. A scheme of the set of mathematical models used for scenarios I and II of the outburst flood development.

Scenario II assumed a cascade outburst flood of Upper and Lower Bodomdara lakes with the maximum possible water accumulation of 700,000 m^3 in case of overflow through the dam of Lower lake. The discharge of the outburst flood for this scenario was obtained according to the formula [*Huggel et al., 2004*] and was equal to 430 m^3/s. It was then used as input hydrological data in the transport-shift model. The hydrograph calculated in the transport-shift model was used for zoning the valley in FLO-2D.

This paper does not consider a scenario, in which the flow from the Darmaidovan River blocks the Bodomdara River with the formation of a new dammed lake. Though this scenario is unlikely, it cannot be excluded. Additional research is required for its consideration. Also, when modeling, the probability of a collapse into the lake is not considered separately. The prerequisites for this collapse are created by an unstable block of rocks in the upper part of the glacier cirque in the center. Satellite images show rock falls on both sides at the end of the hanging glacier, which indicates a possible removal of an unstable block of rock in the future, possibly with a certain amount of ice of about one million cubic meters in volume. When such a block falls, an ice–stone avalanche will inevitably occur and block the upper lake; in summer, this can lead to its splash and subsequent cascade process involving the lower lake. A similar case occurred recently in Peru and was described in [*Vilca et al., 2021*]. This scenario is not considered in this paper, since the main goal was to assess potential flooding zones in the valleys of the Bodomdara and Shakhdara rivers using a set of mathematical models. The model scenarios take into account the outburst of Lower Bodomdara Lake through subglacial runoff channels and the cascade outburst of lakes with the erosion of the dam of the lower lake.

Lake outburst model. Based on the analysis of materials on lake outbursts in various regions of the world, Yu.B. Vinogradov concluded that the outburst of glacial lakes takes place not only because of the destruction of the ice dam but also because of the appearance and expansion of englacial channels [*Vinogradov, 1977*]. Indeed, modern studies confirm that outbursts of glacial lakes can be connected with the formation of englacial channels [*Huss et al., 2007; Hewitt, Jingshi, 2010; Erokhin et al., 2018; Bhambri et* *al., 2020; Che et al., 2022*]. This mechanism can be concluded from the negative asymmetry of recorded hydrographs of the outburst [*Vinogradov, 1977*]. The processes of lake outburst in such cases begin with a relatively slow increase in the outflow of water, reaching a maximum and then a sharp decline [*Huss et al., 2007; Vinogradov, Vinogradova, 2008*].

Despite the fact that Lower Bodomdara Lake is dammed not by a glacier, but by a moraine with an ice core, the authors believe that the presence of buried cracks makes it possible to use this model. Geomorphological analysis of the Darmaidovan River valley allows us to conclude that, apparently, the outburst of Lower Bodomdara Lake will first go through the buried runoff channels and then come to the surface. A similar situation was observed during the outbursts of Lake Teztor (Kyrgyzstan) in 1953 and 2012, when the stream initially formed the way through englacial runoff channels and came to the surface 400 m downstream [*Erokhin et al., 2018*].

Vinogradov's mathematical model of lake discharge is based on the equations of the development of an englacial tunnel linking into a single process the decline in the lake water level, the flow discharge, the water temperature, the appearance of the tunnel, its length, and the difference in heights [*Vinogradov, 1976*]. The works [*Vinogradov, 1976; Vinogradov, Vinogradova, 2008*] present a comparison of the modeled and observed values on the examples of outbursts of large glacial lakes in Iceland (Lake Grimsvetn, 1922, 1934, 1945; Lake Grenaloun, 1935, 1939), British Columbia (Lake Talsekva, 1958), Tajikistan (Lake Medvezhye, 1973), and the USA (Lake George, 1951). In general, the model showed sufficient agreement with the recorded hydrographs.

The model was adapted when calculating the presumptive outburst of Bashkara Lake in the Central Caucasus according to a study of the lake in 2003–2007 [*Gnezdilov et al., 2007*]. The model was also used to calculate outbursts of glacial and subglacial reservoirs of Antarctica [*Popov et al., 2019*]. In the first case, the model was written in the Fortran programming language. In the second the Delphi language was applied, but it was not published in the public domain.

If the water temperature in the lake regulated by the presence of an ice dam and floating icebergs is zero, the flow rate of the outburst flood is as follows:

$$Q=\delta\left\{\frac{\rho_0 g}{\rho r l}\left[h\left(W_0-W\right)+\frac{a}{m+1}\left(W_0^{m+1}-W^{m+1}\right)\right]\right\}^{5/4}\times$$
$$\times\sqrt{aW^m}, \tag{1}$$

where ρ_0 is the density of water, 1000 kg/m^3; ρ is the density of water–ice mixture, 850–910 kg/m^3; g is the acceleration of gravity, 9.81 m/s^2; r is the specific heat of ice melting, 334,000 J/kg; l is the length of the tunnel, m; h is the difference in heights between the entry and exit points of the tunnel, m; W_0 is the volume of water in the lake before the outburst, thousand m^3; a, m are morphometric parameters of the lake bowl determined from the equation $H = aW^m$, H is the water level in the lake; W is the volume of water in the lake; and δ is an empirical coefficient depending on the length of the tunnel. The maximum water discharge of the outburst flood will be at W, at which the following equality is fulfilled:

$$W_0\left(h+\frac{a}{m}W_0^m\right)=$$
$$=W\left[\left(\frac{2.5}{m}+1\right)h+\frac{a}{m+1}\left(\frac{2.5}{m}+3.5\right)W^m\right]. \tag{2}$$

In the case of a significant difference of lake water temperature from 0 °C, the following equations should be used [*Vinogradov, 1977*]:

$$Q=\delta\left\{\frac{\rho_0 g}{\rho r l}\left[\left(x+h\right)\left(W_0-W\right)+\frac{a}{m+1}\left(W_0^{m+1}-W^{m+1}\right)\right]\right\}^{5/4}\times$$
$$\times\sqrt{aW^m}; \tag{3}$$

$$x=\frac{C_0}{g}t\left\{1-\exp\left[-\frac{400\delta^{0.3}l\left(aW^m\right)}{Q^{0.55}\rho_0 C_0}\right]^{0.15}\right\}, \tag{4}$$

where C_0 is the specific heat capacity of water, 4190 J(kg·°C); and t is the temperature of water in the lake, °C.

According to our estimates, the length of the subglacial channel in the case of the Lower Bodomdara Lake outburst may reach 732 m. The water temperature in the lake was estimated at 2.5 °C. Morphometric parameters of the lake bowl – a and m obtained from the bathymetric survey data – were 0.061 and 0.65, respectively.

The solution of model equations (1)–(4) was implemented in the Python programming language and connected with an upgraded transport-shift model of debris flow formation.

Transport-shift model of debris flow formation. The model equations were developed by Yu.B. Vinogradov on the basis of experimental data on artificially generated debris flows in the Chemolgan River valley in 1971–1975. The debris flow discharges calculated using this model proved to be in agreements with observation data [*Vinogradova, Vinogradov, 2017*].

The PALSAR DEM (cell size 12.5 m) was used as the basis for relief modeling. The characteristics of debris flow-forming soils, such as the angle of internal friction and the ratio of the volume of water to the volume of solid substance, were used the same for both scenarios and were evaluated on the basis of regulating documents [*SP 425.1325800.2018*], engineering and geological survey materials form the Sevkavgiprovodkhoz Institute [*Nikulin, 2009*] and the works of Yu.B. Vinogradov [*Vinogradov, Vinogradova, 2010*]. In the case of an outburst of the lower lake, the potential debris flow source was supposed to be allocated to moraine in the upper reaches of the Darmaidovan River. The average slope was 13° (Fig. 6). For scenario II, a cascade outburst of the Bodomdara lakes was assumed to be the result of the overflow and/or destruction of the lake dam. In this case, data from the recharge site upstream the left tributary outflow cone were taken into account. This site also represented moraine sediments (Fig. 6). The average slope was 14.8°.

Hydrodynamic model FLO-2D. The FLO-2D model is a two-dimensional model based on the numerical solution to the Saint-Venant equations based on regular rectangular computational grids. When modeling the movement of debris flow in the FLO-2D model, it is assumed that debris flows move like a Bingham fluid (viscoplastic fluid) [*O'Brien et al., 1993*]. The basic equation of the model is the equation for calculating the friction slope [*O'Brien et al., 1993*].

To use 2D models, detailed information about the morphometry of river valleys is required, which is presented in the form of a field of points. Thus, we obtain a picture of the distribution of flow velocities, water levels, and water depths within the calculated area.

The PALSAR DEM was main source of information on the relief of the territory. The position of riverbeds was refined using satellite images. For the Shakhdara River, data from topographic maps on a scale of 1:50 000 were used to model the relief, because the PALSAR DEM for this area contained serious errors in the narrowest places of the river valley with high rocky slopes. After necessary corrections, the relief data were interpolated into the model grid with the cell size of 12.5 × 12.5 m. The UAV survey was used to construct the relief for the Bodomdara River cone with a high quality of detail. The resolution of the original digital elevation model was 1 m. The most probable parameters of debris flows were determined based on the materials of previous studies [*Petrakov et al., 2012*]. The sediment content in the debris flow was assumed to be 30–35%.

The study area downstream the lakes was divided into 5 sections (Fig. 6): (1a) the upper section of the potential debris flow source according to scenario I (the length of the section was 225 m); (1b) the upper section of the potential debris flow recharge site according to scenario II (84 m); (2) the section from the debris flow source to the alluvial cone of the Bodomdara River (the flow through this section was considered as a debris flow with the water discharge of Bodomdara River set to 5 m^3/s; the length of this section was 27 km); (3) the section for the alluvial cone of the Bodomdara River with a detailed topography obtained during the UAV survey; the flow in this section was considered as debris flow for the Bodomdara River and as water flow with the discharge of 30 m^3/s for the Shakhdara River; the length of this section was 2.4 km; (4) the section of the Shakhdara River downstream the Bodomdara cone to the confluence of the Dasht River (the water flow discharge for this section was set at 30 m^3/s; the length of this section was 18.4 km); and (5) the section of the Shakhdara River from the confluence of the Dasht River to the mouth (water discharge was equal to 30 m^3/s; section length 27.2 km).

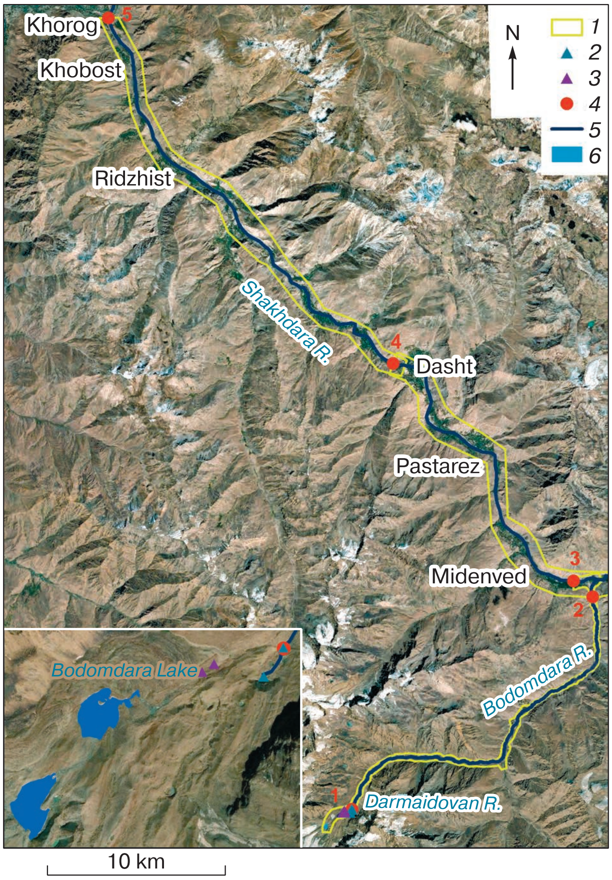

Fig. 6. Simulation scheme of possible outburst floods.

(*1*) boundaries of FLO-2D modeling, (*2*) boundaries of a potential debris flow source (scenario I), (*3*) boundaries of the recharge site (scenario II), (*4*) gauges for calculating hydrographs according to FLO-2D, (*5*) rivers, and (*6*) lakes.

RESULTS OF MODELING OUTBURST FLOODS AND DEBRIS FLOWS

According to scenario I, an outburst of Lower Bodomdara Lake with a volume of 328,000 m^3 (the

Table 2. **The results of an outburst flood simulation according to lake outburst and transport-shift models**

Scenarios	Outburst volume, m^3	Maximum discharge of the outburst flood, m^3/s	Maximum discharge of the debris flow wave, m^3/s	Lag time, h
I	328,000	167	459	0.96
II	700,000	430	840	0.40

current volume of the lake) takes place. The maximum discharge of the outburst flood calculated using the lake outburst model [*Vinogradov, 1977*] should reach 167 m^3/s and be observed 57 min after the beginning. The debris flow discharge at the debris flow source calculated according to the transport-shift model should increase to 459 m^3/s (Table 2), and the debris flow density, to 1637 kg/m^3. The average debris flow velocity at the debris flow source should be 6.1 m/s.

Scenario II assumes a cascade outburst of the Bodomdara lakes with a total volume of 700,000 m^3. The maximum discharge of the outburst flood, according to the formula [*Huggel et al., 2004*] should be 430 m^3/s. The shape of the input hydrograph was assumed to be almost symmetrical, with a maximum 24 min after the start and the total duration of 0.8 h. After passing the potential debris flow recharge site, the discharge should reach 840 m^3/s (according to the transport-shift model); the debris flow density should be 1489 kg/m^3 and the average flow velocity, 7.2 m/s.

The FLO-2D hydrodynamic model was used to obtain flood depths, flow velocities, and lag time in the valley for both scenarios of outburst flood. Hydrographs obtained in the transport-shift model of debris flow formation were used as input hydrological data. According to the simulation data, the lag time of the debris flow from the debris flow source to the alluvial cone of the Bodomdara River should be 1.67 h in scenario I and 1.37 h in scenario II (Fig. 7). The maximum water discharge at the top of the alluvial cone will be 143 m^3/s at the input discharge of 459 m^3/s and 348 m^3/s at an input discharge of 840 m^3/s.

In the Bodomdara River valley, the largest depths and flow velocities should be observed during the outburst flood passage. Under all scenarios, the flow velocities over a larger part of the channel will be 1.5–5.0 m/s and even more in some sections. The flow depths in the channel can reach 0.5–7.7 m. However, there are no infrastructure facilities and settlements in this valley, so the danger of such flood is only a potential threat.

On the alluvial cone, the flow will spread evenly over the surface. Under scenario I corresponding to lake volume in 2020, the flow depth in the Bodomdara channel may reach will reach 2 m and, in the Shakhdara channel, 4.6 m (Fig. 8*a*).

The flow velocities on the alluvial cone should not exceed 1.6 m/s. In the channels of the Bodomdara and Shakhdara rivers, they may vary from 3 to 5 m/s.

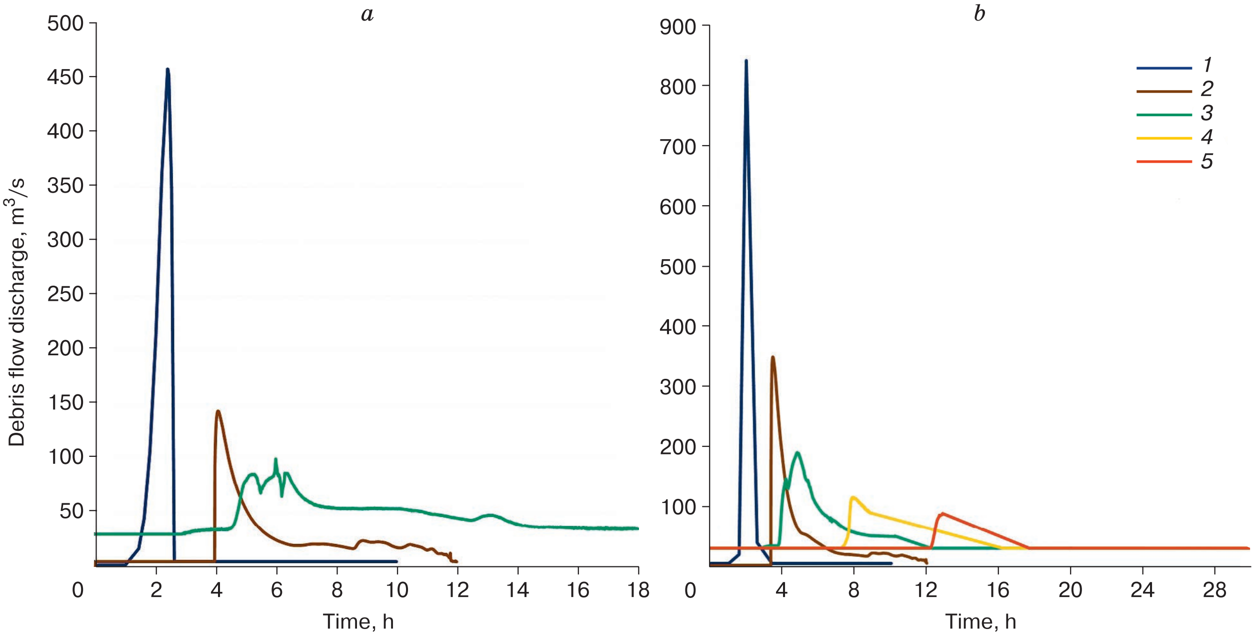

Fig. 7. Hydrographs of the outburst flood obtained from simulation according to (*a*) scenario I (outburst volume 328,000 m^3) and (*b*) scenario II (outburst volume 700,000 m^3).

(*1*) at the exit from the debris flow source, (*2*) at the top of the cone of the Bodomdara River, (*3*) the Shakhdara River downstream the Bodomdara cone, (*4*) the Shakhdara River downstream the cone of the Dasht River, (*5*) the Shakhdara River at the confluence with the Gunt River.

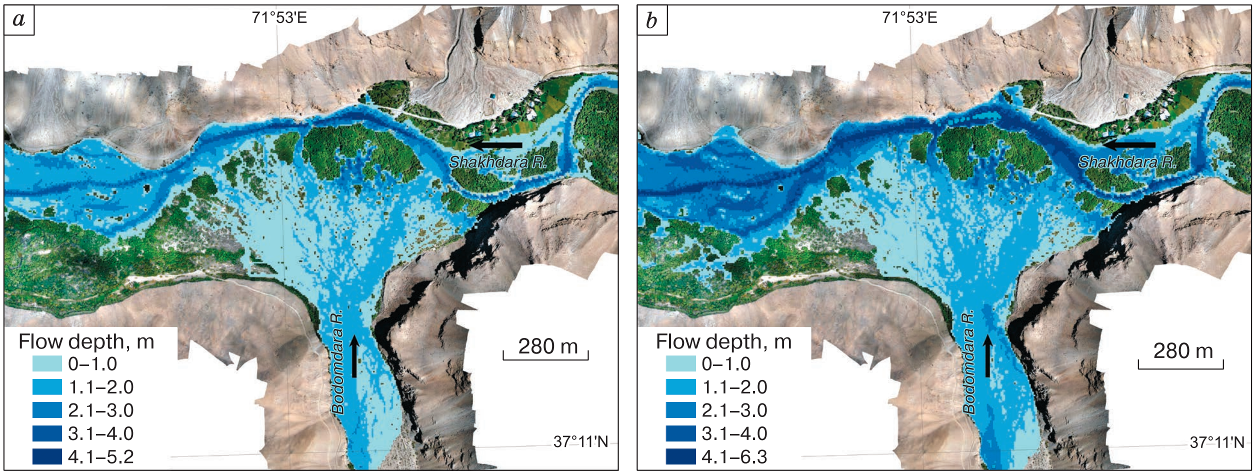

Fig. 8. Depths of flooding at the mouth of the Bodomdara River according to the results of FLO-2D modeling on detailed topographic data from UAV survey for (*a*) outburst scenario I and (*b*) outburst scenario II.

Downstream the alluvial cone, the hydrograph of the Shakhdara River should have a flattened shape due to the flow spreading; the peak of the flood will be observed in 5.2 h from the moment of the outburst, and the maximum discharge, taking into account the input discharge of the Shakhdara River (30 m^3/s) will reach 86 m^3/s, which is significantly lower than the discharge under scenario II (188 m^3/s). In this regard, the movement of the outburst flood under scenario I downstream the Shakhdara valley was not considered.

Under the hypothetical scenario II, taking into account the outburst flood of a larger volume, the depth of the flood in some areas of the alluvial cone can exceed 4 m, areas with flow velocities up to 5 m/s will be formed in the central and upper parts of the cone (Fig. 8*b*).

The maximum discharge of the Shakhdara River downstream from the Bodomdara cone will be observed in 4.8 h after the outburst and will reach 188 m^3/s. The alluvial cone of the Bodomdara River and the downstream section of the Shakhdara River floodplain are currently developed to a small extent; there are no buildings in the potential flood zone. Upstream the Bodomdara alluvial cone, on the right bank of the Shakhdara River, there are houses of the village of Otzhaga, which may be flooded in the case of damming of the Shakhdara River by the debris flow.

According to scenario II, when moving along the Shakhdara valley for 50 km to the mouth of the river, the flood will spread significantly; the maximum discharge in the middle of the section near the cone of the Dasht River and the village of the same name will be 114 m^3/s; the flood wave will reach this gauge is 7.92 h. In the mouth of the Shakhdara River, the wave of the outburst flood will reach a maximum in 13 h after the lake outburst. The maximum discharge at the mouth of the Shakhdara River will reach 89 m^3/s (taking into account the base discharge of 30 m^3/s), which will exceed the maximum discharge of 48.6 m^3/s observed at the gauge station in the village of Khabost (at the mouth of the river) [*Surface*..., *1971*]. It is worth noting that most settlements along the Shakhdara River in its lower reaches are located at fairly high levels relative to the water level; however, flooding of houses and other buildings in close proximity to the river with the flow depth varying from 0.3 to 1.0 m can be observed. To obtain more accurate results, it is necessary to use detailed topographic data for each locality. It is important that any economic activity (pasturing, haymaking, etc.) in the floodplain areas is potentially endangered by the in outburst flood in the considered areas.

CONCLUSIONS

Possible causes and consequences of an outburst flood in the Bodomdara River valley have been estimated using data from detailed field studies. When comparing the location of the edges of the active glacier tongues on satellite images of 2008 and 2020, the retreat of the glacier by 50–120 m in 12 years (i.e., up to 10 m/yr) has been determined. The edge of the glacial-moraine complex is stable, but the ice wall above the river source has also noticeably retreated (by 35–40 m in 12 years; 3 m/yr). The degradation of the glacier leads to the changes in dynamics of glacial lakes and their dams. Thus, Upper Bodomdara Lake has appeared in recent decades. The supraglacial position of this lake suggests a possibility of its outburst as a result of the retreat of the glacier and the damage of the ice dam. In turn, this will trigger an outburst of Lower Bodomdara Lale with the development of cascade outburst flood. Though the bowl-shaped depression of the lower lake is relatively stable, its outburst is possible without a cascade flood at abnormally high temperatures and intense snowmelt combined with extreme rainfall.

For the first time, an integration of three mathematical models has been used to model outburst floods : the model of lake outburst through englacial channel by Yu.B. Vinogradov, the transport-shift model by Yu.B. Vinogradov, and the FLO-2D hydrodynamic model.

Two scenarios of an outburst flood were considered: (I) outburst of Lower Bodomdara Lake with a volume of 328,000 m^3 and (II) cascade outburst of both lakes with a total volume of 700,000 m^3. For scenario I, the maximum discharge of the outburst flood obtained using bathymetric lake survey data and lake outburst model by Yu.B. Vinogradov may reach 167 m^3/s. Further estimate of sediment material increment at the potential debris flow source has been carried out using a transport-shift model of debris flow formation; the predicted discharge of the debris flow may reach 460 m^3/s. A two-dimensional hydrodynamic model FLO-2D with a debris flow block has been adapted to the section of the outburst flood movement along the Darmaidovan, Bodomdara, and Shakhdara rivers with a total length of 75 km. This adapted model has been used to estimate the depth of the flood, flow velocities, potential danger of the flood, and the lag time of the maximum flood wave after the outburst flood. According to the results of hydrodynamic modeling, at the top of the alluvial cone of the Bodomdara River, the maximum flow discharge will be 143 m^3/s; it will be reached in 4.07 h after the outburst of the lake. The maximum discharge of the Shakhdara River downstream the cone will be 86 m^3/s.

The maximum discharge of the outburst flood according to scenario II as calculated using the formula [*Huggel et al., 2004*] will be 430 m^3/s. After the additional increment at the debris flow recharge site, it will reach 840 m^3/s. At the top of the alluvial cone of the Bodomdara River, the maximum flow discharge will be 348 m^3/s, and it will be reached in 3.47 h after the start of the outburst. The flow velocities will reach 3 m/s, and the flow depth will reach 4 m. The maximum flow discharge in the Shakhdara River downstream the Bodomdara alluvial cone will be 188 m^3/s; at the river mouth (50 km downstream), it will decrease to 89 m^3/s. These discharges in the lower reaches of the Shakhdara River are three times higher than the maximum recorded water discharges. Despite the fact that most of the settlements in the Shakhdara River valley are located at fairly high elevations beyond the flood prone zone, the bridges of the Khorog–Pamir highway across the Shakhdara river are at risk. Meadows and pastures and outbuildings within them, as well as individual houses located on the banks of the river are in the flood prone zone. The greatest damage can be expected in the area of the villages of Bidizi Bolo, Anbaz/Vezdara, Tsorzh, and Midenved. A damage to buildings and lands of the village of Otzhaga on the right bank of the Shakhdara River immediately upstream the mouth of the Bodomdara River is also possible because of the damming effect of the debris flow as a result of river bank erosion and flooding.

Taking into account the unfavorable dynamics of the glacial-moraine complex, the further growth of the upper lake and the possible breach of the lower lake dam, regular remote monitoring of the situation in the upper reaches of the Darmaidovan River is necessary. Planning of economic activity in the valleys of the Bodomdara and Shakhdara rivers below the mouth of the Bodomdara River should be carried out taking into account the possibility of an outburst flood wave passing here.

Acknowledgments. *This study was supported by the Russian Foundation for Basic Research (project no. 20-35-90006); it was carried out within framework of the state assignments of Lomonosov Moscow State University, sections I.7 (CITIS 121051300175-4), I.10 (CITIS 121051400038-1) and of Water Problems Institute of the Russian Academy of Sciences 0147-2019-0001 (CITIS AAAA-A18-118022090056-0).*

The authors express their gratitude to the staff of the Aga Khan Agency for Habitat in the Republic of Tajikistan R.A. Bobov, T.Z. Sabzaliev, H.S. Abdulasanov, A. Akimbekov, M. Gulomnosirov, M. Marodmamadov, F. Fidoliev for assistance in organizing field work.

References

Bhambri R., Watson C.S., Hewitt K. et al., 2020. The hazardous 2017–2019 surge and river damming by Shispare Glacier, Karakoram. *Sci. Rep.* **10** (4685). DOI: 10.1038/s41598-020-61277-8.

Cesca M., d'Agostino V., 2008. Comparison between FLO-2D and RAMMS in debris-flow modeling: a case study in the Dolomites. *WIT Transact. Engin. Sci.* **60**, 197–206. DOI: 2495/DEB080201.

Che Y., Wang S., Wei Y. et al., 2022. Rapid changes to glaciers increased the outburst flood risk in Guangxieco Proglacial Lake in the Kangri Karpo Mountains, Southeast Qinghai-Tibetan Plateau. *Nat. Hazards* **110**, 2163–2184. DOI: 10.1007/s11069-021-05029-5.

Dokukin M.D., Bekkiev M.Yu., Kalov R.Kh. et al., 2020. Rock glaciers as origination sites of the catastrophic debris flows. *Georisk* **14** (2), 52–65 (in Russian).

Erokhin S.A., Zaginaev V.V., Meleshko A.A. et al., 2018. Debris flows triggered from non-stationary glacier lake outbursts: the case of the Teztor Lake complex (Northern Tian Shan, Kyrgyzstan). *Landslides* **15**, 83–98. DOI: 10.1007/s10346-017-0862-3.

Glazyrin G., Braun L.N., Shchettinnikov A.S., 2018. Sensitivity of mountain glaciation erization to climate changes in Central Asia. *Zeitschrift fuer Gletxcherkunde. Glazialgeol.* **39**, 71–76.

Gnezdilov Yu.A., Ivaschenko E.N., Krasnykh N.Yu., 2007. Assessment of the hypothetical outburst of Lake Bashkara. In: *Collection of Scientific Works of JSC Sevkavgiprovodkhoz*, Pyatigorsk, **17**, pp. 122–145 (in Russian).

Iudina (Kurovskaia) V.A., Chernomorets S.S., Vinogradova T.A., Krylenko I.N., 2022. Modeling of debris flow triggered by snow melting: case study of the Barsemdara River, Tajikistan. *Earth's Cryosphere* **26** (3), 43–53.

Harrison S., Kargel J.S., Huggel C. et al., 2018. Climate change and the global pattern of moraine-dammed glacial lake outburst floods. *The Cryosphere* **12** (4) 1195–1209. DOI: 10.5194/tc-12-1195-2018.

Hewitt K., Jingshi L., 2010. Ice-dammed lakes and outburst floods, Karakoram Himalaya: historical perspectives on emerging threats. *Physical Geogr.* **31** (6), 528–551.

Huggel C., Haeberli W., Kääb A. et al., 2004. An assessment procedure for glacial hazards in the Swiss Alps. *Can. Geotech. J.* **41** (6), 1068–1083.

Huss M., Bauder A., Werder M. et al., 2007. Glacier-dammed lake outburst events of Gornersee, Switzerland. *J. Glaciol.* **53** (181), 189–200. DOI: 10.3189/172756507782202784.

Hutter K., Svendsen B., Rickenmann D., 1994. Debris flow modeling: A review. *Continuum Mech. Thermodyn.* **8**, 1–35.

Jan C.D., Shen H.W., 1997. Review dynamic modeling of debris flows. In: Armanini A., Michiue M. (Eds.), *Recent Developments on Debris Flows. Lecture Notes in Earth Sciences*, vol. 64. Springer, Berlin, Heidelberg. DOI: 10.1007/BFb0117764.

Jansky B., Engel Z., Sobr M. et al., 2009. The evolution of Petrov Lake and moraine dam rupture risk (Tien-Shan, Kyrgyzstan). *Natural Hazards J.* (1), 83–96.

J-42-108 (Roshtkala). Topographic Map, Scale 1:100 000. Joint Staff, Moscow, 1988.

Kääb A., Huggel C., Fische L. et al., 2005. Remote sensing of glacier- and permafrost-related hazards in high mountains: an overview. *Nat. Hazards Earth Syst. Sci.* **5**, 27–554. DOI: 10.5194/nhess-5-527-2005.

Kidyaeva V.M., Chernomorets S.S., Savernyuk E.A. et al., 2020. Outburst-hazardous lakes in the Gunt River basin (Gorno-Badakhshan Autonomous Region, Tajikistan): hazard assessment and outburst modeling. In: *Avalanches, Debris flows and Risk Assessment*. Moscow, Pero, pp. 18–43 (in Russian).

Khromova T.E., Osipov G.B., Tsvetkov D.G. et al., 2006. Changes in glacier extent in the eastern Pamir, Central Asia, determined from historical data and ASTER imagery. *Remote Sens. Environ.* **102** (1–2), 24–32.

Khromova T., Nosenko G., Kutuzov S. et al., 2014. Glacier area changes in Northern Eurasia. *Environ. Res. Lett.* **9** (1), 015003.

Komatsu T., Watanabe T., 2014. Glacier-related hazards and their assessment in the Tajik Pamir: A short review. *Geograph. Studies* **88** (2), 117–131.

Kotlyakov V.M., Dyakova A.M., Koryakin V.S. et al., 2011. *Glaciers of the Former Soviet Union. Glaciers of Asia*, U.S. Geol. Survey Prof. Paper 1386–F, 349 pp.

Luknitsky P.N., 1955. *Travels in the Pamir.* Moscow, Molodaya Gvardiya, 502 pp. (in Russian).

Mergili M., Müller J.P., Schneider J.F., 2013. Spatio-temporal development of high-mountain lakes in the headwaters of the Amu Darya River (Central Asia). *Glob. Planet. Change* **107**, 13–24.

Mergili M., Schneider J.F., 2011. Regional-scale analysis of lake outburst hazards in the southwestern Pamir, Tajikistan, based on remote sensing and GIS. *Nat. Hazards Earth System Sci.* **11**, 1447–1462.

Mergili M., Schneider D., Worni R. et al., 2011. Glacial lake outburst floods in the Pamir of Tajikistan: Challenges in prediction and modeling. Proc. 5th Intern. Conf. *Debris-Flow Hazards Mitigation: Mechanics, Prediction and Assessment* (Padua, June 14–17, 2011). Padua, Italy, pp. 973–982.

Mikhailov V.O., 2011. Classification of numerical mathematical models of debris flow and slope processes. *Inzhenern. Geol.* **3**, 26–33 (in Russian).

Mikhailov V.O., Chernomorets S.S., 2011. *Mathematical Modeling of Debris flows, Collapses and Landslides*. Moscow, Lambert, 131 pp. (in Russian).

Nikulin A.S., 2009. Experience in determining the angles of internal friction of debris flow clay. In: *Collection of Scientific Works of JSC Sevkavgiprovodkhoz* **18**, 30–33 (in Russian).

O'Brien J., Julien P., Fullerton W., 1993. Two-dimensional water flood, debris flow simulation. *J. Hydraul. Engin.* **119** (2), 244–259.

Petrakov D.A., Tutubalina O.V., Aleinikov A.A. et al., 2012. Monitoring of Bashkara Glacier lakes (Central Caucasus, Russia) and modelling of their potential outburst. *Nat. Hazards* **61** (3), 1293–1316. DOI: 10.1007/s11069-011-9983-5.

Popov S.V., Pryakhina G.V., Boronina A.S., 2019. Estimation of water discharge during development of glacial and subglacial outburst floods. *Earth's Cryosphere* **23** (3), 20–26.

Quincey D.J., Richardson S.D., Luckman A. et al., 2007. Early recognition of glacial lake hazards in the Himalaya using remote sensing datasets. *Glob. Planet. Change* **61** (1–2), 0–152.

Surface Water Resources of the USSR: Hydrological Study. Vol. XIV. Basins of the Rivers of Central Asia. Iss. 3. Amu Darya Basin. Leningrad, Gidrometeoizdat, 1967, 322 pp. (in Russian).

Surface Water Resources of the USSR. vol. XVI. Central Asia. Iss. 3. Amu Darya Basin. Leningrad, Gidrometeoizdat, 1971, 472 pp. (in Russian).

SP 425.1325800.2018, 2019. *Engineering Protection of Territories from Erosion Processes. Design Rules*. Moscow, Standartinform, 36 pp. (in Russian).

URL: https://earthexplorer.usgs.gov/ (date accessed: Sept. 8, 2021, date of issue: Sept. 13, 1975).

URL: https://earthexplorer.usgs.gov/ (date accessed: Sept. 8, 2021; date of issue: Aug. 20, 2010).

URL: https://apps.sentinel-hub.com/eo-browser/ (date accessed: Sept. 15, 2021; date of issue: 2015–2021).

URL: https://services.arcgisonline.com/ArcGIS/rest/services/World_Imagery/MapServer (date accessed: Sept. 1, 2021; date of issue: Sept. 10, 2013).

Vilca O., Mergili M., Emmer A. et al., 2021. The 2020 glacial lake outburst flood process chain at Lake Salkantaycocha (Cordillera Vilcabamba, Peru). *Landslides* **28**, 2211–2223. DOI: 10.1007/s10346-021-01670-0.

Vinogradov Yu.B., 1976. Method for calculating flood hydrograph in case of outburst of a glacier-dammed lake. In: *Debris Flows*. Moscow, Gidrometeoizdat, Iss. 1, pp. 138–153 (in Russian).

Vinogradov Yu.B., 1977. *Glacial Outburst Floods and Debris flows*. Leningrad, Gidrometeoizdat, 154 pp. (in Russian).

Vinogradov Yu.B., 1980. *Etudes about Debris Flows*. Leningrad, Gidrometeoizdat, 160 pp. (in Russian).

Vinogradov Yu.B., Vinogradova T.A., 2008. *Modern Problems of Hydrology*. Moscow, Academy, 320 pp. (in Russian).

Vinogradov Yu.B., Vinogradova T.A., 2010. *Mathematical Modeling in Hydrology.* Moscow, Academy, 304 pp. (in Russian).

Vinogradova T.A., Vinogradov A.Yu., 2017. The experimental debris flows in the Chemolgan River basin. *Nat. Hazards* **88** (Suppl. 1), 189–198.

Voellmy A., 1995. Über die Zerstörungskraft von Lawinen, *Schweiz. Bauzeitung* **73** (12), 159–162.

Wang X., Ding Y., Liu S. et al., 2013. Changes of glacial lakes and implications in Tian Shan, central Asia, based on remote sensing data from 1990 to 2010. *Environ. Res. Lett.* **8** (4), p. 044052.

Wu Y.H., Liu K.F., Chen Y.C., 2013. Comparison between FLO-2D and Debris-2D on the application of assessment of granular debris flow hazards with case study. *J. Mount. Sci.* **10** (2), 293–304.

Received December 4, 2021
Revised July 10, 2022
Accepted September 20, 2022

Translated by S.B. Sokolov

EARTH'S CRYOSPHERE
SCIENTIFIC JOURNAL

Earth's Cryosphere, 2022, vol. XXVI, No. 5, pp. 25–34

CRYOGENIC PHENOMENA IN SEAS AND OCEANS

FREQUENCY OF OCCURRENCE OF FAST ICE CALCULATED FROM POLYGONS OF DIGITIZED ICE CHARTS USING THE EXAMPLE OF THE KARA SEA

R.I. May[1,2,*], K.R. Ganieva[1], A.G. Topaj[3], A.V. Yulin[4]

[1] *St. Petersburg State University, Department of Oceanology, Universitetskaya Emb. 7/9, St. Petersburg, 199034 Russia*
[2] *Krylov State Research Center, Moskovskoe shosse 44, St. Petersburg, 196158 Russia*
[3] *LLC "Bureau Hyperborea", Kavalergardskaya St. 6A, St. Petersburg, 191015 Russia*
[4] *Arctic and Antarctic Research Institute, Beringa St. 38, St. Petersburg, 199397 Russia*

**Corresponding author; e-mail: rimay@mail.ru*

Many elements of the natural environment are areal objects that change their position and shape at all scales of variability. For sea ice, such elements can be fast ice, drifting ice, polynyas, ice massifs, and boundaries of multi-year ice. In other earth sciences, these are the boundaries of glaciers, permafrost, snow cover, forest zone, and various isolines of meteorological and oceanological fields (isotherms, isobars, etc.). To analyze such objects, one can usually use approximations in the form of a grid area (rasterization) or a system of sections. In this article, we suggest a direct analysis of these objects based on operations with vector polygons. An efficient algorithm for calculating the probability (frequency of occurrence) of an unlimited number of polygons has been developed and tested. A criterion for selecting one of the real edges of a polygon as an analogue of the isoline of the probability of intersections of polygons is proposed. The developed method has been tested using data on the fast ice of the Kara Sea taken from the digital ice charts developed by the Arctic and Antarctic Research Institute for 1998–2020. As a result, the charts of fast ice probability for the cold season of each year and for a given time of the year for the entire considered period have been obtained. Based on these data, the operational characteristics of fast ice have been estimated, and a tendency for a decrease in the area of fast ice during the considered period has been revealed. For the beginning of May (the period of the maximum development of fast ice), analogues from factual observations characterizing extreme, median, and quartile probability isolines of fast ice occurrence have been found.

Keywords: *fast ice, sea ice, Kara Sea, analysis of polygons.*

Recommended citation: May R.I., Ganieva K.R., Topaj A.G., Yulin A.V., 2022. Frequency of occurrence of fast ice calculated from polygons of digitized ice charts using the example of the Kara Sea. *Earth's Cryosphere* **26** (5), 25–34.

INTRODUCTION

The fast ice of the Arctic seas (fixed ice along the coastline) is a unique ice formation that is constantly formed during the cold season in the coastal zone of the coast of the mainland and the islands. The presence of fast ice is a characteristic feature of the ice regime of the Arctic seas in the winter season [*Vize, 1944, 1948; Zubov, 1944*]. According to the definition [*Volkov, 1981; WMO No. 259, 2014; Atlas..., 2018*], fast ice is considered to be sea ice that forms and remains motionless along the coast, where it is attached to the shore, ice wall, ice barrier, between shoals, or between grounded ice hummocks. Fast ice can form naturally from salt water or when floating ice of any age category freezes to the shore or to the already existing fast ice.

As a rule, fast ice has the maximum thickness among ice of the same age due to its long and calm growth [*Gudkovich et al., 1972; Gorbunov et al., 1983*]. Fast ice radically changes the characteristics of the hydrological regime of the occupied water area. Fast ice (as opposed to drifting ice) is one of the reasons for the seasonal variability of tide characteristics. The circulation of water under fast ice differs from the circulation of water under drifting ice. The fast ice boundary can be an area of intense hummock formation during ice pressure drift. Vice versa, during offshore winds, polynyas with special hydrological and thermal balance conditions are formed near the fast ice boundaries [*Gordienko, 1971; Karelin, Karklin, 2012*]. Fast ice is important from a practical perspective: on the one hand, it can become an obstacle to navigation, on the other hand, fixed ice can serve as a temporary berth for unloading cargo at an unequipped shore. Polynyas formed near the fast ice are, most often, the easiest areas for Arctic navigation. The channel laid in the fast ice retains its position and is used during the entire navigation period.

The evaluation of fast ice regime characteristics along the given sections was carried out in [*Dmitrenko et al., 1999; Karelin, Karklin, 2012; Arkhipov et al.,*

Copyrights © 2022 R.I. May, K.R. Ganieva, A.G. Topaj, A.V. Yulin, All rights reserved.

2017]. The Arctic and Antarctic Research Institute (AARI) uses standard alignments that run perpendicular to the coastline. The distance between the sections varies from 50 to 150 km; the Kara Sea has only 28 standard sections [*Karelin, Karklin, 2012*]. Obviously, the accuracy of the fast ice description depends on the number of selected sections. At large distances between the sections, the obtained statistical characteristics are polygonal objects with a rough spatial resolution. The paper [*Pavlova et al., 2019*] gives a quantitative estimate of the error in determining the maximum fast ice in the Kara Sea based on data from standard AARI sites: the maximum error in the fast ice width is ~30–40 km.

Increasing the gate frequency can offset this error to some extent. For the coast of Alaska, sections were drawn along the points located on the coast and a line 150 km away from the coast [*Mahoney et al., 2007, 2014*]. The alignment points on the sea line were spaced apart at 1 km from one another and connected to the nearest points on the coast. Based on the composition of various radar satellite images, the coordinates of the fast ice edge were determined. Thus, a frequent alignment was used for automatic delineation of the boundaries of fast ice and the determination of some statistical characteristics of its distribution along the sections [*Mahoney et al., 2007, 2014*].

Even with a high frequency of alignments, this method contains uncertainties: with a winding coastline (bays, gulfs, capes, peninsulas, islands), the alignments perpendicular to the coast can intersect, lie entirely within the fast ice fields, cross the edges of the fast ice of opposite coasts, etc.

Another method for studying the regime characteristics of fast ice is based on the use of grid areas, the nodes of which contain a sign of the presence or absence of fast ice. This method was used in [*Divine et al., 2004; Mahoney et al., 2007, 2014; Galley et al., 2012; Yu et al., 2014; Selyuzhenok et al., 2015; Li et al., 2020*]. The sum of signs of the presence or absence of fast ice in each cell of the grid area, related to the total number of analyzed fields of fast ice, allows us to estimate the probability of the presence of fast ice in the cell. In this case, in grid methods, the results of analysis depend on the spatial step. The problem of fast ice approximation by a grid area was raised in [*Yu et al., 2014; Pavlova et al., 2019*].

Obviously, the smaller the spatial grid step, the more accurate the approximation. However, acceptable spatial grid steps require significant computational resources. In studies of the regime characteristics of fast ice, grids with spatial steps from 100 m [*Mahoney et al., 2007, 2014*] to 12.5 km [*Divine et al., 2004; Yu et al., 2014*] are used. Thus, the analysis of fast ice variability can be based on the gate and grid methods. Modern information on ice is represented by vectorized polygons that describe areal objects (fast ice, ice zones, polynyas, leads) in the form of a sequence of coordinates of boundary points. At the same time, statistical analysis of data in the form of lines (curves, functions) is fundamentally possible [*Ramsay, Silverman, 2005*].

MATERIALS AND METHODS

Electronic ice charts

Special SIGRID formats have been developed for the storage and dissemination of ice information, allowing the storage of multidimensional ice cover data. The first two versions of the format were based on the matrix principle of information storage. In 1995, the AARI developed the SIGRID-3 format, which allows storing vector information about the ice cover in the form of polygons that outline certain zones with the same ice parameters. This vector format is most suitable for describing ice zones in general and fast ice, in particular. To store polygons of ice zones in the SIGRID-3 format, the geographic information system file structure developed by ESRI is used. The SIGRID-3 format has been adopted by the World Meteorological Organization as the main format for the storage and dissemination of ice information. This format is used by major sea ice research centers.

This article describes the results of the analysis of ice information provided by the AARI through the World Data Center–Sea Ice (WDC-SI) [*http://wdc.aari.ru/datasets*]. The information covers the interval from 1997 to the present time with weekly time step. The AARI ice charts presented on the WDC-SI website were created based on the analysis of satellite information in various ranges of the electromagnetic spectrum by ice experts. An ice expert determines ice zones based on his experience, knowledge of the regime characteristics of the ice cover in a given area, and on constant monitoring of changes in the ice situation. Each ice expert specializes in a separate water area, so AARI provides ice charts separately for 12 Arctic and freezing seas of Russia [*Afanasyeva et al., 2019*]. This paper presents calculations of the regime characteristics of the appearance of fast ice using the example of the Kara Sea as a water area where year-round navigation of ships is carried out.

In each electronic ice chart, coordinates of the fast ice boundaries are given with due account for the ice zone. Separate fast ice areas observed in a given time are combined into one landfast ice polygon. Since AARI ice charts are created manually by experts, in some cases, objective and subjective errors may occur. At the first stage, all landfast ice polygons are visually checked for such errors. Ice charts that do not display information about fast ice in some separate part of the water area are considered unsuitable for analysis (December 22, 1999; June 5, 2003; April 29, 2014; December 25, 2018). In some cases, either fast ice is completely absent (October 30, 2003; February 27, 2018), or the displayed fast ice polygon differs significantly from the information of ice charts adjacent in time (August 12, 2003). In addition, on some ice charts, the fast ice polygon is artificially cut off in the Gulf of Ob and the Yenisei Bay. The missing sections of the landfast ice polygons in the Gulf of Ob and the Yenisei Bay are restored to avoid errors in the calculation of areas during the analysis due to artificial distortions of the ice zones.

Operations with vector polygons

Operations with polygonal objects can be described with mathematical symbols from the algebra of sets: union of polygons ($A \bigcup B$), subtraction of polygons (A\B) and intersection of polygons ($A \cap B$) (Fig. 1). Based on these three steps, it is possible to create algorithms for calculating the repeatability (probability) of polygon intersections. Consider a sample of N polygons P_n, $n = 1, ..., N$, for which we will build probabilistic intersection polygons – an analogue of constructing a histogram or an empirical probability distribution for scalar quantities. The composition of this sample is determined by the semantics of the problem under consideration. For example, it can include all polygons for a limited period of a calendar year (landfast ice distribution in April) or the entire ice season. The union of all landfast ice polygons P_n will give one vast polygon, maximum in area and coverage, where landfast ice was noted at least once. This polygon $Q_{1/N}$ will correspond to the area, where the probability of finding landfast ice is greater than or equal to $1/N$:

$$Q_{1/N} \geq \bigcup_{n=1}^{N} P_n.$$

Meanwhile, the intersection of all sample polygons forms a set of points where landfast ice is observed for all considered ice charts; in other words, this is the area where the probability of finding landfast ice is N/N, that is, one:

$$Q_1 = Q_{N/N} = \bigcap_{n=1}^{N} P_n.$$

Along with these extreme cases, it is of interest to determine the areas occupied by landfast ice with any intermediate probability n/N, where $n = 1, ..., N$. The most obvious algorithm for calculating such polygons of probabilities $Q_{n/N}$ is as follows. It is necessary to consider sequentially all subsets of the complete sample, consisting of exactly n polygons without repetitions and without taking into account permutations. For each of these subsamples Ω_k, we find the intersection of its component polygons and all these intersections merge:

$$Q_{n/N} = \bigcup_{k=1}^{C_n^N} \left(\bigcap_{\Omega_k} P_i,\ i \in \Omega_k \right), \tag{1}$$

where $C_n^N = \dfrac{N!}{n!(N-n)!}$ is the number of combinations.

Unfortunately, the direct sequence of operations according to formula (1) often cannot be technically implemented due to exponentially increasing computational complexity. So, for the size of the initial sample of 22 polygons and the calculation of the "median" polygon of intersections, i.e., for $n = 11$, the number of analyzed subsamples is equal to the number of combinations from 22 to 11, which is 705,432 variants. Of course, performing several operations with vector polygons is difficult.

Perhaps this feature of the most obvious algorithm (1) explains the fact that up to now, no analysis of polygons has been carried out directly, without an intermediate raster (grid) or gate approximation. To solve this problem, the authors proposed, implemented, and tested an algorithm for recursively recalculating the entire set of probabilistic intersection polygons while successively adding new initial polygons to the sample. We can say that this algorithm is analogous to adaptive statistical estimation algorithms. Indeed, let at the $(n-1)$-th step of our algorithm, i.e., for $n-1$ already processed polygons, we know the probabilistic polygons of the intersection $R_{k/N}$, where each such polygon is a set of points falling strictly into k initial polygons (in contrast to the polygons of the intersection Q, for which the membership condition is formulated as "no less than in k initial polygons"). Then, when a new initial polygon P_n is introduced into consideration, all these polygons are recalculated at a new step of the algorithm according to a simple rule:

$$R_{k/N}^{n} = \left(R_{k-1/N}^{n-1} \cap P_n \right) \cup \left(R_{k/N}^{n-1} \setminus P_n \right);$$

$$R_{k/N}^{0} = \varnothing,\ k = 1, ..., N. \tag{2}$$

Formula (2) demonstrates how a set of points forming the k-th set of intersections of the initial

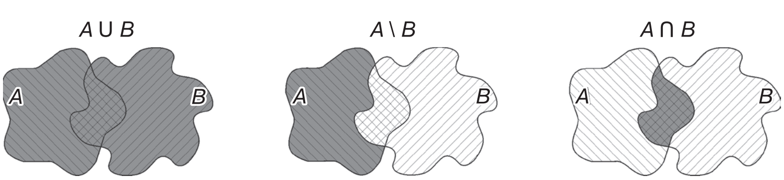

Fig. 1. Operations with vector polygons.

polygons is created when a new initial polygon appears. These points coincide with the points for the corresponding (k–1)-set at the previous step, which fall into the new polygon, and the points for the corresponding k-set at the previous step, which do not fall into the new polygon.

In the meantime, the polygons of intersections of the cumulative probability $Q_{n/N}$ that are of interest to us can always be calculated using the formula:

$$Q_{n/N} = \bigcup_{k=1}^{n} R_{k/N}. \quad (3)$$

The algorithm described by formulas (2) and (3) allows quick recursive calculation of the polygon intersection probability for an unlimited number of polygons P_n, since the computational complexity of the algorithm grows with an increase in the number of polygons only in a quadratic dependence.

The spatial slice of the obtained intersection frequency field, drawn orthogonally to the coastline and the polygons of probability Q_p, will outwardly resemble the empirical function of the spatial distribution of the probability value, where the distance is plotted along the abscissa axis, and the probability values varying from 0 in the seaward part to 1 at the coast are plotted along the ordinate. Thus, it is possible to find correspondences between the considered method of vector polygon analysis and the gate method. At the same time, it is possible that along such a cut there will be local decreases in probabilities associated with the influence of local conditions (the influence of landfast ice located near individual islands, prominent elements of the coastline, ice hummocks, etc.). Such effects inherent in the gate method are associated with the choice of the position and direction of the slices.

In the accepted notation, the analogue of the interquartile distance will be the Q_{IQR} polygon, which can be calculated as the difference between the polygons $Q_{p\,=\,0.25}$ and $Q_{p\,=\,0.75}$:

$$Q_{IQR} = Q_{p\,=\,0.75} \setminus Q_{p\,=\,0.25}. \quad (4)$$

It should be noted that the obtained “probabilistic” polygons of finding landfast ice Q_p will never exactly coincide with any of the actually observed landfast ice edges P_n. The probability isolines obtained during vector operations will be a broken line composed of fragments of landfast ice edges for different years or dates. Therefore, it is of interest to be able to replace the obtained “virtual” isoline with its close analogue from the real world. To select one of the observed landfast ice edges P_n closest to Q_p, one can use the concept of “functional data depth” [*Lopez-Pintado, Romo, 2009*]. In functional data analysis, the “depth” function determines how “deep” a point or curve is in the selected data cloud in Euclidean space, that is, how close it is to an implicitly defined center that has a maximum “depth”. The authors propose using the condition $S(D_n)$ = min as a criterion for the “depth” of the landfast ice line, i.e., its correspondence to the obtained “virtual” standard, where the chosen proximity norm $S(D_n)$ is the area of polygon D_n, which is determined from the equation

$$D_n = \left(Q_p \setminus P_n\right) \cup \left(P_n \setminus Q_p\right).$$

From the entire set of observed landfast ice polygons P_n, the one for which the polygon area D_n is minimal is selected. A similar criterion is used in the least squares method: the minimum of the sum of squares of the difference between the data and the approximating function has the geometric meaning of the minimum of the area between the measured values and the function.

The algorithm for calculating the probability of polygon intersections described above was implemented in the MatLab language as a set of programs and functions, the files of which can be found in the public domain at [*https://www.mathworks.com/matlabcentral/fileexchange/99879-probability-of-polygon-sintersection*].

RESULTS AND DISCUSSION

The AARI ice charts are provided with weekly discreteness, therefore, for the analysis of landfast ice polygons, the authors used ten-day periods; each month was divided into three such periods. From the entire data array, ice charts closest in time to the central day of the ten-day period were selected. Thus, as such central dates, the authors chose days 5, 15, and 25 of each month. Taking into account that ice charts are created from a series of satellite images covering several days, it can be assumed that the maximum deviations of three days for the dates of a weekly and ten-day discreteness will not greatly affect the results of the analysis.

Using the method described above for estimating the probability of crossing polygons, it is possible to determine the operational characteristics of the occurrence of landfast ice. Depending on the period of time, for which the data array is analyzed, it is possible to estimate the seasonal or interannual variability of landfast ice frequency.

Analysis of data for one cold season will show the repeatability of the landfast ice position for a given year. A comparison of annual charts of landfast ice position frequency for several years will reveal interannual variability. As an example, polygons of landfast ice position probability during one cycle of formation and destruction (October–July) for 2000, 2005, 2010, 2015, and 2020 are given (Fig. 2). A series of charts shows a trend towards a decrease in the area occupied by landfast ice. For 1999–2005, the landfast ice of Sergey Kirov Islands (77°15′ N, 91° E) and of Voronin Island (77°15′ N, 91° E) for most of the considered period (October–July) are located inside a vast landfast ice field connected to the mainland. As seen in Fig. 2, the probability of finding landfast ice between these islands and the Taimyr Peninsula in 2000 and 2005 is 0.6–0.8, i.e., landfast ice occurs for 15–21 ten-day periods out of 27. Similar probability values are observed for other years in the interval from 1998 to 2005, except for 2002, when landfast ice connected to the mainland was observed only during 2–3 ten-day periods out of 27 decades (probability about 0.1). From 2008 to 2020, a different picture is noted: landfast ice of Sergey Kirov and Voronin islands was connected with the mainland landfast ice in less than 11 ten-day periods out of 27 (probability less than 0.41) (Fig. 2). The exception is 2013, when the probability of landfast ice occurrence between these islands and the Taimyr Peninsula was 0.66 (17 ten-day periods out of 27), while in 2012, 2016, and 2017 landfast ices of the islands of Sergei Kirov and Voronin remained isolated from the mainland landfast ice. A similar trend (a decrease in the probability of landfast ice occurrence over the considered period) was noted for the Gulfs of Ob and Gydan and the Yenisei Bay (Fig. 2).

In addition to a qualitative description of the interannual variability, the obtained polygons of the probabilities of the landfast ice position can give some quantitative characteristics: the area or linear width of the landfast ice. For example, the representation of the probability quantiles of the occurrence of landfast ice in the form of polygons will allow one to find the area occupied by the quantile of a given probability. Now, to study the interannual and climatic variability of landfast ice distribution, time series of the maximum or average area of landfast ice per year are used. The time series of areas occupied by quantiles of different probabilities may make it possible to reveal hidden patterns of interannual and climatic variability of landfast ice.

Another frequently used method for calculating the regime characteristics of the state of natural parameters subjected to seasonal variability is to analyze data separated by one year. For example, let us determine the probability of the appearance of landfast ice in the first ten days of May for the entire time of observations. The choice of the first ten days of May is because at this time the maximum landfast ice areas in the Kara Sea are observed.

Landfast ice with a probability of 1 (minimum development) is observed in the Taz Bay, the southern part of the Gulf of Ob, the Gydan Bay, the Yenisei Bay in the form of a narrow strip near the Yamal coast of the Baydaratskaya Bay, in the Malygin Strait separating Belyi Island from the Yamal Peninsula, in the Pyasinsky Bay and the waters of the Nordenskiöld Archipelago (Fig. 3). Thus, polygon $Q_{p\,=\,1}$ consists of three or four isolated regions. The polygon of the probability of detecting landfast ice is interrupted at the exits from the Gulf of Ob and the Yenisei Bay, as well as in the area of the Cape of Dickson. For all 22 years, in the first ten days of May, landfast ice has always been observed near the islands of Sergei Kirov, Voronin Island, and in the straits of the Severnaya Zemlya Archipelago.

The area, where landfast ice is observed at least once in the first ten days of May (the maximum possible development of landfast ice) is a vast polygon $Q_{p\,=\,1/22}$ connected to the mainland and including all the islands of the considered part of the Kara Sea, except for Uedineniya Island. The edges of the polygon $Q_{p\,=\,1/22}$ are located approximately 20 km north of the Izvestiya TSIK, Sergei Kirov, and Voronin islands. The distance from the islands of Izvestiya TSIK and Arctic Institute to the edge of the polygon $Q_{p\,=\,1/22}$ is about 10 km. The edge of the polygon $Q_{p\,=\,1/22}$ is located at a distance of 30 to 60 km from Vilkitsky, Shokalsky, and Belyi islands. The polygon $Q_{p\,=\,1/22}$ near the Yamal Peninsula is 30–50 km wide; near the Vaigach and Yugorsky peninsulas, its width is approximately 10 km. Uedineniya Island has a separate landfast ice (the maximum width of the landfast ice is up to 20 km). In addition, there are local areas of landfast ice isolated from the shore, which in shallow water areas can form for a short time near ice hummocks. It should also be recognized that in some cases the drifting fields of detached landfast ice on the electronic ice charts of the AARI are also designated as landfast ice.

The region of landfast ice occurrence with a probability of 0.5 is divided into three parts: landfast ice near Vaigach Island and the northern part of the Yugor Peninsula; landfast ice along the Baidaratskaya Bay, Yamal, Gulf of Ob, Gydan Bay, and Yenisei Bay shores; and landfast ice to the west of the Dikson Island along the coast of the Taimyr Peninsula and the Severnaya Zemlya Archipelago. Inside the polygon $Q_{p\,=\,0.5}$ connected to the mainland, there are the islands of Belyi, Shokalsky, Vilkitsky, Sergei Kirov, and Voronin. Isolated median polygons of landfast ice occurrence are noted near the islands of Sverdrup, Arctic Institute, Izvestiya TSIK, and Uedineniya. A part of the coast near Dikson Island is not included in the polygon $Q_{p\,=\,0.5}$; in more than 50% of cases, landfast ice is not observed in this part of the sea.

The dotted line in Fig. 3 shows the lines of the polygons of probabilities 0.25 and 0.75, obtained by two-dimensional interpolation of the coordinates of the polygon vertices. In the space between these two polygons, the landfast ice edge will be located in 50% of cases.

The distance between polygons of quartiles is called interquartile distance Q_{IQR}. As we can see from Fig. 3, the polygon of interquartile distance has a different length in different parts of the sea: in Baydaratskaya Bay and off the western coast of the Yamal Peninsula, its width is about 10 km; to the east of Be-

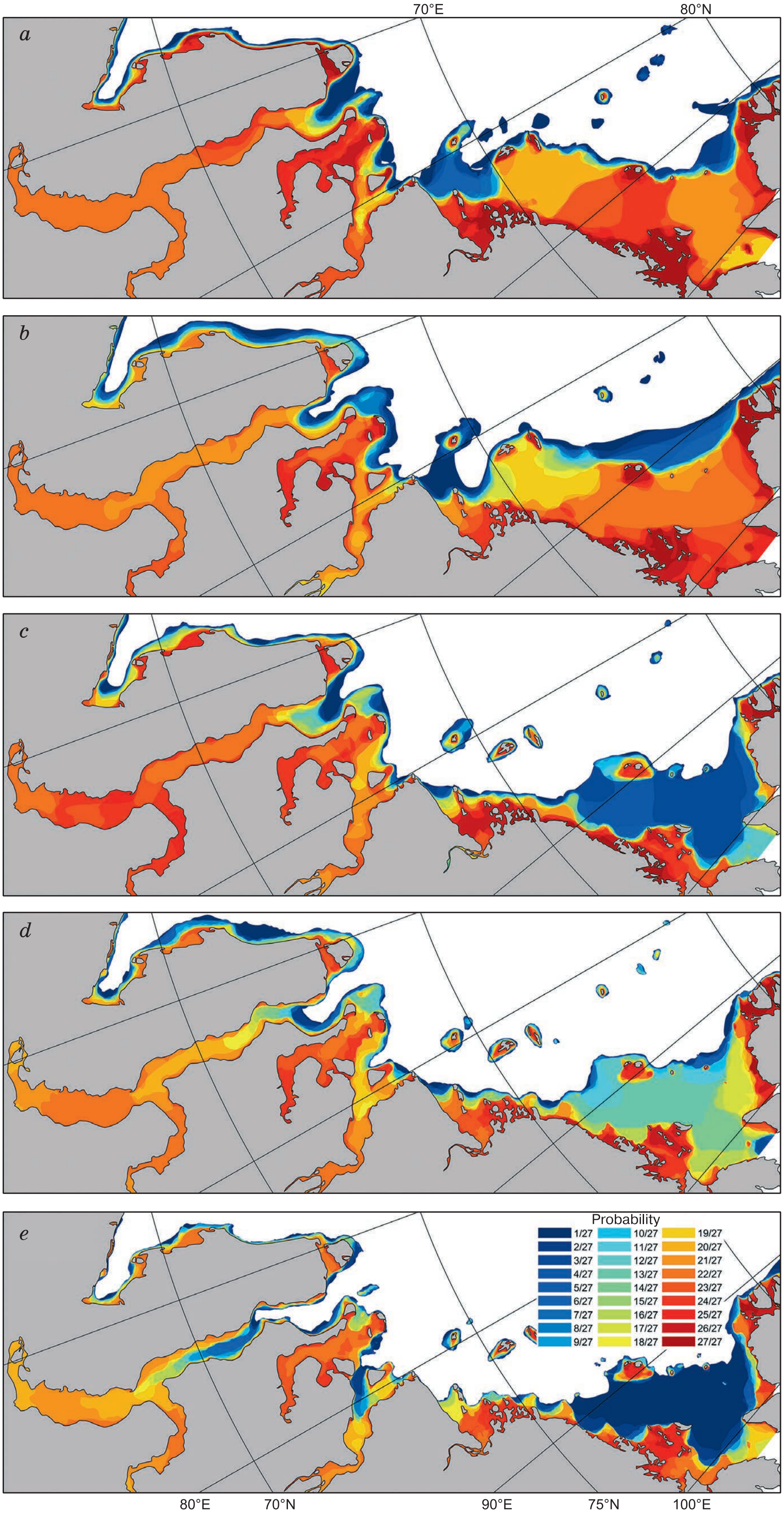
70°E
80°N
a
b
c
d
e
Probability
1/27
2/27
3/27
4/27
5/27
6/27
7/27
8/27
9/27
10/27
11/27
12/27
13/27
14/27
15/27
16/27
17/27
18/27
19/27
20/27
21/27
22/27
23/27
24/27
25/27
26/27
27/27
80°E
70°N
90°E
75°N
100°E

Fig. 2. The probability of finding landfast ice from November 1 to July 31 in different years:

(*a*) November 1999–July 2000; (*b*) November 2004–July 2005; (*c*) November 2009–July 2010; (*d*) November 2014–July 2015; (*e*) November 2019–July 2020.

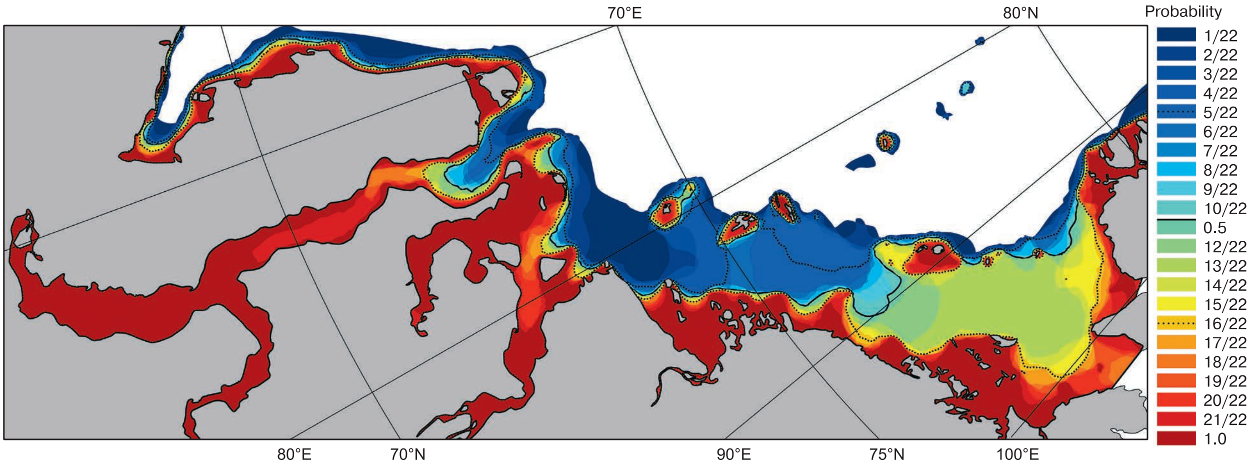

Fig. 3. Probability of landfast ice occurrence in the first ten days of May (1998–2020).

lyi Island at the entrance to the Gulf of Ob, the width of the Q_{IQR} polygon is 20 km; the maximum width (90 km) is in the Gulf of Ob itself. In the water area between the islands of the Arctic Institute and Sergey Kirov, the polygon of interquartile distance has a width of 50–100 km; to the east of the 90° E meridian, the width of the Q_{IQR} polygon increases to 100–200 km. Figure 3 shows that the islands of the Arctic Institute, Sergey Kirov, and Voronin are located inside the $Q_{p\,=\,0.25}$ quartile polygon connected to the mainland coast. The islands of Sverdrup, Izvestiya TSIK, and Uedineniya have their own isolated polygons of the quartile $Q_{p\,=\,0.25}$.

It can be seen that the faces of the interquartile polygons $Q_{p\,=\,0.25}$ and $Q_{p\,=\,0.75}$ are located asymmetrically relative to the line of the median polygon $Q_{p\,=\,0.5}$ (Fig. 3), which indicates an asymmetric distribution of the probabilities of landfast ice occurrence along the directions orthogonal to the shore and the probability polygons Q_p. Moreover, the asymmetry of the distribution changes sign: east of the 90° E meridian, the distance between polygon faces $Q_{p\,=\,0.75}$ and $Q_{p\,=\,0.5}$ is greater than the distance between polygons $Q_{p\,=\,0.25}$ and $Q_{p\,=\,0.5}$. At the entrance to the Gulf of Ob and in the water area located between the islands of the Arctic Institute and the islands of Sergei Kirov, an opposite trend is noted.

The position of the isolines of the probability of landfast ice occurrence shown in Figs. 2 and 3 are consistent with the known regime characteristics of the Kara Sea. Air temperature, bottom relief, configuration of coasts and islands, and wind and hydrological regimes determine the development of landfast ice [*Gordienko, 1971; Gudkovich et al., 1972; Gorbunov et al., 1983; Karelin, Karklin, 2012*]. The formation of landfast ice occurs after the onset of ice formation in the coastal part when young ice reaches the gray-white stage (thickness range 20–30 cm). At the beginning of the winter period, an intensive increase in the width of the landfast ice takes place, which is associated with an increase in the thickness of the ice and the strengthening of the ice plate itself. In the middle of winter, the development of landfast ice width slows down and stops altogether. The width of landfast ice can change as a result of the action of offshore or pressure winds, and periodic and surge fluctuations in sea level. In spring, due to the above-zero temperature and the flow of solar radiation, the ice begins to melt and collapse. The strength of the ice cover is significantly reduced and an abrupt decrease

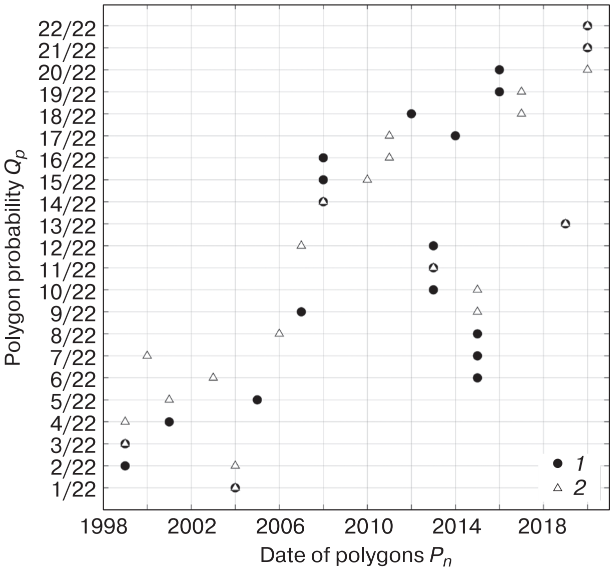

Fig. 4. Correspondence of polygons of probabilities Q_p and landfast ice polygons P_n in the first ten days of May (1998–2020) calculated as:

(*1*) minimum area of polygons $(Q_p \setminus P_n) \cup (P_n \setminus Q_p)$; (*2*) minimum difference between polygon areas Q_p and P_n.

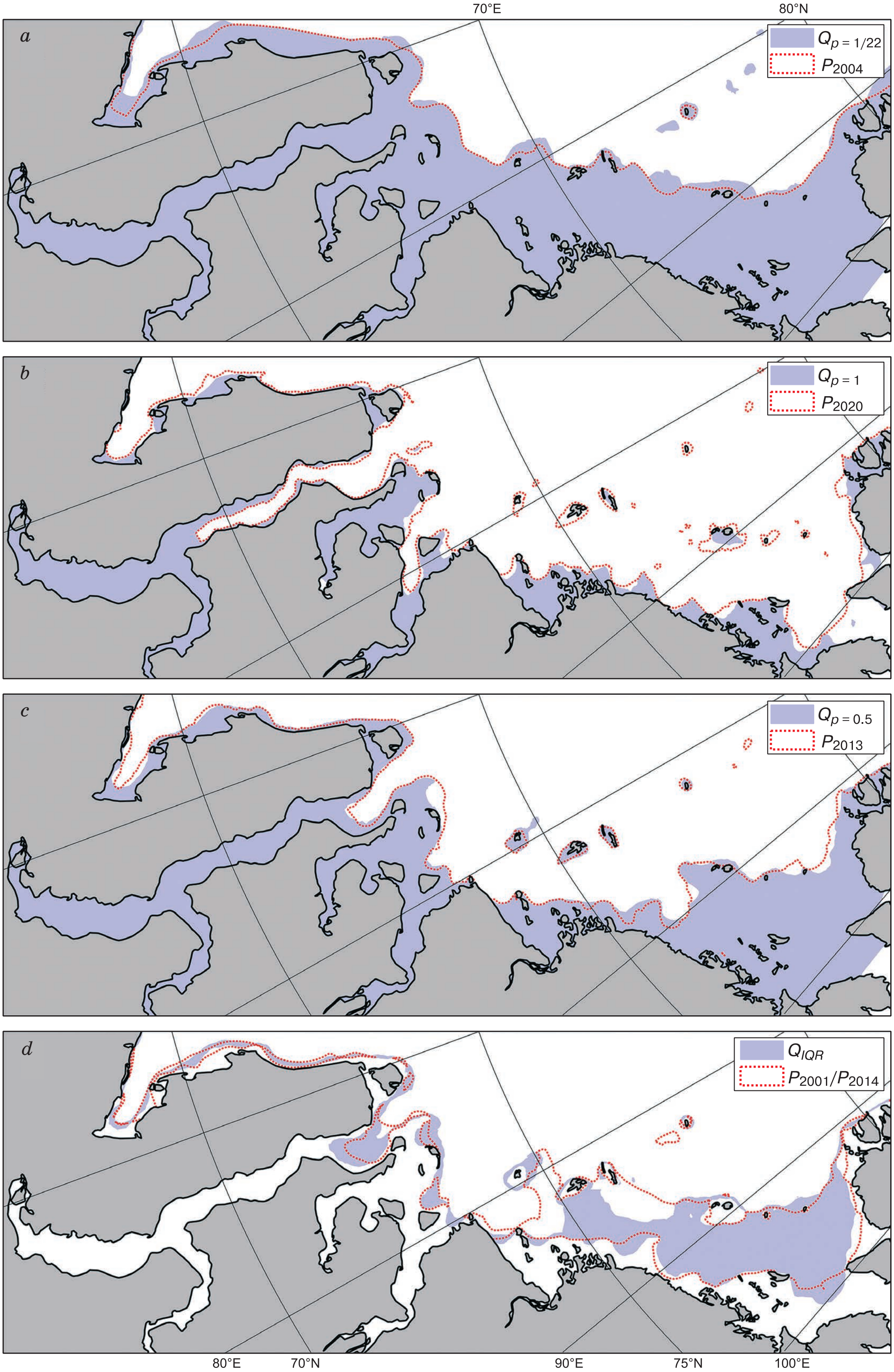
70°E
80°N
a
Q p = 1/22
P2004
b
Q p = 1
P2020
c
Q p = 0.5
P2013
d
Q IQR
P2001/P2014
80°E
70°N
90°E
75°N
100°E

Fig. 5. Areas of landfast ice occurrence in the first ten days of May with a probability of: (*a*) 1/22, (*b*) 1, (*c*) 0.5; (*d*) area of interquartile distance.

in the landfast ice width is observed; its pattern depends on the direction and strength of the wind. Breaking up of landfast ice, as a rule, starts from its seaward edge and moves towards the coast, although cases of rapid complete destruction of the entire landfast ice were sometimes noted.

Such a scheme of landfast ice dynamics determines the maximum probabilities of detecting landfast ice near the shore. Noted in Fig. 2, the trend of landfast ice area reduction is consistent with the general positive trend of air temperature changes in this area [*Karelin, Karklin, 2012*].

The resulting polygons of landfast ice detection probabilities Q_p are a complex combination of the results of combining and crossing different landfast ice fragments P_n measured from satellite images in different years. In some cases, it is required to select an analogue of the polygon of the probability of detecting landfast ice Q_p from the array of measured landfast ice boundaries in different years. Polygons-analogues were selected according to two criteria: (1) minimum area of the symmetric difference $(Q_p \backslash P_n) \cup (P_n \backslash Q_p)$ and (2) minimum difference between the areas of polygons Q_p and P_n (Fig. 4). Figure 4 shows the correspondence between the probability polygons Q_p and the landfast ice polygons P_n for the first ten days of May. There is a unidirectional trend here: in that period, polygons with high probability values of landfast ice occurrence correspond to landfast ice polygons of recent years (2014–2020); larger polygons with low probabilities correspond to landfast ice polygons surveyed in the first half of the period under consideration (1998–2008). The noted trend also indicates a decrease in landfast ice area over the past 22 years.

The polygon of the probability of finding landfast ice $Q_{p\,=\,1/22}$ should be greater than or equal to the largest landfast ice of all marked on satellite images. Therefore, for the polygon $Q_{p\,=\,1/22}$, both criteria indicated the presence of landfast ice on May 5, 2004 (Fig. 5*a*). A similar situation develops with the polygon minimally possible in terms of area $Q_{p\,=\,1}$, showing the area where landfast ice at the beginning of May was recorded during the entire period (22 years) of observation. Both criteria pointed to the last of the AARI ice charts under consideration dated May 5, 2020 (Fig. 5*b*). The median line of the landfast ice appearance (polygon $Q_{p\,=\,0.5}$) best coincides with the landfast ice recorded on May 7, 2013 (Fig. 5*c*). In other cases, the selection criteria under consideration give, as a rule, different results, and according to the criterion $(Q_p \backslash P_n) \cup (P_n \backslash Q_p)$, a more accurate coincidence of the faces of the polygons Q_p and P_n is noted. The area of interquartile distance Q_{IQR} is limited by polygons $Q_{p\,=\,0.25}$ and $Q_{p\,=\,0.75}$; landfast ice edge lines for May 7, 2014, and May 8, 2001, can be used as their analogues, respectively (Fig. 5*d*).

CONCLUSIONS

The parameters of the natural environment are n-dimensional functions ($n \geqslant 1$), which are recorded during observations as a discrete data set in n-dimensional space. With the development of numerical methods and computational technologies, there is an increasing demand to obtain and analyze data in their original form, i.e., in the form of continuous n-dimensional functions, without simplifying discretization. Thus, in recent decades, a separate direction in mathematical statistics has been distinguished – the analysis of functional data [*Ramsay, Silverman, 2005*]. This analysis, based on the use of raw data, finds application in various fields of science, including the earth sciences.

Obviously, such an analysis is also in demand in the study of the ice cover. There are several prerequisites for this: (a) in nature, the edge of drifting ice, landfast ice, and polynyas is a closed line; (b) traditionally spatially distributed ice information is summarized and recorded in the form of ice zones, which are also closed lines; (c) electronic ice charts adopted by the World Meteorological Organization are not raster images, but sets of vector polygons designed as shape-files with geoinformation reference.

In the present work, apparently, the first attempt has been made to apply the initial vector data to the analysis of information on the spatial distribution of the ice cover. Based on standard, strictly formalized and optimally implemented operations with vector polygons in many applied software libraries, algorithms for calculating the probabilities of crossing polygons were developed, with the help of which the probability (repeatability) of finding landfast ice in the Kara Sea was calculated. Formally, the method proposed by the authors cannot be classified as a method of analysis of functional data. However, it is based on the same ideology of eliminating intermediate procedures associated with the transfer of functions (polygons) into a set of discrete values (matrices or a set of sections).

The proposed method was applied to assess the probability of occurrence of landfast ice in the Kara Sea for the period from 1998 to 2020. The area of extreme distribution of landfast ice in the first ten days of May includes the islands of Vilkitsky, Shokalsky, Belyi, the Arctic Institute, Izvestiya TSIK, Sergey Kirov, and Voronin. The edge of this area is located 10–20 km north of the Izvestiya TSIK, Sergey Kirov, and Voronin islands and 30 to 60 km north of the Vilkitsky, Shokalsky, and Bely islands.

An analysis of the variability of landfast ice edge coordinates over different years showed that over the considered period of 22 years, there was a decrease in the area of landfast ice. This conclusion was confirmed both by comparing the interannual variability of the frequency of landfast ice position during the cold season and by fitting the measured polygons to different polygons of the probability of landfast ice occurrence. Landfast ice in 1998–2008 corresponds, as a rule, to polygons with the minimum probability and maximum areas, and, conversely, the landfast ice observed in May 2020 generally corresponds to the area, where landfast ice is always observed, i.e., to the polygon with the maximum probability and minimum area.

This algorithm can be applied to estimate the probability of occurrence of any data represented as polygonal features. Such objects are used in many Earth sciences, including hydrometeorology and glaciology, for example, to describe ice edges, glacier boundaries, permafrost, snow cover, and the position of certain field boundaries (isotherms, isobars, etc.). Thus, the potential scope of the proposed methodology can be much wider than the examples discussed in the article.

Acknowledgments. *This study was supported by the Russian Science Foundation, project no. 17-79-20162.*

References

Arkhipov V.V., Kokin O.V., Ogorodov S.A. et al., 2017. Landfast ice edge near the Yamal coast of the Baydaratskaya Bay of the Kara Sea in 2012–2016: its dynamics and role in the formation of modern furrows on the seabed. *Vesti gazovoy nauki* **4** (32), 129–136 (in Russian).

Atlas of Ice Formations, 2018. V.M. Smolyanitskiy (ed.). St. Petersburg, AARI, 230 pp. (in Russian).

Afanasyeva E.V., Alekseeva T.A., Sokolova Yu.V. et al., 2019. AARI methodology for sea ice charts composition. *Rossiiskaya Arktika* **7**, 5–20 (in Russian).

Divine D.V., Korsnes R., Makshtas A.P., 2004. Temporal and spatial variation of shore-landfast ice in the Kara Sea. *Continental Shelf Res.* **24** (15), 1717–1736.

Dmitrenko I.A., Gribanov V.A., Volkov D.L. et al., 1999. Impact of river discharge on the landfast ice extension in the Russian Arctic shelf area. In: *Proc. of the 15th Int. Conf. on Port and Ocean Engineering under Arctic Conditions (POAC99)* (Helsinki, August 23–27, 1999). Helsinki, Finland, 1999, pp. 311–321.

Galley R.J., Else B.G.T., Howell S.E.L. et al., 2012. Landfast sea ice conditions in the Canadian Arctic: 1983–2009. *Arctic* **65** (2), 133–144.

Gorbunov Yu.A., Karelin I.D., Kuznetsov I.M. et al., 1983. *Fundamentals of Physical and Statistical Methods of Ice Forecasting and Calculations for the Arctic Seas with a Lead Time of up to 30 Days.* Leningrad, Gidrometeoizdat, 288 pp. (in Russian).

Gordienko P.A., 1971. *Landfast ice of the Arctic seas. Parts I–II.* Leningrad, Gidrometeoizdat, 172 pp. (in Russian).

Gudkovich Z.M., Kirillov A.A., Kovalev K.G. et al., 1972. *Fundamentals of the Methodology for Long-term Ice Forecasting for the Arctic Seas.* Leningrad, Gidrometeoizdat, 348 pp. (in Russian).

Karelin I.D., Karklin V.P., 2012. *Landfast ice and Polynyas of the Arctic Seas of the Siberian Shelf in the Late XX–Early XXI century.* St. Petersburg, Izd. AARI, 180 pp. (in Russian).

Li Z., Zhao J., Su J. et al., 2020. Spatial and temporal variations in the extent and thickness of Arctic landfast ice. *Remote Sensing* **12**, 64.

Lopez-Pintado S., Romo J., 2009. On the concept of depth for functional data. *J. Amer. Statistical Assoc.* **104** (486), 718–734.

Mahoney A.R., Eicken H., Gaylord A.G., Gens R., 2014. Landfast sea ice extent in the Chukchi and Beaufort Seas: The annual cycle and decadal variability. *Cold Regions Sci. and Technol.* **103**, 41–56.

Mahoney A.R., Eicken H., Gaylord A.G., Shapiro L., 2007. Alaska landfast sea ice: Links with bathymetry and atmospheric circulation. *J. Geophys. Res.* **112** (C2), C02001.

Pavlova E.A., May R.I., Mironov E.U. et al., 2019. Methods of calculating the statistical parameters of landfast ice edge distribution. In: *Proc. of the III All-Russian Conf. Hydrometeorology and Ecology: Achievements and Development Prospects"* (St. Petersburg, Dec. 18–19, 2019). St. Petersburg, Khimizdat, pp. 669–672 (in Russian).

Ramsay J.O., Silverman B.W., 2005. *Functional Data Analysis.* New York, Springer Verlag, 429 pp.

Selyuzhenok V., Krumpen T., Mahoney A. et al., 2015. Seasonal and interannual variability of landfast ice extent in the southeastern Laptev Sea between 1999 and 2013. *J. Geophys. Res. Oceans* **120**, 7791–7806.

URL: http://wdc.aari.ru/datasets (last visited: Sept. 1, 2022).

URL: https://www.mathworks.com/matlabcentral/fileexchange/99879-probability-of-polygons-intersection (last visited: Sept. 1, 2022).

Vize V.Y., 1944. *The Foundations of Long-Range Ice Forecasting for the Arctic Seas.* Moscow, Izd. Glavsevmorputi, 272 pp. (in Russian).

Vize V.Y., 1948. *Seas of the Soviet Arcti*c. Moscow, Leningrad, Izd. Glavsevmorputi, 416 pp. (in Russian).

Volkov N.A. (ed.), 1981. *Guide to the Production of Ice Air Surveys.* Leningrad, Gidrometizdat, 239 pp. (in Russian).

WMO No. 259, 2014. *The WMO Sea Ice Nomenclature. Vol. 1. Terminology and Codes.* WMO, JCOMM Expert Team on Sea Ice, 121 pp.

Yu Y., Stern H., Fowler C. et al., 2014. Interannual variability of Arctic landfast ice between 1976 and 2007. *J. Climate* **27**, 227–243.

Zubov N.N., 1944. *Arctic Ice.* Moscow, Izd. Glavsevmorputi, 360 pp. (in Russian).

Received September 28, 2021
Revised April 9, 2022
Accepted September 14, 2022

Translated by A.V. Muravyev

EARTH'S CRYOSPHERE
SCIENTIFIC JOURNAL

Earth's Cryosphere, 2022, vol. XXVI, No. 5, pp. 35–47

GASES AND GAS HYDRATES IN THE EARTH'S CRYOSPHERE

METHANE IN FROZEN AND THAWING SEDIMENTS OF WESTERN RUSSIAN ARCTIC

N.A. Zadorozhnaya[1,*], G.E. Oblogov[1,2], A.A. Vasiliev[1,2], I.D. Streletskaya[3], G.V. Malkova[1,2], P.B. Semenov[4], B.G. Vanshtein[4]

[1] *Earth Cryosphere Institute, Tyumen Science Center, Siberian Branch of the Russian Academy of Sciences, Malygina St. 86, Tyumen, 625026 Russia*
[2] *Tyumen State University, Volodarskogo St. 6, Tyumen, 625003 Russia*
[3] *Lomonosov Moscow State University, Faculty of Geography, Department of Cryolithology and Glaciology, Leninskie Gory 1, Moscow, 119991 Russia*
[4] *All-Russia Scientific Research Institute of Geology and Mineral Resources of the World Ocean (VNIIOkeangeologia), Angliiskii prosp. 1, St. Petersburg, 190121 Russia*

Corresponding author; e-mail: z.nataliia.95@gmail.com

The results of studies of the methane content in the active layer and upper permafrost horizon in the areas of the Marre-Sale station (western Yamal Peninsula) and the Pechora River mouth are presented. Data on the methane content in Quaternary permafrost and ground ice of different geneses and data on methane emission from the surface of typical tundra in Marre-Sale are analyzed. The highest methane content in sediments of both the active layer and the upper permafrost is characteristic of boggy floodplains and waterlogged depressions on the surface of the marine terrace. In well-drained landscapes, methane is virtually absent in sediments of the active layer. In the upper permafrost, its content is 5–6 times higher than in the overlying active layer. A large amount of methane (on average, about 2 mL/kg) is contained in loamy clay marine sediments at the base of the Marre-Sale section, as well as in the massive ice. The distribution of methane in permafrost and ground ice is close to a lognormal distribution. Significant methane flux (up to 10.7 mg/(m^2·h)) has been determined for highly moistened surfaces occupying about 45–50% of the area of a typical tundra.

Keywords: *methane, permafrost, transient layer, ground ice, methane emission, Marre-Sale, Pechora River mouth.*

Recommended citation: Zadorozhnaya N.A., Oblogov G.E., Vasiliev A.A., Streletskaya I.D., Malkova G.V., Semenov P.B., Vanshtein B.G., 2022. Methane in frozen and thawing sediments of Western Russian Arctic. *Earth's Cryosphere* **26** (5), 35–47.

INTRODUCTION

The greenhouse effect on climate change cannot be assessed without taking into consideration greenhouse gases emitted to the atmosphere from natural sources. Permafrost contains enormous reserves of greenhouse gases [*Rivkina et al., 1992; Sturtevant et al., 2012; Christensen, 2014; Schuur et al., 2015; Euskirchen et al., 2017; Streletskaya et al., 2018b; van Huissteden, 2020*]. The high content of greenhouse gases in permafrost is related to the considerable content of organic matter in the Quaternary sediments of the Arctic region. Greenhouse gases – methane CH_4 and carbon dioxide CO_2 – are produced in the course of microbial decomposition of organic matter. The warming potential of methane is at least 28 times higher than the warming potential of CO_2 (over 100 years) [*IPCC, 2018*]. Continuing warming in the Arctic [*IPCC, 2018*] may lead to the emission of greenhouse gases that are currently stored in permafrost and ground ice [*McCalley et al., 2014; Dean et al., 2018*].

According to available estimates, methane emissions from Arctic ecosystems, primarily from waterlogged and boggy areas, reach 8 to 29 Tg C/yr [*McGuire et al., 2012*], which corresponds to about 10% of the global CH_4 emission from natural wetlands [*Ciais et al., 2013*]. Some researchers believe that current estimates of CO_2 and CH_4 emissions caused by dramatic permafrost thawing may be underestimated [*Anthony et al., 2018*]. The point is that the greenhouse gas emissions increase due to the expansion of waterlogged areas and thermokarst lakes, where organic carbon becomes available for microbial decomposition [*van Huissteden, 2020*]. There is also an opposite opinion stating that the emission of greenhouse gases related to permafrost degradation is not so large and may not have a significant impact on climate change [*Anisimov, 2007*].

Copyrights © 2022 N.A. Zadorozhnaya, G.E. Oblogov, A.A. Vasiliev, I.D. Streletskaya, G.V. Malkova, P.B. Semenov, B.G. Vanshtein, All rights reserved.

Methane may have abiogenic, biogenic, thermogenic, and pyrogenic origins. Biogenic CH_4 is a final product of the organic matter decomposition by methanogenic archaea in the anaerobic environments, such as waterlogged soils, bogs, and marine sediments [*Streletskaya et al., 2018a*]. In typical tundras, the biogenic CH_4 is formed in the oxygen-free water-saturated active layer and in talik zones in the presence of sufficient amount of organic carbon in available forms [*Kraev et al., 2013; Kraev, Rivkina, 2017*].

It has been experimentally found that no methane is generated in frozen sediments [*Walz et al., 2017*], i.e., the entire amount of methane emitted from frozen sediments was formed before or during freezing and is a characteristic of host sediments themselves. The same can be stated for ground ice. The microbial activity in the active layer (AL) continues until the moment of its complete freezing [*Sturtevant et al., 2012*]. It has also been confirmed that a decrease in sediment temperatures reduces the activity of methane-oxidizing microbes in the upper horizons of the active layer [*Sachs et al., 2008*].

Field observations and experiments in the northeast of Siberia demonstrated that biogenic methane tends to accumulate near the lower boundary of the AL [*Kraev et al., 2017*]. During freezing, CH_4 may be squeezed out of this layer down into the permafrost for the first few meters and accumulate in lithological “pockets”.

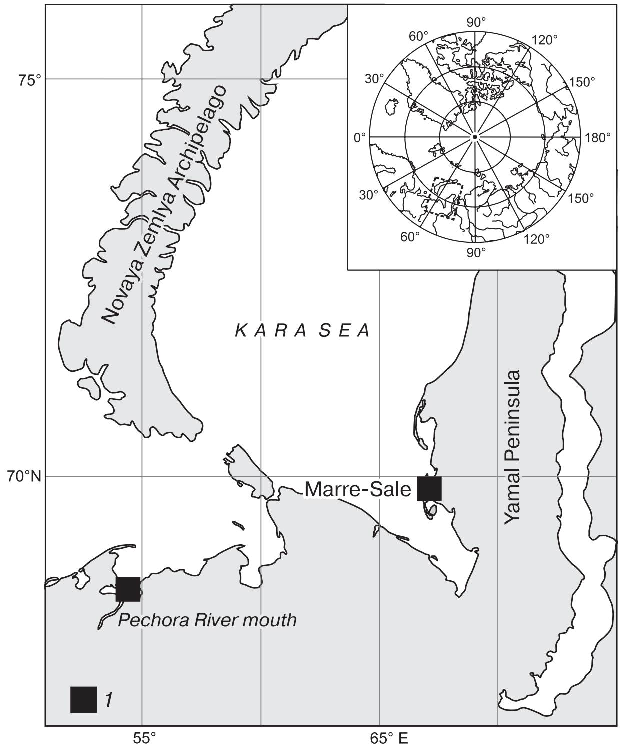

Fig. 1. Location of key sites.

1 – key site.

The aim of this study is to analyze factual data on the methane content in the AL and Quaternary permafrost, especially in the upper permafrost horizon (UPH), or the transient and intermediate layers according to Yu.L. Shur [*French, Shur, 2010*] and in the ground ice, as well as on the methane emission from the predominant landscapes of studied regions in the western sector of the Russian Arctic.

STUDY SITES

Long-term studies of the geological, geocryological, and landscape conditions have been performed in the areas of geocryological stations in the Yamal Peninsula (Marre-Sale) and the Pechora River mouth [*Pavlov et al., 2002; Kanevskii et al., 2005; Streletskaya et al., 2009, 2018a; Malkova, 2010*]. In the area of the Marre-Sale station, measurements of the methane content in the AL, permafrost and ground ice, and methane emission from the surface of predominant landscapes were performed. In the area of the Pechora River mouth, initial data on the CH_4 content in frozen and thawed sediments were obtained (Fig. 1).

The Marre-Sale Station

The Marre-Sale permafrost station is located near the weather station of the same name. The station belongs to the zone of typical tundra with maritime Arctic climate. According to the Marre-Sale weather station data, the mean annual air temperature (MAAT) from 1961 to 1990 (the period of the climatic norm) was −8.5°C. The coldest month is February with the mean monthly air temperature of −22.7°C; the warmest month is July (7.1°C). In recent decades (approximately since 1970), air temperature has been rising everywhere in the Arctic. In the studied region, the mean annual temperature has increased by about 2.8°C (1970–present), which is close to the “hard” scenario of climate change [*IPCC, 2018*]. The area belongs to the zone of continuous permafrost. Despite the presence of relatively homogeneous sandy or loamy sandy sediments in the upper part of the section, the AL depth varies from 0.3 to 2 m and more in dependence on the landscape conditions.

The landscape structure within the station area (Fig. 2) is representative of the typical tundra of Yamal Peninsula. The studied territory is located on the third marine terrace with heights from 15 to 30 m asl. The terrace is dissected by the system of ravines and runoff hollows and by deep (10–15 m) lake basins. The northern part of the territory is occupied by the wide floodplain of the Marre-Yakha River and by towpath and sea beach barrens. The floodplain is subdivided into low (regularly flooded, 0.1–0.5 m above the river water level), medium (periodically flooded, 0.5–1.5 m), and high (rarely flooded, >1.5 m) floodplain sections. The floodplain is boggy and contains numerous lakes occupying about 40% of the floodplain area. Flat areas between the lakes are occupied by polygonal herb-moss and dwarf shrub-herb-moss bogs. The total lake coverage is about 11% of the studied territory.

Herb-dwarf shrub-lichen tundras predominate on marine terraces; they are allocated to relatively drained positions between the lakes (sampling point BH6). Widespread herb-moss boggy lake depressions (point BH44) indicate the processes of active drainage of the lakes through runoff hollows. These two types of landscapes together occupy about 57% of the area, excluding the area of the lakes. Other landscape types almost equally occupy the remaining area (Fig. 2).

Hydrological conditions play an important role in the methane production in the active layer. The landscapes in the Marre-Sale area can be divided into four main classes according to their moisture content. The class of drained tundras includes sandy blowouts with fragments of tundra vegetation (point BH43) and drained polygonal tundra (point BH6).

The class of poorly drained tundras includes flat areas with wet surface covered by herb-dwarf shrub-lichen vegetation (point BH1) and the high floodplain of the Marre-Yakha River (point SB06). The class of wet tundras includes flat areas of wet herb-dwarf shrub-lichen-moss tundra (point BH3) and wet polygonal tundra with the herb-dwarf shrub-lichen-moss vegetation with small shallow ponds (points BH2, BH2a). The class of waterlogged tundras includes heavily moistened areas of ravines and runoff hollows (point BH4), lake basins (point BH44), polygonal herb-moss and dwarf shrub-moss areas of the low (point SB05) and medium (point BH36) floodplains of the Marre-Yakha River. The landscape of flat raised peatlands with the predomination of shrub-lichen-moss vegetation is distinguished separately.

The Pechora River mouth

In the European part of Russia (Nenets Autonomous District), field studies were conducted in the areas of three geocryological stations – Bolvansky, Kumzha, and Kashin – in the southern tundra subprovince of marine and alluvial accumulative plains.

The mean annual air temperature for the climatic norm period (1961–1990) is –4.7°C at the Cape Konstantinovsky weather station, which is the closest weather station to the study area. Over the last 15 years, the mean annual air temperature has risen to –2.7°C. The lowest mean annual air temperature (–9.1°C) over the entire observation period (since 1935) was recorded in 1998; and the highest mean annual air temperature (–0.7°C), in 2013. A general trend towards the mean annual air temperature rise by 0.06°C/yr has been observed in the past 30 years.

The Bolvansky station in the delta of the Pechora River on the southern coast of the Pechora Bay (the Barents Sea basin) within the gently hilly third marine plain raised at 25 to 35 m asl. The poorly drained spotty moss-lichen-dwarf shrub tundra on the tops and slopes of the hills predominates in this area. Surface sediments are represented by marine and coastal loamy sands and loams with interlayers and lenses of silty sands. Peat from 0.5 to 5 m in thickness occurs at the surface of polygonal peatlands and bogs. The territory of the station belongs to the area of continuous permafrost. Two pits were sampled at the Cape Bolvansky site. The first pit was located on the gently sloping surface of the polygonal waterlogged peatland (point 20P4). The second pit was excavated on a gently sloping surface of the polygon between runoff hollows within waterlogged peatland (point 20P6).

The Kashin geocryological station, 50 km west of the Bolvansky station, was established in 2009. It is found on Kashin Island in the Korovinskaya Bay of the Pechora River mouth, on the first marine terrace elevated at 2–10 m asl. Kashin Island is mostly com-

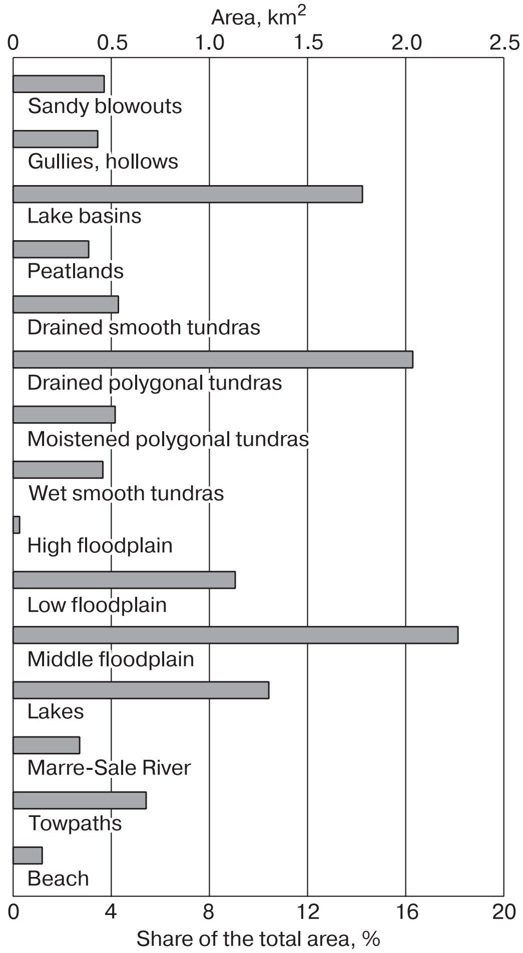

Fig. 2. Landscape structure of the Marre-Sale site.

posed of frozen sands covered with peat (up to 2 m in thickness) in some places. One pit and one exposure of the retreating coast were described and sampled. The pit was excavated on a gently inclined poorly drained surface with hillocky microtopography and lichen vegetation (point 20P3). The second sampling point was allocated to a polygonal peatland on the first alluvial–marine terrace elevated by about 1.6 m (point 20P7).

The Kumzha site was established 7 km to the south of Kashin Island, in the Pechora River delta-front, on a remnant of the first alluvial terrace at 5–8 m asl. Two pits were sampled. The first pit was laid on a slightly wavy drained surface flat-topped peatland with dwarf birch-lichen vegetation surrounded by waterlogged sedge-dominated depressions (point 20P1). The second pit was found in the central part of the depression (drained thermokarst lake) with sedge-sphagnum vegetation (point 20P2).

The Kashin and Kumzha sites belong to the zone of sporadic permafrost. The average depth of the active layer in the recent decades, according to data from CALM R24 (Bolvansky) and R24A (Kashin) sites, has been about 1.0–1.2 m.

METHODS

To determine the content of methane in frozen and thawed sediments, sediment samples of about 50 cm^3 were taken and placed in 150-mL plastic syringes after weighing. The samples were degassed using the Head Space method [*Kampbell et al., 1989*]. A highly concentrated NaCl solution and air of the known volume (about 50 cm^3) were pumped into the syringe. After complete thawing of the sample, emitted gas was pumped from the syringe into sealed 10-mL glass test-tubes with rubber corks. The samples were transported to the laboratory of the VNIIOkeangeologiya, where the gas composition was determined by gas chromatography on the SHIMADZU GC 2014 (Japan) flame ionization detector.

To determine the water content, the samples were taken in parallel with the samples for the gas composition determination.

In the late July and early August 2018, 2019, and 2020, CH_4 specific fluxes were measured in predominant landscapes in the Marre-Sale area. Isolated cubic chambers of 25 × 25 × 25 cm made of acrylic glass were used for measurements. Inside the chambers, air was automatically stirred for 15 s by fans every 10 min. Two-channel loggers HOBO Pro v2 (USA) with sensors on the surface (in a layer of the vegetation cover) and at a depth of 10 cm were installed near the chambers to measure temperature. Accuracy of the logger measurements was ±0.1°C.

Temperature was recorded every 10 min. Gas was sampled after the beginning of the experiment every hour during four hours (i.e., five measurements) by a 150-mL plastic syringe from the center of the chamber; then, gas was immediately pumped into 10-mL sealed glass test-tubes. The samples were analyzed in the laboratory of the VNIIOkeangeologiya with the use of the above-mentioned instrument. The CH_4 specific fluxes were further calculated from the slope of linear trends of the CH_4 concentration in mg/(m^2·h) taking into consideration changes in the temperature and air pressure during the experiment [*Glagolev et al., 2010*].

Data on the CH_4 concentration in sediments and ice and on the CH_4 emission were analyzed by standard statistical methods. All data were sorted into groups according to their geological and genetic background or according to the landscape characteristics of sampling sites. Mean, minimum, maximum, standard deviation, and median values were calculated for the analyzed statistical samples. The results were presented in graphs, diagrams, and figures. In box plot diagrams, the lower and upper edges of a rectangle (“box”) correspond to the first and third quartiles of the sample. The crosses in each field represent the mean methane content. The ends of the “whiskers” are the edges of a statistically significant selection (the lower end is the difference of the first quartile and one and a half interquartile distance; the upper end is the sum of the third quartile and one and a half interquartile distance). Dots on the box plot diagram designate the values of the methane content or methane flux.

RESULTS AND DISCUSSION

The methane content in the active layer and upper permafrost horizon

The methane content in the AL (regardless of the AL thickness in different years) and in the upper permafrost horizon (UPH) (to a depth of 3.6 m) in the Marre-Sale station area have been studied annually since 2012. Overall, 369 samples have been analyzed, including 249 samples in the thawed state and 120 samples in the frozen state. For the Pechora River mouth, 42 samples were taken (11 samples in the frozen state, 31 in the thawed state). The methane content was not studied in peat bogs, the Marre-Yakha River towpaths, and on the sea beach. The methane content in such areas is low due to the unfavorable conditions for significant methanogenesis [*Kwon et al., 2017*].

Figure 3 demonstrates sediment sections obtained from shallow (up to 3.6 m) boreholes: composition of the sediments, total weight water content, and the methane content in AL and UPH in different years for the area of the Marre-Sale station.

Against the background of considerable variability in the methane content in the AL, in general, there is a natural increase in the CH_4 content with depth. This probably indicates an important role of diffusion

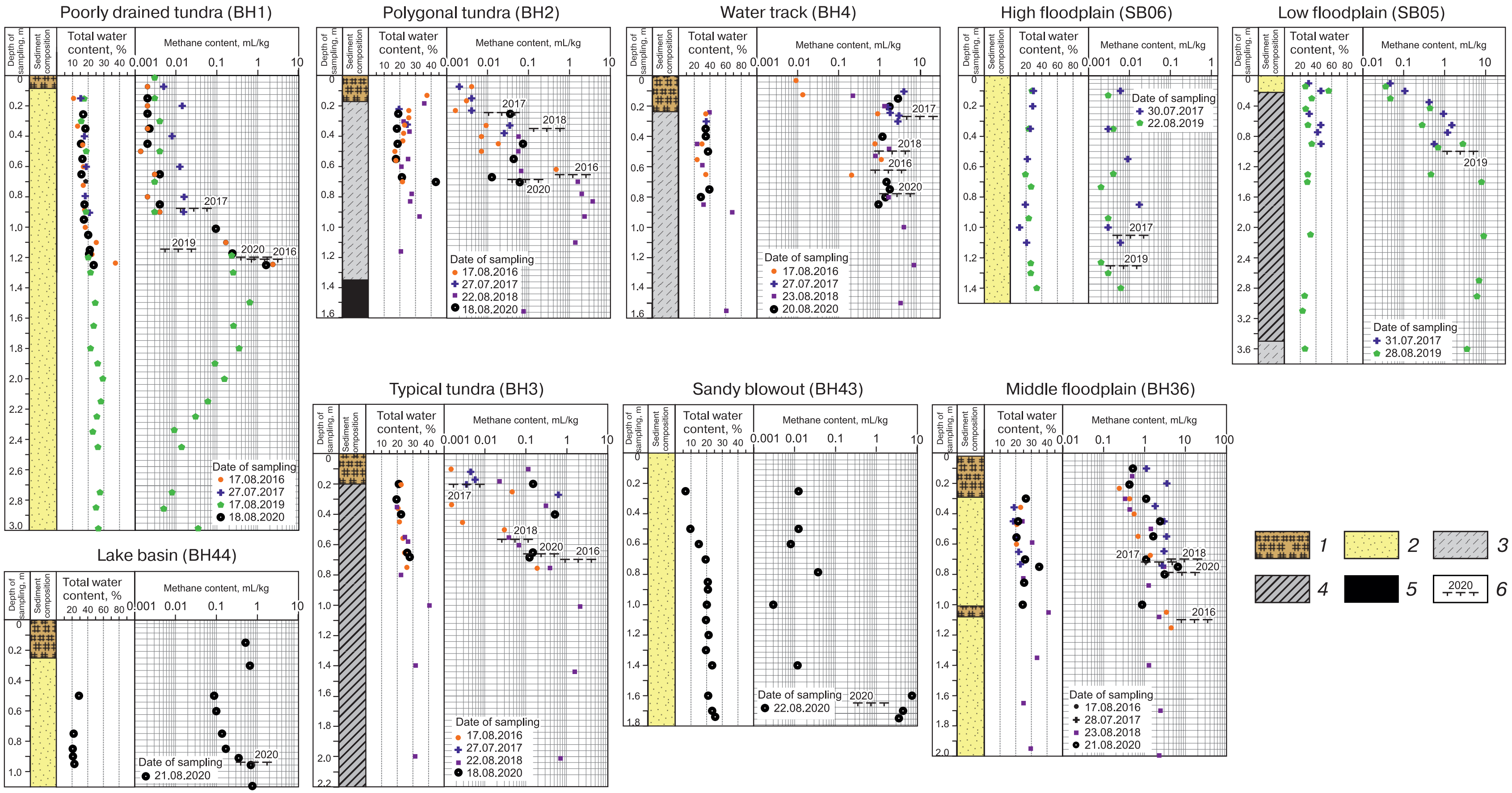

Fig. 3. Change in the methane content with depth in different types of landscapes in the Marre-Sale area.

1 – peat, *2* – sand, *3* – loamy sand, *4* – loam, *5* – ice with mineral admixtures (probably, wedge ice), *6* – boundary of the active layer at the time of drilling and the year of sampling.

mechanism of methane transfer to the surface. The amount of methane in the UPH is always higher than in the AL. The highest methane contents in both AL and UPH are typical for the most waterlogged sedge-dominated landscapes. The diffusion mechanism of the methane distribution in the AL may indicate the strong influence of methanotrophic bacteria that use methane as the only source of carbon and energy. As a rule, aerobic layers, where methanotrophic bacteria develop, are located above anaerobic zones of the methanogenesis [*Whalen, Reeburgh, 1990*].

Figure 4 demonstrates the statistical data on the CH_4 content in the AL and UPH at the Marre-Sale area. It can be seen that the CH_4 content varies considerably in dependence on a landscape. The ratio of the average CH_4 content in the landscapes with the maximum CH_4 contents to that in the landscapes with the minimum CH_4 contents is up to 400. Differences in the amount of methane are significant for the samples both from the AL and from the UPH.

In the Marre-Sale area, the highest methane content in the AL was observed in the middle floodplain of the river (point BH36) and averaged 1.59 ± 1.36 mL/kg with the maximum of 6.55 mL/kg. Almost the same values (1.57 ± 2.62 with the maximum of 9.05 mL/kg) were obtained for the low floodplain. On the main surface of the third marine terrace, the highest methane content in the AL was obtained for the moistened surface of the runoff hollows (point BH4) and averaged 1.54 ± 1.09 mL/kg with the maximum of 3.93 mL/kg. The high values of the methane content in AL were recorded in polygonal tundra (points BH2, BH2a). All other landscapes were characterized by much lower methane contents in thawed sediments (Fig. 4). In the moist typical tundra (point BH3), the average methane content was 0.13 ± 0.18 mL/kg; in point BH44 (lake basin), it was 0.28 ± 0.23 mL/kg. The methane content was less than 0.1 mL/kg in the AL of the moist flat tundra (point BH1), in drained sandy blowouts (point BH43), and in the high floodplain of the Marre-Yakha River (point SB06). On the basis of the obtained data, it can be assumed that there is a definite tendency for an increase in the methane content with an increase in the degree of surface moistening and in the water content of the AL; however, this relationship is not linear and is not observed over the entire area.

In all cases, the methane content in the UPH is higher than in the AL (Fig. 4). The difference in the ratio of the methane content in the UPH to the methane content in the AL for different types of landscapes is significant and ranges from 130–150 to 500–600% and higher. The maximum methane contents are observed near the upper permafrost horizon and 0.3–0.5 m deeper than the maximum thickness of the AL. Below, the methane content gradually decreases down the section. The similar distribution of methane was previously established for the sections in the northeastern Siberia [*Kraev, Rivkina, 2017*].

In general, the high methane contents in the UPH were obtained for sampling points BH43, BH36, BH4, BH2a, and SB05, i.e., for the same landscapes, where the high methane content was observed in the AL. In a single case (point BH43, drained surface of a sandy blowout), the high methane content values were obtained for the underlying frozen sediments (the average methane content 5.14 ± 1.9 mL/kg with the maximum value of 7.29 mL/kg), though in the AL, the methane content was exceptionally low. This can be explained by a high degree of drainage of the upper sandy horizon, which does not provide the anaerobic conditions and the methane formation.

In the area of the Pechora River mouth, the CH_4 content was determined at the sites within several landscape structures (Fig. 5).

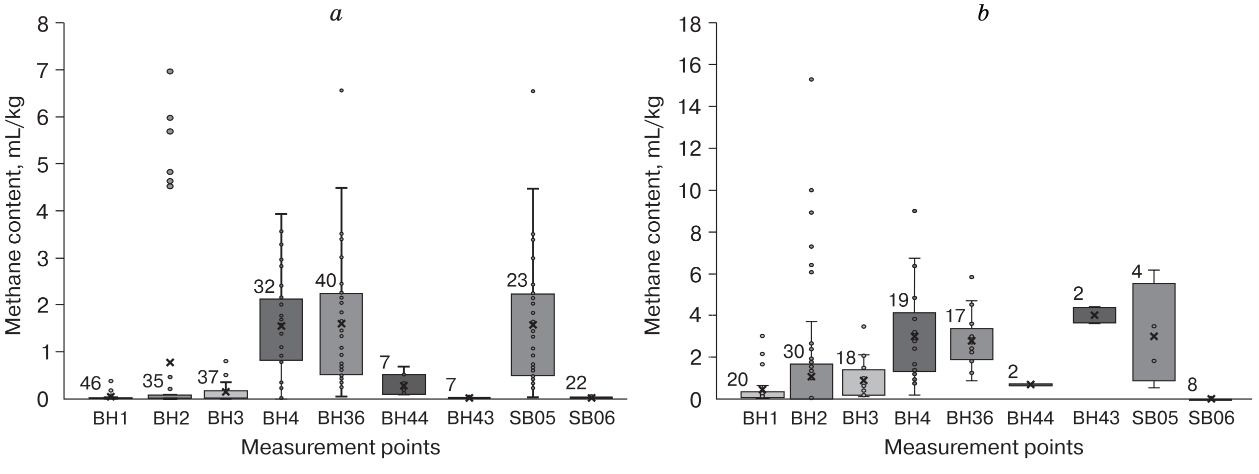

Fig. 4. Box-plot diagrams of the methane content at observation points in the Marre-Sale area in the (*a*) active layer and (*b*) upper permafrost horizon.

Figures indicate the number of samples.

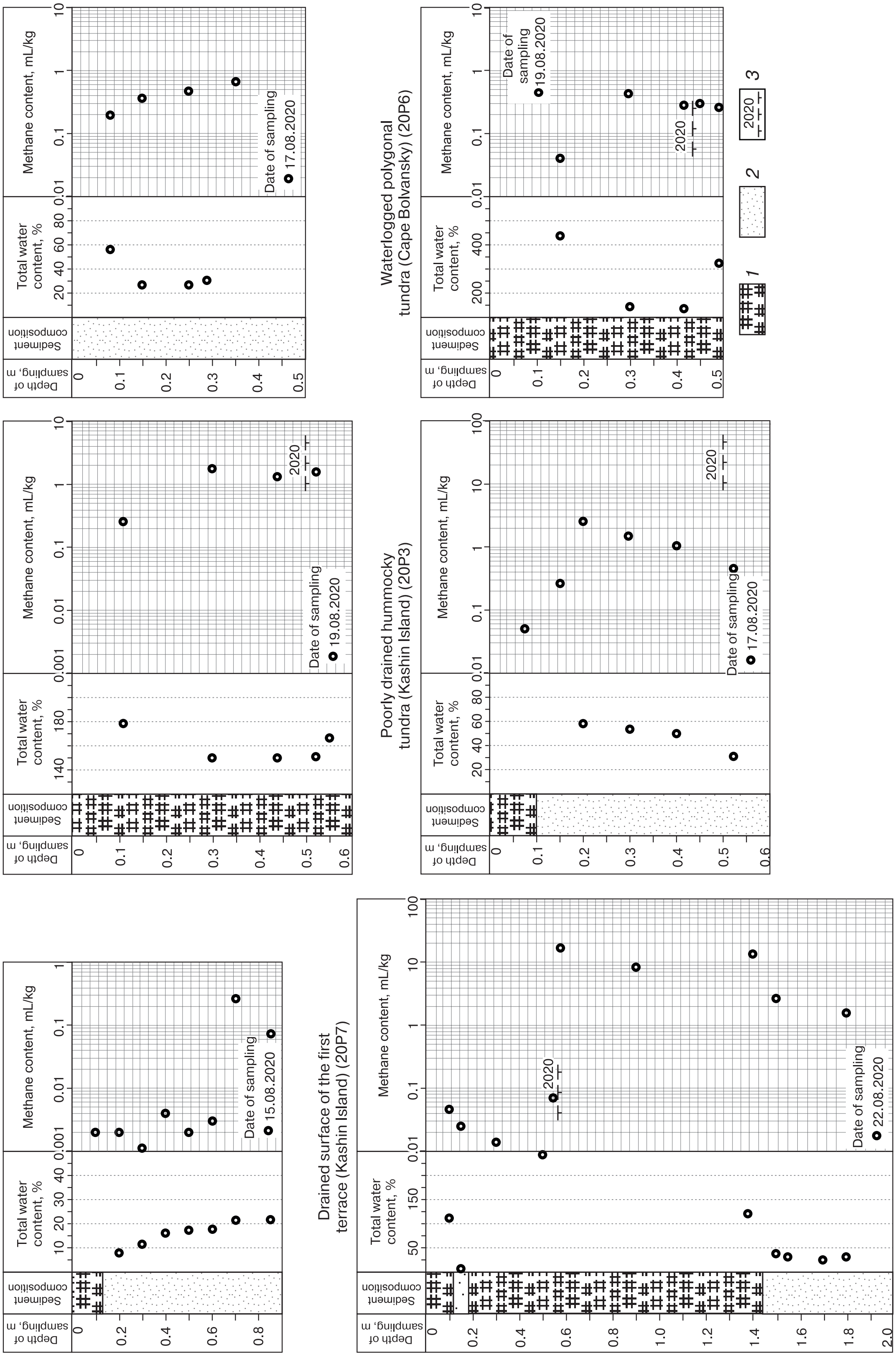

Fig. 5. Changes in the methane content by depth in different types of landscapes near the mouth of the Pechora River.

1 – peat; *2* – sand; *3* – boundary of the active layer at the time of drilling and the year of sampling.

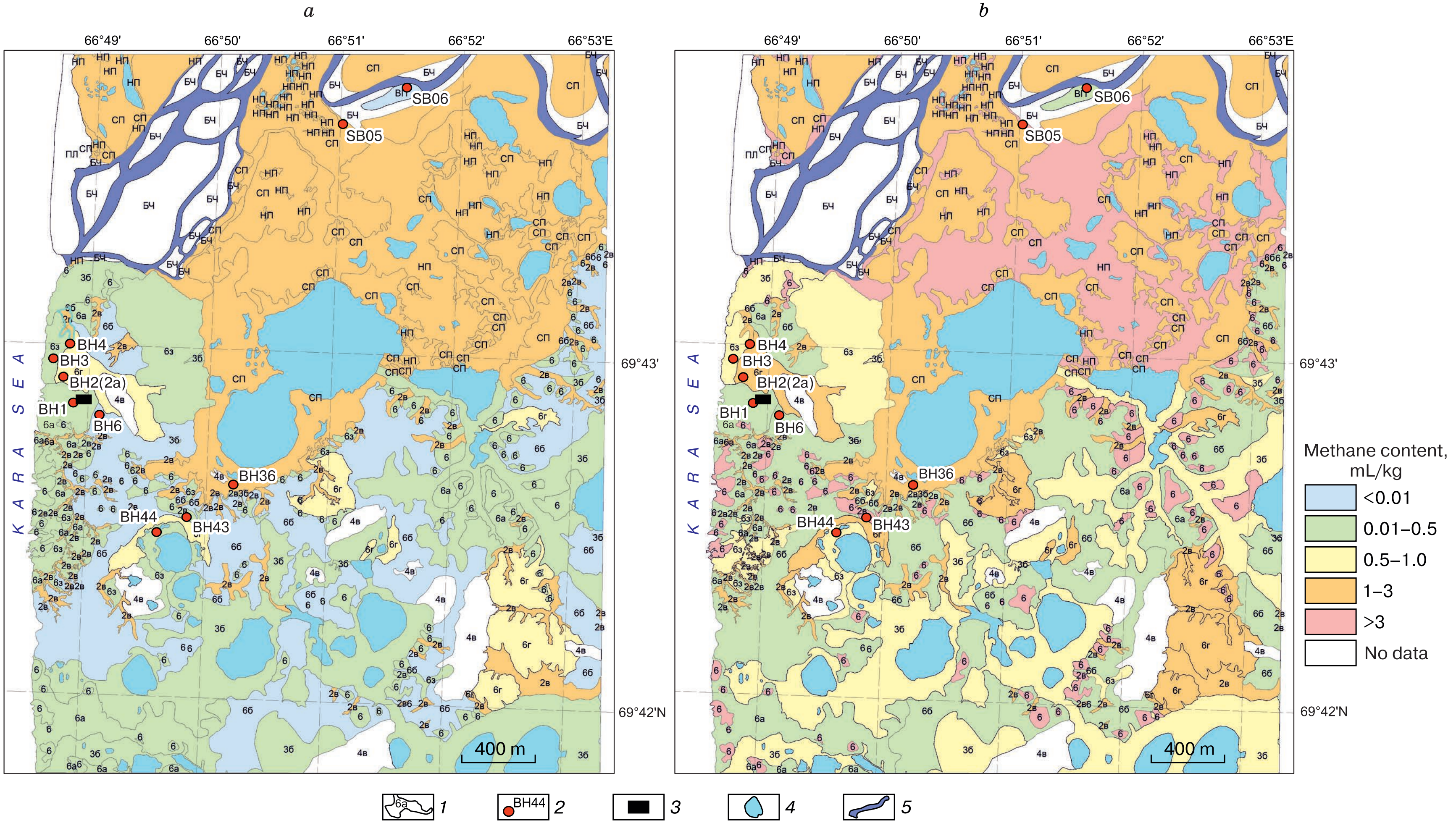
a
b
66°49'
66°50'
66°51'
66°52'
66°53'E
69°43'
69°42'N
KARA SEA
BH1
BH2(2a)
BH3
BH4
BH6
BH36
BH43
BH44
SB05
SB06
400 m
Methane content, mL/kg
<0.01
0.01–0.5
0.5–1.0
1–3
>3
No data
1
2
3
4
5

Fig. 6. Maps of the average methane content in the predominant landscapes of the Marre-Sale area in the (*a*) thawed sediments of the active layer and (*b*) upper permafrost horizon.

1 – landscape boundary and index (2c(2в) – gullies and water tracks, 3b(3б) – lake basins, 4c(4в) – peatlands, 6 – sandy blowouts, 6a(6a) – drained smooth tundras, 6b(6б) – drained polygonal tundras, 6d(6г) – waterlogged polygonal tundras, 6z(6з) – wet smooth tundras, LF(НП) – low floodplain, MF(СП) – middle floodplain, HF(ВП) – high floodplain, SB(ПЛ) – sea beach, TP(БЧ) – unvegetated zones between floodplain and seashore (towpaths)); *2* – sampling point and its index; *3* – Marre-Sale weather station; *4* – lakes; *5* – Marre-Yakha River.

The high methane content in thawed sediments of the AL near the Pechora River mouth was recorded at sampling sites 20P3 and 20P4; the average CH_4 contents were 1.24 ± 1.08 mL/kg (maximum 2.5 mL/kg) and 1.1 ± 0.83 mL/kg (maximum 1.9 mL/kg), respectively. At point 20P2, the average methane content in the AL was 0.42 ± 0.2 mL/kg (maximum 0.67 mL/kg); at point 20P6, the average value was 0.24 ± 0.19 mL/kg (maximum 0.41 mL/kg). At points 20P1 and 20P7, the CH_4 concentrations were insignificant, less than 0.05 mL/kg. The given data, as well as the data for the Marre-Sale territory, indicate some increase in the amount of CH_4 in the more moistened landscapes compared to the drained surfaces.

Frozen sediments in the UPH were sampled at points 20P3, 20P4, 20P6, 20P7. The CH_4 content in them was higher than in the AL for all points, except for 20P3. The maximum values were obtained for frozen sediments in the coastal cliff on Kashin Island (point 20P7); they average CH_4 content was 8.15 ± 6.14 mL/kg (maximum 15.78 mL/kg). In other points, the average methane content comprised 1.68 mL/kg (20P4), 0.46 mL/kg (20P3), 0.3 mL/kg (20P6).

The maps illustrating the spatial distribution of methane in the AL and UPH are presented in Fig. 6. The earlier created landscape map of the study area [*Oblogov et al., 2020*] was used as the base map. To show the methane content in sediments, average data obtained at sampling points were sorted into five unequal gradations shown by color on the map.

The maps clearly illustrate the spatial distribution of methane in the AL and UPH and allow us to estimate the amount of methane that will be emitted into the atmosphere for different scenarios of climatic warming and permafrost degradation under the typical tundra conditions.

Methane in permafrost and ground ice of the Marre-Sale Area

Data on the methane content in the Quaternary permafrost and ground ice of the Marre-Sale area were obtained by studying coastal cliffs of 10 to 30 m in height (Fig. 7) [*Kanevskii et al., 2005; Streletskaya et al., 2009, 2018a*].

In the upper part of the section, fine-grained alluvial sands of the Holocene age (aIV) are exposed. They have the lowest CH_4 content among all geological varieties; the average value is 0.08 ± 0.1 mL/kg; the maximum value is 0.35 mL/kg.

Continental layered silty loamy sands and sands of lacustrine-bog (lbIII^4) or coastal-marine (amIII$^{3-4}$) origin underlie Holocene sands. The CH_4 content in these sediments is an order of magnitude higher than in the Holocene sands; it averages 0.87 ± 1.13 mL/kg with a maximum of 3.81 mL/kg.

Loamy sands and sands (amIII$^{3-4}$) were formed within the vast coastal plain with numerous lakes [*Streletskaya et al., 2009*]. These sediments are characterized by the high variability in the CH_4 content, with the maximum value of 6.75 mL/kg and the average value of 0.46 ± 1.16 mL/kg.

The base of the section is composed of clay and loamy sediments with interlayers of sands of the Late Pleistocene age (mIII^1) of the marine and coastal-marine origin. The silty clay sediments are most enriched in CH_4 content: 1.94 ± 1.62 mL/kg (average) and 6.77 mL/kg (maximum).

The am III$^{3-4}$ sediments in the middle part of the section contain subhorizontal lenses and interlayers of ice with wave-like bends and single mineral inclusions. The pure ice layers with a thickness from a few centimeters to 1.5 m (0.2–0.5 m on average) alternate with sandy (loamy sandy) interlayers. The ice contains irregularly distributed bubbles, 1–2 mm in diameter of a rounded or poorly elongated shape, in

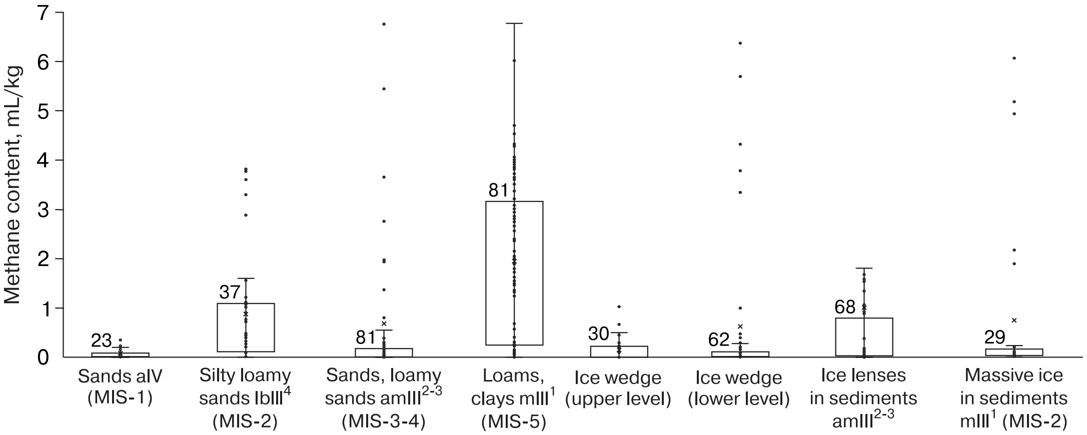

Fig. 7. Box-plot diagrams of the methane content in the Quaternary frozen sediments and ground ice in the area of the Marre-Sale coastal cliff.

Figures indicate the number of samples.

which gas occurs under pressure. The amIII$^{3-4}$ sequence of sandy sediments with inclusions of ice lenses and interlayers is visually seen as a single ice-rich horizon and is united into the horizon of massive ice of the first type (MI 1). The ice lenses contain the significant amount of methane. The average methane content is 0.98 ± 3.25 mL/kg. The absolute maximum is 23.29 mL/kg was determined in a sample from the ice lens in the amIII$^{3-4}$ sediments. This is the maximum value among all sampled sediments.

Thick massive ice of the second type (MI 2) is exposed 3.0–3.5 km to the south of the polar station in the thickness of the mIII^{1} loamy clay sediments. The apparent thickness of the ice body is more than 8 m; the lower part descends under sea level. The ice is almost clear and glassy, but there are zones with a significant number of admixtures of mineral inclusions (mainly clayey and silty fractions) in the form of suspended matter. Ice includes small irregularly distributed gas bubbles and their clusters. Gas in the bubbles is under pressure. The average methane content in the MI 2 samples is 0.76 ± 1.69 mL/kg; the maximum reaches 6.07 mL/kg.

There are two generations of ice wedges (IW) in the section. The Holocene IW of the upper level is distinctly wedge-shaped and often superimposes the lower-level of older wedges. The wedges with a width of 0.5–1.2 m at the top and 1.0–3.5 m in height form a polygonal network; the size of polygon sides is 6–8 m. The wedges are of the syngenetic type of growth, as indicated by the relatively high ice content of host sands and peat. Wedge ice contains numerous vertically oriented gas bubbles of up to 3 mm in size. The average methane content in the samples of IW of the Holocene age is 0.15 ± 0.24 mL/kg; the maximum value is 1.03 mL/kg.

Large ice wedges began to form at the end of MIS-3 (Marine Isotope Stage 3) and continued active growth in MIS-2 [*Forman et al., 2002*]. The wedges of 1.5–4.0 m in width and up to 10 m in height form a polygonal network of 10–20 m in size. The wedges are syngenetic, as indicated, in particular, by the repeatedly encountered layered cryogenic structure of the host sediments. The wedge tails in the central part of the coastal cliff are involved in the MI 1 massif, branching and bending in different directions. The IW is transparent, with thin vertically oriented interlayers of mineral inclusions of sandy silt fraction. Numerous gas bubbles 0.1–2.0 mm in size extend vertically in the ice. The average methane content of the Pleistocene IW samples is 0.63 ± 1.89 mL/kg, with the maximum value of 11.11 mL/kg.

The CH_4 concentrations within the same geological and genetic variety can differ by several orders

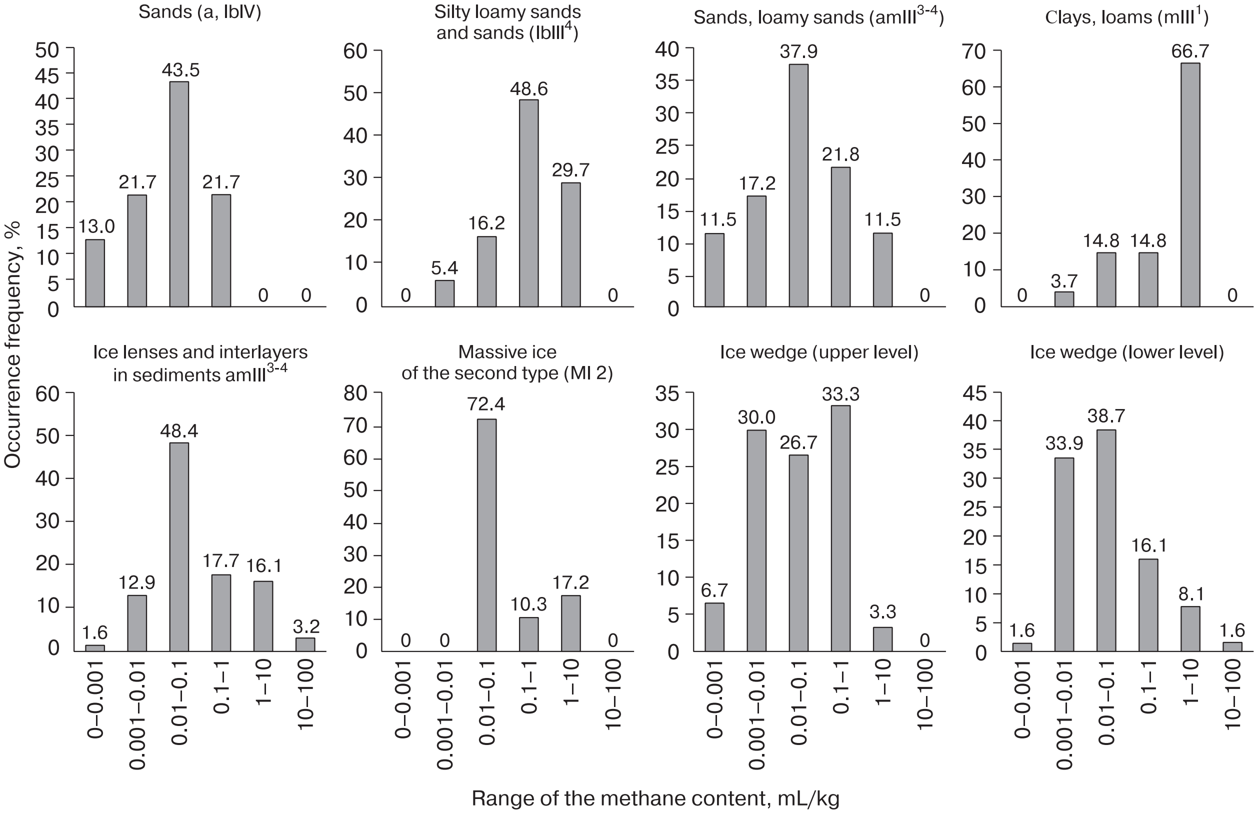

Fig. 8. Methane contents in different genetic types of frozen sediments and ground ice in the Marre-Sale area.

of magnitude, in dependence on the place of sampling. This is primarily relevant to massive ice areas, where completely different values were obtained in samples taken within a few tens of centimeters from one another. Figure 8 demonstrates the distributions of the CH$_4$ content in the Quaternary frozen sediments and ground ice in the Marre-Sale area.

It is evident that in most of the considered geological-genetic varieties, the pattern of the CH$_4$ distribution is close to the lognormal one. In general, the maximum values range from 0.01 to 0.10 mL/kg. Significant deviations from the lognormal distribution are observed only for marine loamy clay sediments mIII^1, where the values ranging from 1 to 10 mL/kg distinctly predominate, and for MI 2, where the range of 0.01 to 0.10 mL/kg predominates.

The obtained data point to the high methane content in the Quaternary permafrost and ground ice. Nevertheless, each geological and genetic type is characterized by its own methane content indicating the influence of the conditions of sediment deposition and freezing. Thus, methane can act as an additional indicator for geocryological subdivision of frozen sediments.

Emission of methane from the surface of the predominant landscapes of Marre-Sale

The specific CH$_4$ efflux to the atmosphere (methane emission) was measured in the Marre-Sale area in the late July – early August in 2018, 2019, and 2020 at nine key points (BH1, BH2, BH2a, BH3, BH4, BH36, BH44, SB05, SB06) within eight dominant landscapes.

The measurements were not performed in peatlands, drained surface of sandy blowouts, Marre-Yakha River towpath, and the sea beach. For similar types of landscapes, it was previously established that methane efflux is virtually absent [*Kwon et al., 2017*].

Twenty six four-hour experiments were conducted at the surface temperatures from 5.7 to 20.0°C. Figure 9 demonstrates the results of the measurements.

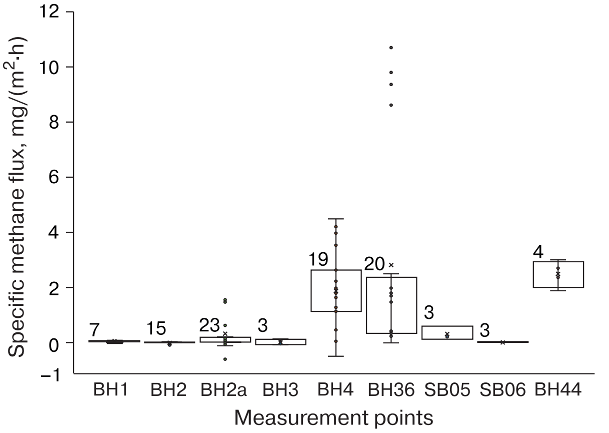

Fig. 9. Box-plot diagrams of the specific methane flux from predominant landscapes of Marre-Sale area.

Figures indicate the number of samples.

There are several types of landscapes with high positive values of the specific methane fluxes. These are the waterlogged floodplain (points BH36 and SB05), the heavily moistened runoff hollows (point BH4), the waterlogged surface of the lake basin (point BH44), and the highly moistened surface of the polygonal depression (point BH2a). The maximum value of the specific methane flux (10.7 mg/(m^2·h) was obtained in point BH36 at the surface temperature of 20.0°C. In point BH4, the maximum methane flux was 4.5 mg/(m^2·h) at the surface temperature of 16.9°C; in point BH44, these values were 2.99 mg/(m^2·h) and 17.1°C, respectively. The greatest methane flux at point BH2a (1.5 mg/(m^2·h)) was obtained at the surface temperature of 13.1°C. In other points, the specific flux values were always less than 0.1 mg/(m^2·h). Approximately the same methane fluxes were measured earlier in various ecosystems of Alaska in the zone of continuous permafrost [*Euskirchen et al., 2017*].

The relationship between the specific methane fluxes and the surface temperature at the time of sampling clearly demonstrates a tendency for the increase in the methane fluxes with a rise in the surface temperature (Fig. 10). This is best manifested for the landscapes with large methane fluxes. In particular, at

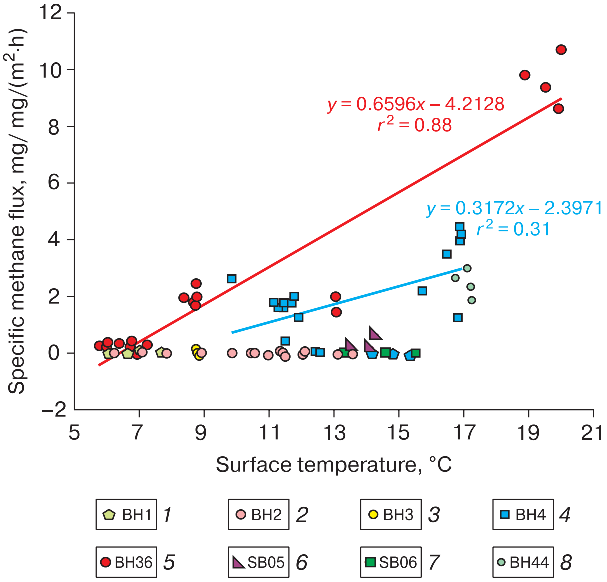

Fig. 10. The relationship between the specific methane fluxes and the surface temperature at measurement points in the predominant landscapes of the Marre-Sale area.

1–8 – measurement points (*1* – drained smooth tundra, *2* – drained polygonal tundra, *3* – wet smooth tundra, *4* – runoff hollow, *5* – middle floodplain, *6* – low floodplain, *7* – high floodplain, *8* – lake basin). Linear trends are presented for some data sequences.

point BH36, we can distinguish three temperature ranges, at which we measured the methane fluxes. At the surface temperature of 5.7 to 7.2°C, the lowest methane flux close to zero or negative was observed. At the surface temperature of 8–9°C, the methane flux increased significantly and reached 1.68–2.47 mg/(m^2·h). The highest methane flux of 8.6–10.7 mg/(m^2·h) at point BH36 was obtained at the surface temperatures from 18.8 to 20.0°C.

CONCLUSIONS

As a result of the studies conducted in the Marre-Sale area, new statistically reliable data on the methane content in the AL and the underlying UPH (transient and intermediate permafrost layers) were obtained.

In Marre-Sale, the highest methane content in the AL was recorded in the waterlogged landscapes of the middle and low floodplains; it averaged 1.59 ± 1.36 and 1.57 ± 2.62 mL/kg, respectively. For the third marine terrace, the high methane content in the AL was obtained for the waterlogged runoff hollows and for the polygonal tundra. In well-drained landscapes (drained surface of typical tundra, sandy blowouts, etc.), the lowest methane content in the AL was observed. A typical increase in the CH_4 content with depth in the AL probably indicates an important role of methane diffusion to the surface.

In the UPH sediments, the methane content is up to 5–6 times higher than in the AL and averaged 3 mL/kg. The high methane content in the UPH was obtained for the landscapes, in which the high methane content was also observed in the AL. The high CH_4 content in the UPH is explained by penetration of methane into the underlying layers during the autumn freezing of the AL.

The transient layer of permafrost with the high content of methane can be considered as a significant potential source of methane, which may be involved in the turnover of greenhouse gases in the atmosphere during the permafrost degradation.

The content and distribution of methane in various geological and genetic types of the Quaternary permafrost and ground ice of different origins in the Marre-Sale area were analyzed. The highest methane concentrations were found in the loamy clay sediments of marine origin (mIII^1) (on average, about 2 mL/kg with a maximum of 6.77 mL/kg). These sediments occur at the base of the section and constitute a larger part of the sediments exposed in the coastal cliff. High methane contents were also established for ground ice of the area. The absolute maximum of the methane content (23.29 mL/kg) was obtained in the interlayers and lenses of glassy ice in the alluvial-marine (coastal-marine) sandy loams and sands (amIII$^{3-4}$); although, in this type of ice, the average methane content did not exceed 1 mL/kg. It was shown that the methane content within the same genetic type of sediments can differ by several orders of magnitude in dependence on the local conditions of particular sampling sites. The methane distribution pattern for most of the distinguished genetic types of frozen sediments and ground ice is close to lognormal.

The peak values of the specific methane fluxes into the atmosphere from the surface of typical tundra landscapes in the Marre-Sale area were determined. Stable and significant methane fluxes were observed for the waterlogged surface of the low and middle floodplains, waterlogged runoff hollows, waterlogged surfaces of lake basins, and highly moistened surfaces of polygonal depressions. The maximum value of methane flux (10.7 mg/(m^2·h)) was obtained on the middle floodplain at the surface temperature of about 20.0°C. On the surfaces of the poorly moistened and drained landscapes, the specific methane fluxes are always less than 0.1 mg/(m^2·h). Taking into consideration the landscape structure of the Marre-Sale area, the sources of significant methane emissions occupy 45–50% of the territory.

Acknowledgments. *This work was supported by the Russian Science Foundation (grant no. 22-27-00181). Cryolithological studies were conducted within the framework of the Development Program of the Interdisciplinary Research and Education School at Lomonosov Moscow State University "The Future of the Planet and Global Environmental Change" and state assignment no. 121051100164 "Evolution of the Cryosphere under Climate Change and Human Impact".*

References

Anisimov O.A., 2007. Potential feedback of thawing permafrost to the global climate system through methane emission. *Environ. Res. Lett.* **2**, 1–7. DOI: 10.1088/1748-9326/2/4/045016.

Anthony K.W., von Deimling T.S., Nitze I. et al., 2018. 21st-century modeled permafrost carbon emissions accelerated by abrupt thaw beneath lakes. *Nat. Commun.* **9**, 3262. DOI: 10.1038/s41467-018-05738-9.

Christensen T.R., 2014. Understand Arctic methane variability. *Nature* **509**, 279–281. DOI: 10.1038/509279a.

Ciais P., Sabine H.C., Bala G. et al., 2013. Carbon and Other Biogeochemical Cycles. In: *Climate Change 2013: The Physical Science Basis. Contribution of Working Group I to the Fifth Assessment Report of the Intergovernmental Panel on Climate Change* [T.F. Stocker, D. Qin, G.-K. Plattner, M. Tignor, S.K. Allen, J. Boschung, A. Nauels, Y. Xia, V. Bex, P.M. Midgley (eds.)]. Cambridge, UK and NY, USA, Cambridge Univ. Press, pp. 465–570.

Dean J.F., Middelburg J.J., Röckmann T. et al., 2018. Methane feedbacks to the global climate system in a warmer world. *Rev. Geophys.* **56**, 207–250. DOI: 10.1002/2017RG000559.

Euskirchen E.S., Bret-Harte M.S., Shaver G.R. et al., 2017. Long-Term Release of Carbon Dioxide from Arctic Tundra Ecosystems in Alaska. *Ecosystems* **20**, 960–974. DOI: 10.1007/ s10021-016-0085-9.

Forman S.L., Ingolfsson O., Gataullin V. et al., 2002. Late Quaternary stratigraphy, glacial limits and paleoenvironments of Maresale area, western Yamal Peninsula, Russia. *Quatern. Res.* **21**, 1–12.

French H., Shur Y., 2010. The principles of cryostratigraphy. *Earth Sci. Rev.* **101** (3–4), 190–206. DOI: 10.1016/ j.earscirev.2010.04.002.

Glagolev M.V., Sabrekov A.F., Kazantsev V.S., 2010. *Measurement of Gas Exchange at the Soil / Atmosphere Boundary.* Tomsk, Tomsk State Pedagogical Univ., 96 pp. (in Russian).

IPCC, 2018. Global Warming of 1.5°C. An IPCC special report on the impacts of global warming of 1.5°C above preindustrial levels and related global greenhouse gas emission pathways. In: *The Context of Strengthening. The Global Response to the Threat of Climate Change, Sustainable Development, and Efforts to Eradicate Poverty.* V. Masson-Delmotte, P. Zhai, H.-O. Pörtner et al. (Eds.). Cambridge, New York, Ridge Univ. Press, 616 pp. DOI: 10.1017/9781009157940.

Kampbell D.H., Wilson J.T., Vandegrift S.A, 1989. Dissolved oxygen and methane in water by a GC Headspace Equilibration Technique. *Intern. J. Environ. Analytic. Chemistry* **36** (4), 249–257. DOI: 10.1080/03067318908026878.

Kanevsky M.Z., Streletskaya I.D., Vasiliev A.A., 2005. Formation of cryogenic structure of Quaternary sediments in Western Yamal (by the example of Marre-Sale area). *Kriosfera Zemli* **9** (3), 16–27 (in Russian).

Kraev G.N., Rivkina E.M., 2017. Accumulation of methane in freezing and frozen soils of the permafrost zone. *Arctic Environ. Res.* **17** (3), 173–184. DOI: 10.17238/issn2541-8416.2017.17.3.173 (in Russian).

Kraev G., Schulze E.-D., Yurova A. et al., 2017. Cryogenic displacement and accumulation of biogenic methane in frozen soils. *Atmosphere* **8** (6), 105. DOI: 10.3390/at-mos8060105.

Kraev G.N., Schulze E.-D., Rivkina E.M., 2013. Cryogenesis as a factor in the distribution of methane in frozen horizons. *Dokl. Akad. Nauk* **451** (6), 684–687 (in Russian).

Kwon M.J., Beuli F., Ilie I. et al., 2017. Plants, microorganisms, and soil temperatures contribute to a decrease in methane fluxes on a drained Arctic floodplain. *Glob. Chang. Biol.* **23**, 2396–2412. DOI: 10.1111/gcb.13558.

Malkova G.V., 2010. Mean-annual ground temperature monitoring on the steady-state-station "Bolvansky". *Kriosfera Zemli* **14** (3), 3–14 (in Russian).

McCalley C., Woodcroft B., Hodgkins S. et al., 2014. Methane dynamics regulated by microbial community response to permafrost thaw. *Nature* **514**, 478–481. DOI: 10.1038/nature13798.

McGuire A.D., Christensen T.R., Hayes D. et al., 2012. An assessment of the carbon balance of Arctic tundra: comparisons among observations, process models, and atmospheric inversions. *Biogeosciences* **9**, 3185–3204. DOI: 10.5194/bg-9-3185-2012.

Oblogov G.E., Vasiliev A.A., Streletskaya I.D. et al., 2020. Methane content and emission in the permafrost landscapes of Western Yamal, Russian Arctic. *Geosciences* **10** (10), 412. DOI: 10.3390/geosciences10100412.

Pavlov A.V., Anan'eva G.V., Drozdov D.S. et al., 2002. Monitoring of active layer and the temperature of frozen grounds in the north of Russia. *Kriosfera Zemli* **6** (4), 30–39 (in Russian).

Rivkina E.M., Samarkin V.A., Gilichinskiy D.A., 1992. Methane in permafrost of the Kolyma-Indigirka Lowland. *Dokl. Ross. Akad. Nauk* **323** (3), 559–562 (in Russian).

Sachs T., Giebels M., Wille C. et al., 2008. Methane emission from Siberian wet polygonal tundra on multiple spatial scales: Vertical flux measurements by closed chambers and eddy covariance, Samoylov Island, Lena River Delta. In: *Proc. 9th Intern. Conf. Permafrost* (Fairbanks, Alaska, 29 June–3 July, 2008), Fairbanks, pp. 1549–1554.

Schuur E.A.G., McGuire A.D., Schädel C. et al., 2015. Climate change and the permafrost carbon feedback. *Nature* **520**, 171–179. DOI: 10.1038/nature14338.

Streletskaya I.D., Shpolyanskaya N.A., Kritsuk L.N. et al., 2009. Cenozoic deposits of Western Yamal and the problem of their genesis. *Byull. Mosk. Gos. Univ., Ser. 5 (Geogr.)*, no. 3, 50–57 (in Russian).

Streletskaya I.D., Vasiliev A.A., Oblogov G.E. et al., 2018a. Methane in underground ice and frozen sediments on the coast and shelf of the Kara Sea. *Led i Sneg* **58** (1), 65–77. DOI: 10.15356/2076-6734-2018-1-65-77 (in Russian).

Streletskaya I.D., Vasiliev A.A., Oblogov G.E. et al., 2018b. Methane content in ground ice and sediments of the Kara Sea Coast. *Geosciences* **8** (12), 434. DOI: 10.3390/geosciences8120434.

Sturtevant C.S., Oechel W.C., Zona D. et al., 2012. Soil moisture control over autumn season methane flux, Arctic Coastal Plain of Alaska. *Biogeosciences* **9**, 1423–1440. DOI: 10.5194/bg-9-1423-2012.

van Huissteden J., 2020. *Thawing Permafrost: Permafrost Carbon in a Warming Arctic.* Springer Nature Switzerland AG, Cham, Switzerland, 508 pp. DOI: 10.1007/978-3-030-31379-1.

Walz J., Knoblauch C., Böhme L. et al., 2017. Regulation of soil organic matter decomposition in permafrost affected Siberian tundra soils – Impact of oxygen availability, freezing and thawing, temperature, and labile organic matter. *Soil Biol. Biochem.* **110**, 34–43. DOI: 10.1016/j.soil- bio.2017.03.001.

Whalen S., Reeburgh W., 1990. Consumption of atmospheric methane by tundra soils. *Nature* **346**, 160–162. DOI: 10.1038/346160a0.

Received December 20, 2021
Revised May 25, 2022
Accepted September 13, 2022

Translated by V.A. Krutikova

EARTH'S CRYOSPHERE
SCIENTIFIC JOURNAL

Earth's Cryosphere, 2022, vol. XXVI, No. 5, pp. 48–60

SNOW COVER AND GLACIERS

SUPERIMPOSED ICE ON THE BELLINGSHAUSEN DOME, KING GEORGE ISLAND, ANTARCTICA

B.R. Mavlyudov

Glaciology Department, Institute of Geography, Russian Academy of Sciences,
Staromonetnyj per. 29, Moscow, 119017 Russia

E-mail: bulatrm@bk.ru

Conditions of the origin, existence, and melting of the superimposed ice are considered for the Bellingshausen Ice Dome on Fildes Peninsula of King George (Waterloo) Island near Antarctic Peninsula. Every year, accumulation of superimposed ice on the ice dome reaches about 15 cm. In years with positive mass balance on the ice dome, the thickness of superimposed ice increases. The maximum measured thickness of perennial superimposed ice on the ice dome is about 145–150 cm reaching 300 cm in some places. Significance of the superimposed ice in the ice mass balance of the Bellingshausen Ice Dome in different years during the observation period from 2007 to 2021 is estimated. It is argued that regime of field observations are necessary for finding seasonal boundary of the superimposed ice as equilibrium line altitude.

Keywords: *Bellingshausen Ice Dome, Fildes Peninsula, ice mass balance, superimposed ice.*

Recommended citation: Mavlyudov B.R., 2022. Superimposed ice on the Bellingshausen Dome, King George Island, Antarctica. *Earth's Cryosphere* **26** (5), 48–60.

INTRODUCTION

The author, following [*Cuffey, Paterson, 2010; Congley et al., 2011*], considers superimposed ice (SI) to be a continuous ice layer forming in the lower part of the snow or snow–firn thickness at the boundary with the glacier ice. In Russian literature, an analogous layer of ice is called infiltration-congelation ice [*Kotlyakov, 1984*], or also superimposed ice [*Ushnurtsev et al., 1995*]. The SI thickness increases until the entire cold store in the underlying ice is used [*Cuffey, Paterson, 2010*]. In the annual snow layer on the glacier, all the formed SI melts together with the snow. In the long-term snow–firn thickness, the SI is preserved and is an element of internal feeding [*Bazhev, 1973, 1980*].

The role of SI in the life of glacier is discussed in numerous publications [*Baird, 1952; Fujita et al., 1996; Wadham, Nuttal, 2002*]. Almost all researchers believe that SI plays an important and sometimes a decisive role in glacier ice mass balance in Polar regions [*Wright et al., 2007*] and regions with continental climate [*Koreisha, 1991*]; in other regions, the role of SI is considered insignificant [*Cuffey, Paterson, 2010*].

For the glaciers of King George Island, a widespread distribution of SI is typical on the surface of ice domes after the snow melting; in particular years, SI cover vast areas. However, this phenomenon is rarely mentioned in publications on this region; the description and mention of SI on King George Island can be found in [*Gonera, Rachlewicz, 1997; Rachlewicz, 1999*]; on Signy Island (the South Orkney Islands) in [*Gardiner et al., 1998*].

In general, SI remains insufficiently studied, especially in Antarctic regions. The present work discusses SI formation on King George Island with a focus on the Fildes Peninsula and the Bellingshausen Dome located on this peninsula, where field work was conducted during 2007–2012 and 2014–2021 within the framework of seasonal studies of the Russian Atarctic Expedition. In addition to understanding the specificity of the formation and existence of SI, an attempt was made to determine its role in the ice dome mass balance.

MATERIALS AND METHODS

Study area

Field study of SI was conducted on the Fildes Peninsula (62° S) in the southwestern part of King George (Waterloo) Island in the South Shetland Islands Archipelago, near the northern end of the Antarctic Peninsula (Fig. 1).

The Fildes Peninsula is 3 km wide and 10 km long; the Bellingshausen Dome is found in its northeastern part (Fig. 2*a*). The size of the dome is 3.3 × 4.5 km, the height is 250 m asl, and its surface area is approximately 8.9 km^2. The Bellingshau-

Copyright © 2022 B.R. Mavlyudov, All rights reserved.

sen Dome continuously adjoins to other, larger ice domes of the island, which is on 95% covered by ice. More detailed information about the structure of the Bellingshausen Dome can be found in [*Mavlyudov, 2016*].

Climate

The King George (Waterloo) Island is one of the warmest regions of Antarctica. The climate of King George is maritime, with mild winters and cool summers, because of the proximity of the Southern Ocean. In summer, west to north winds dominate and bring relatively warm air masses from the Pacific Ocean; in winter, east to south winds carry cold masses from the Antarctic continent. However, during the winter, northwest bringing not only warm air but also liquid precipitation can intrude. A period with above-zero air temperatures mainly lasts from December to March. The mean annual air temperature, according to the Bellingshausen weather station [*www.aari.aq*], is –2.3°C, the mean winter temperature (April–November) is –3.9°C, and the mean summer temperature (December–March) is 0.97°C. The mean annual precipitation is 697 mm with approximately 239 mm in summer (mostly as rain) and 458 mm in winter (mostly as snow).

Research methods

The study of SI on Fildes Peninsula and on the Bellingshausen Dome was conducted simultaneously with mass balance research. Superimposed ice was studied: (1) in the base of pits excavated for measuring snow on the ice dome at the end of November – beginning of December (if SI formation had already started by that time) and during summer seasons in the period of presence of a snow cover at stakes R1, R4, R8, R12, BN, FN, and IN; (2) during the period of snow cover melting, when the SI was entirely exposed (Figs. 2*b*, *c*, *e*); and (3) during the period of SI melting, when the melting crust is formed on its surface (Fig. 2*f*). The melting crust is a highly friable 5- to 10-cm thick top layer in the glacier's ablation area, which appears as a result of direct penetration of solar radiation into the ice, which induces ice melting in the upper layer [*Kotlaykov, 1984; Mavlyudov, 2008*]. The SI thickness was measured in boreholes (Fig. 2*d*) drilled by a ring drill of 10 cm in diameter at different times along the edge of the exposed SI (Table 1). The lower boundary of annual SI in boreholes was a layer of volcanic ash particles, which at the end of the ablation season usually appear at the surface of glacial ice.

The SI thickness was also measured on the walls of fresh crevasses and near 29 ablation stakes installed across different slopes of the ice dome (Fig. 1). The density of the SI and melting crust over it were determined by weighing method.

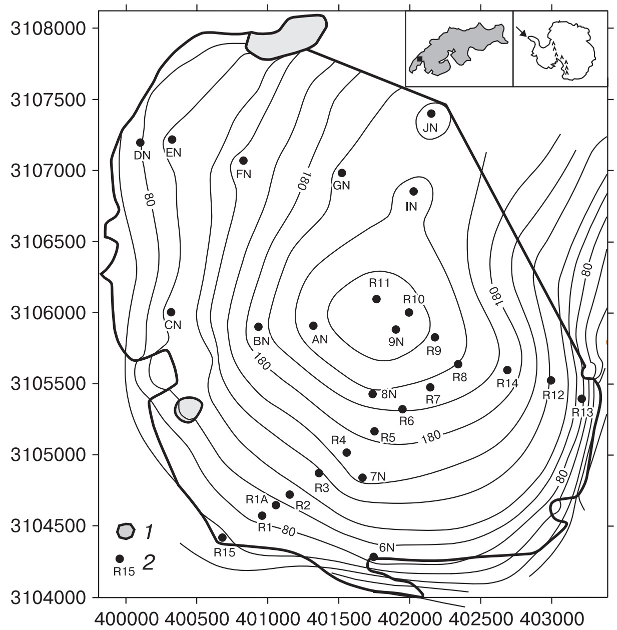

Fig. 1. Location of Bellingshausen Ice Dome and ablation stakes on it.

1 – nunataks, *2* – ablation stakes and their numbers. Inset maps show the position of King George Island (*arrow*) near Antarctic Peninsula and the Bellingshausen Ice Dome (*black square*) on King George Island (UTM coordinate system, zone 21).

RESULTS

Identified conditions of superimposed ice formation

The formation of SI depends on the structure, thickness and temperature of the snow thickness, store of cold accumulated in the underlying ice over the winter, and on the surface structure of glacial ice [*Kotlyakov, 1984*]. Study of the snow cover structure before the beginning of melting demonstrated that it consists of snow layers of varying granularity and density, as well as numerous ice interlayers. Ice layers in the snow thickness can be of two types. The first is ice crust forming upon rainfall onto a cold surface of snow. Ice crusts are usually continuous, and their thickness does not exceed 1–3 mm. Thinner ice crusts are formed upon periods of abrupt warming without liquid precipitation (radiation crusts). The second is ice interlayer forming during the concretion of water vapor onto the surface of the snow during strong winds (most often, northern and northwestern) under conditions of high air humidity (fog) and near-freezing temperature. In this case, single ice aggregates of about 2 cm wide, 2–4 cm long and approximately 1 cm thick grow on the surface of the snow cover. These aggregates are inclined at 10°–20° to the surface of the snow and are oriented against air flows. In such layers, ice aggregates are not interconnected.

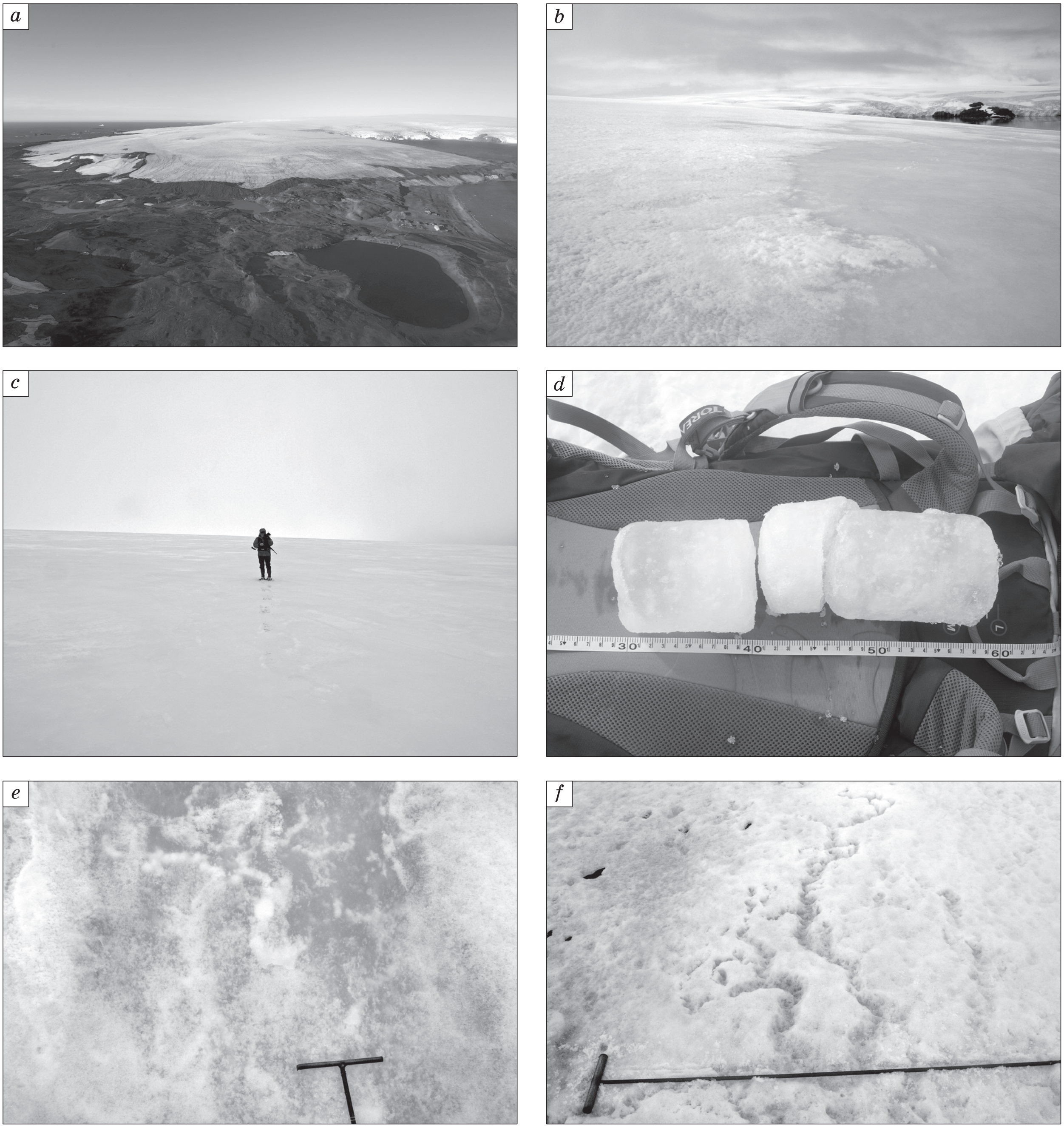

Fig. 2. Bellingshausen Ice Dome: (*a*) view from the southeast from a helicopter (March 7, 2020), (*b*) boundary between snow and exposed SI on southern slope of the dome, (*c*) SI field on southern slope of the dome (December 31, 2019), (*d*) core of the long-term SI, (*e*) surface of the exposed SI with translucent inner channels, and (*f*) melting crust with melted out inner channels on the surface of exposed SI.

The overall thickness of the layers with ice aggregates usually does not exceed 2–3 cm.

At the beginning of the warm season, meltwater seeps through snow to ice interlayers, beginning to increase the thickness of ice crust and bind together ice aggregates. However, the heat released during the freezing of meltwater on ice interlayers most often does not allow a significant increase in their thickness. As a result, water finds a way through the ice crust or between ice aggregates and infiltrates into deeper layers. However, in some cases, meltwater makes ice interlayers impermeable. In this case, ice begins to grow over these ice interlayers and isolates layers and lenses of snow or firn within the ice thickness.

Table 1. **Characteristics of superimposed ice on the Bellingshausen Ice Dome in different years**

Year	Average SI thickness for the dome, cm	Range of SI thickness variation, cm	Average SI thickness according to stake measurements, cm w.e.	SI melting, cm w.e.	SI share in B_w according to stake measurements, %	SI share in B_s according to stake measurements, %
2007/08	19.9 (214)	1–28	18.1	8.8	28.3	12.0
2008/09	16.0 (107)	7–43	14.3	9.3	26.9	7.4
2009/10	15.6 (76)	4–27	14.4	0.7	18.3	1.6
2010/11	38.9 (53)	4–52	13.4	8.7	21.4	17.2
2011/12	30.3 (20)	10–69	16.1	14.4	28.5	12.6
2012/13				0		0
2013/14				0		0
2014/15	41.7 (29)	5–54	12.4	0.9	23.0	1.6
2015/16	25.7 (60)	8–56	16.4	3.1	27.8	5.5
2016/17	30.7 (36)	6–175	14.9	16.5	28.1	17.6
2017/18	14.6 (34)	5–150	14.4	19.0	24.4	19.5
2018/19	13.6 (40)	5–35	12.9	4.7	20.7	9.1
2019/20	67.1 (64)	3–300	11.8	31.6	23.0	18.1
2020/21	13.8 (122)	5–106	10.9	10.9	13.4	10.9

Note: Number of measurements is indicated in parentheses. B_w is the winter mass balance, and B_s is the summer mass balance. Bold face in the first column indicates years with positive mass balance.

A portion of ice in the snow thickness on the ice dome differed significantly from year to year and from point to point because it depended on the thickness and structure of the snow, slope orientation, and weather conditions during previous periods. During all years of observation, at the end of the season of accumulation, at maximum snow accumulation, the amount of ice (by water content) within the seasonal snow thickness ranged from 12 to 60% given the average snow thickness of 0.4–0.5 g/cm^3. During the season of ablation, the overall amount of ice in the seasonal snow initially increased and then decreased.

Measured snow temperatures at the bottom part of the snow thickness at the end of the season of accumulation on the Bellingshausen Dome in different years varied from –3 to –5°C. Low snow temperature contributed to freezing of meltwater seeping from the surface of the snow and moistening the snow thickness with the growth snow grains as well as to the increase in the thickness of ice interlayers. The SI formation in the lower part of the snow–firn thickness took place primarily during its moistening by meltwater. In some cases, this process could begin earlier, if meltwater flowed or seeped through down the slope under the snow thickness from higher positions with a thinner snow, where it melted first, how it happened, for example, on the slope below stake R4.

Measurements in pits showed that the average mineralization of seasonal snow in the upper part of the ice dome was approximately 70 mg/L. During water flowing down the ice slope, its partial freezing (during SI formation) took place, which led to increasing concentration of salts in the water flowing over the ice. At the beginning of the ablation season, water mineralization reaching 1000 mg/L) was measured several times in the pits in the lower part of the snow thickness. This indicates that the water made quite a long way under the snow. The recorded mineralization of the SI itself was 20–30 mg/L. The measured velocity of water flow under the 1-m-thick snow cover on a slope of about 10° reached approximately 80 m/day. If the rate of water flow down the dome's slopes is considered as a constant, meltwater can flow down from the top of the dome to its lower part in 18–19 days. This rate increases as the steepness of the slope increases and the snow thickness decreases. The latter leads to the growth of the thickness of the moistened layer in the lower part of the snow thickness which achieves a maximum in a strip of water-saturated snow ("snow bog") at the boundary of the snow cover and the exposed SI. Upon the emergence of a thick layer of wet snow, the formation of SI slows down and then ceases. According to the author's estimates, the duration of SI growth on the dome during the spring is 1–1.5 months and depends on the air temperature and the activity of spring snowmelt. At the same time, the growth of the SI layer occurs on the whole snow-covered surface of the ice dome. Apparently, an exception is the areas of the ice dome, where the long-term snow–firn thickness is maximal, i.e., where it exceeds 3 m, so that SI forms within this thickness and meltwater runoff during the ablation season is minimal.

It was determined that snow disappears first in the areas with the minimum snow thickness in the middle of the southern (near stake R4) and northwestern (near stakes EN and FN) slopes and at the lower part of the dome (if there is no windblown snow pack there). An area of melted snow appeared in the snow field and began to grow in all directions increasing the area of the exposed SI layer. The exposed SI begins to melt, and a layer of melting crust – a loose mass of weakly cemented ice grains of 1–2 mm in diameter – forms on it. After the SI melting, glacier ice is exposed to the surface, and the area of SI encircles exposed glacier ice. Subsequently, the area of exposed glacier ice also begins to increase. Meltwater channels form in the exposed field of glacier ice and are drained down the slope, first into the strip of SI, then also into the area of snow. In the case of active melting and considerable meltwater discharge through these channels, slush flows can form in the snow field. Getting toward the lower side of glacier ice, meltwater can sometimes penetrate under the edge of the partially melted SI and further flow beneath the SI at some distance. However, as the SI layer is frozen to the glacier ice at the contact with the snow field, meltwater flow under it becomes impossible. As a result, weakened areas of the SI layer appear in this zone, where meltwater discharge to the surface takes place in the form of small fountains giving the birth to surface water streams. Often, on the exposed surface of the SI layer on the dome, currently active and former fountains can be identified by the presence of dark spots of volcanic ash carried out by the meltwater streams onto the surface of the whitish SI. Volcanic ash is present in the form of interlayers within the glacier ice and is mainly derived from volcanic eruptions on Deception Island of the same archipelago 120 km to the west-southwest [*Jiankang et al., 1999*].

If the long-term snow–firn layer exceeds 2 m, as recorded near stakes R6–R9, then SI can also form on the surface of one of the ice interlayers near the bottom of the snow thickness at the end of the ablation season. Most often, this was observed at a distance of 0.5–0.8 m from the surface of the glacier ice, so that firn layer sealed from the top by SI was preserved. In 2016, the author measured the thickness of one of such suspended SI layers in the pit near stake R6; it equaled 25 cm and was formed over the course of 1.5 years. Subsequently, while the snow cover was preserved, the thickness of this SI layer increased. In this case, a new SI layer formed within the firn thickness, under which the layer of sealed firn was preserved. At the end of the 2018/19 summer season, the thickness of the suspended SI layer reached 70 cm. An analogous phenomenon was also noted at other measurement stakes in the upper part of the ice dome with a sharp decrease in the snow–firn thickness measured weekly using a metal probe during the ablation season.

In autumn, SI formation is favored by the conditions in the thin lower part of the snow cover. A new SI layer is formed, the thickness of which decreases in the direction of increasing snow thickness. A layer of autumn SI can be preserved until the next ablation season or melt together with the snow during the next summer warming.

At the end of the ablation season, the surface of the glacier ice becomes uneven, very dissected, cut by numerous channels deepened into the ice and forming along former ice cracks and other defects. Numerous recesses and rises of 10–15 cm in amplitude are typical for the ice surface during this time, as well as cryoconite holes of different sizes. The formation of SI in the autumn and, to a larger extent, in the spring leads to leveling of the ice surface. Consequently, during simultaneous snow melting in separate areas of the ice dome, large areas of leveled SI surfaces were observed. Specifically, such leveled surfaces are favorable for the formation of areal slush flows from a water-saturated snow strip at the boundary with the snow cover upslope. In many cases, this led to an accelerated disappearance of the snow cover on separate areas of the dome, especially on north-facing slopes.

Characteristics of SI on the ice dome

According to the author's measurements, the average thickness of the annual SI layer on the ice dome is 15–16 cm. Depending on the relief of the surface and the presence of crevasses, the thickness of the layer varied from 2 to 24 cm or more. The minimum thickness of SI (about 2 cm) was recorded at the lower side of perpendicular long-term crevasses in the western part of the ice dome. This indicates that the freezing of water entering from upslope areas played an important role in the formation of superimposed ice.

If, during the summer, snow in the upper part of the ice dome does not melt fully, as it happened in 2009–2016, as well as partially in 2017–2019, then SI, which accumulated at the beginning of the ablation season, does not melt under the snow cover. At the beginning of the next ablation season, a new SI layer begins to grow on the SI layer from the previous year. Thus, the thickness of the SI layer is summated. Given an average thickness of annually accumulating SI layer of approximately 15 cm, a maximum thickness of approximately 75 cm accumulated during five years was first observed on the ice dome. Then, the maximum thickness of SI was found to be equal to 145 cm near stake R12 on the eastern slope of the dome in March 2019. In some areas along the periphery of the ice dome, the SI thickness reached 1.5 m, which is indicative of about a decade of its continuous accumulation. The SI thickness of 3 m was recorded near stake R7 in ice crevasse under snow and firn.

Data on the average thickness of the SI layer on the Bellingshausen Ice Dome in different years are provided in Table 1. They indicate that only in 2007–

2009, 2017–2018, and 2020 the average SI layer showed annual growth of up to 16 cm. In other years, the average SI thickness was higher because of the SI accumulation over several years.

To compare, Table 2 shows data on SI for different regions. It can be seen that the predominant SI thickness accumulated during one summer season in different regions is in the interval of 10–20 cm and increases up to 27–35 cm only high in the mountains on the Aktru Glacier, at the boundary of the firn–ice and cold firn zones in conditions of continental climate of the Altai Mountains. On glaciers of the Suntar-Khayata Ridge, in conditions of cold climate, similar thicknesses of seasonal SI were recorded in the ablation zone. Larger SI thickness values obtained for the Kongsvegen Glacier (Spitsbergen) were possibly related to damming of meltwater in the snow cover within separate parts of the glacier.

The density of SI on the ice dome slopes was measured in 10- to 40-cm-long ice cores and reached 0.66–0.91 g/cm^3. Such a wide range of SI densities is apparently connected to the structure of wet snow, the presence or absence of ice interlayers and their thickness, as well as to the number of air bubbles in the ice. Average data from 97 samples showed SI density equal to 0.82 g/cm^3. The obtained average SI density on the Bellingshausen Ice Dome agrees well with data from other glaciers (Table 2): 0.8 g/cm^3 for Kongsvegen Glacier on Spitsbergen [*Brandt et al., 2008*], 0.87 g/cm^3 for Xiao Dongkemadi Glacier on the Tibetan Plateau [*Fujita et al., 1996*], 0.89 g/cm^3 for McCall Glacier in Alaska [*Wakahama et al., 1976*], and 0.85–0.91 g/cm^3 [*Bazhev, 1980*] and 0.86–0.98 g/cm^3 [*Shumskii, 1955*] for various glaciers.

A layer of melting crust appears on the surface of melting SI, which, despite having a firn-like snow structure, differs sharply from it. The snow on the surface of the dome is partly covered by dust because dust concentrates on the surface during melting and subsidence of snow. Areal meltwater flows running from a strip of water-saturated snow wash away all dust from the surface of the exposed SI leaving it absolutely clean. Because of this, the surface of the melting SI (melting crust) has a comparable or even a higher albedo than melting snow and a much higher albedo than that of the strip of water-saturated snow and SI just exposed from snow. The following albedo values were obtained through measurements: melting SI, 0.8–0.9 (the average of 13 measurements is 0.85); melting snow, 0.79–0.89 (the average of 8 measurements is 0.85); water-saturated snow, 0.704–0.723 (the average of 4 measurements is 0.716); exposed and not yet melting SI, 0.62–0.64 (the average of 3 measurements is 0.63). The obtained albedo values are close to data for other glaciers [*Cuffey, Paterson, 2010*].

The melting crust surface of the SI is friable and firn-like; it consists of single firn grains of 1–2 mm and more in diameter. The density of the melting SI (to be more exact, the melting crust on SI) varied from 0.6 to 0.9 g/cm^3 (the average of 46 measurements is 0.767 g/cm^3), i.e., it slightly exceeded the

Table 2. **Data on superimposed ice in different regions**

Region	Glacier	SI thickness, cm/yr	Share of SI in mass balance, %	SI density, g/cm^3	Ice formation zone	Source
Spitsbergen	Kongsvegen	(16 ± 6) to 43	15–33 B_w	0.80	fs	[*Brandt et al., 2008*]
Spitsbergen	Kongsvegen	15–(60 ± 10)	35–100		fs	[*Obleitner, Lehning, 2004*]
Spitsbergen	Central Loven	11–18	10–30 B_w		fs	[*Wadham, Nuttal, 2002*]
Spitsbergen	Central Lovem	15	16–25–37		fs	[*Wright et al., 2005*]
Spitsbergen	Store	27	up to 100		fs	[*Jonsson, Hansson, 1990*]
Spitsbergen	Austfonna		5–100 B_w		fs	[*Dunse, 2011*]
Spitsbergen	Aldegonda	15–20			a	[*Solovyanova, Mavlyudov, 2006*]
Spitsbergen	Eastern Grønfjord	12			a	[*Chernov et al., 2015*]
Severnaya Zemlya	Mushketova	17			fs	[*Bolshiyanov et al., 2016*]
Alaska	McCall	20–30–40	50	0.89	fs	[*Wakahama et al., 1976*]
Alaska	McCall		>40 B_w		fs	[*Rabus, Echelmeyer, 1998*]
Baffin Land, Canada	Beims	16.5			fs	[*Baird, 1952*]
Altai	Aktry	20–35			fs–cf	[*Narozhnyi, 2001*]
Suntar-Khayata	No. 30–34	17.5 (5–30)			a	[*Mavlyudov, Ananicheva, 2016*]
Tibet Plateau	Ksnao Dongkemadi		26–60	0.87	fs	[*Fujita et al., 1996*]
Various regions			up to 80–100	0.85–0.91	fs–cf	[*Bazhev, 1980*]
King George Island	Ekologic	10–15			fs	[*Gonera, Rachlewicz, 1997*]
King George Island	Ekologic	7	up to 20		fs	[*Rachlewicz, 1999*]
Different Regions				0.86–0.89	fs–cf	[*Shumskii, 1955*]

Note: B_w is winter mass balance; ice formation zones: cf – cold firn zone, fs – firn–snow zone, and a – ablation zone.

density of the firn and was slightly less than the density of the SI not subjected to melting. The significant difference in density values of the melting crust on SI depended on the presence and thickness of ice interlayers existing in the snow and firn before the formation of SI.

Specific features of SI melting

The melting of SI begins under a thin layer of snow under the influence of solar radiation. Small inner channels forming a sparse dendritic network of voids are developed in the SI thickness at shallow depths. The density of these channels can reach 5 m per 1 m^2 and more. How exactly are they formed in the SI thickness is not quite clear. It is possible that they develop from air bubbles, which are abundant in the SI. Under the thick layer of snow, channels are not formed; melting inside the ice begins under the influence of solar radiation, when the thickness of the snow becomes less than 0.5–0.6 m. The melting of inner channels that appear in the SI thickness creates unevenness on its surface in the form of shallow dry channels (Fig. 2*f*).

At the first exposure from under the snow, the water permeability of the SI layer is low, and the borehole drilled in it remains completely filled by water. But as soon as the area of the exposed SI widens and a melting crust is formed in its central part, no water remains in the boreholes near the upper boundary of the exposed area of SI, because water is drained through the melting crust. On the contrary, in the boreholes drilled along the lower boundary of the exposed SI area (below the field of exposed glacier ice), the water level stands at the top of the boreholes, because of the absence of drainage channels in the SI thickness.

The layer of SI under the snow cover preserved after the summer season and the adjacent part of exposed SI contribute to the increase in the thickness of the glacier ice. In 2007/08 and 2008/09, the SI melted almost entirely on the Bellingshausen Ice Dome; in 2009/10, it was preserved in some locations the southern and northwestern parts of the dome above 170 m asl. At higher elevations, SI was preserved everywhere. In 2010/11 and 2011/12, it was preserved at elevations above 180 m asl (on average). In 2012/13–2014/15, the SI layer on the dome did not melt out under the preserved snow. Active melting of the SI continued in 2016/17 and 2017/18 because of high summer air temperatures; in 2018/19 the SI melting was reduced because of frequent summertime snowfalls. In summers of 2019/20 and 2020/21, melting of the SI was active (Table 1). According to our estimates, except for cold seasons of 2009/10, 2012/13–2015/16, and 2018/19, when snow was preserved almost on the entire surface of the dome until the end of the ablation season, the melting of the SI reached approximately 9 cm in water equivalent (w.e.) and more. In summers of 2011/12, 2016/17, 2017/18, 2019/20, and 2020/21, the SI layer, which had accumulated over previous years, melted away completely. A comparison of average melting rates of the SI on the dome with the mean summer temperatures recorded at the Bellingshausen weather station (Fig. 3) demonstrated their relatively close relationship with the coefficient of determination $R^2 = 0.66$.

Duration of the SI formation at different elevations of the ice dome

The formation of SI on the ice dome most often did not exceed one month. During years with positive mass balance, the growth of SI in the lower part of the dome began in December and ended in January, and sometimes could last throughout the entire summer with varying intensity, as it happened in 2014/15. During years with negative mass balance, the growth of the SI in the lower part of the dome began in November and ended in December. In individual years, certain shifts in the dates of SI growth in dependence

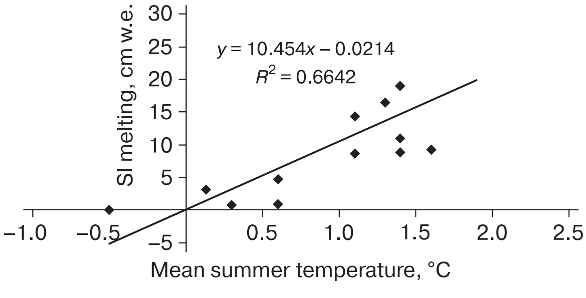

Fig. 3. Averaged melting rate (stake measurements) versus mean air summer temperatures at Bellingshausen weather station in 2007–2021.

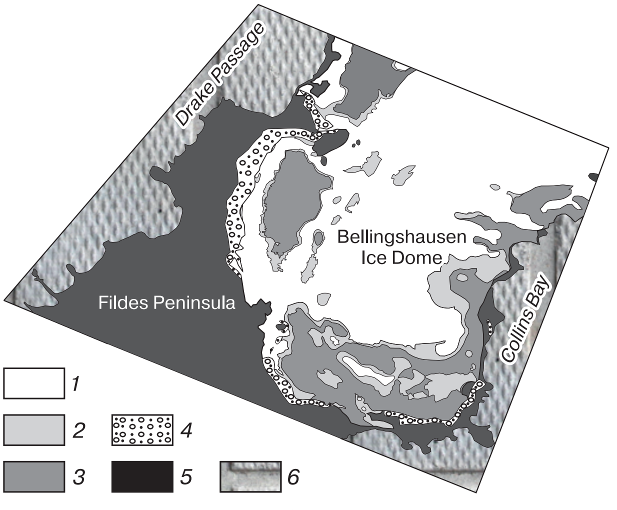

Fig. 4. Distribution of different types of snow–ice formations on the Bellingshausen Ice Dome.

1 – snow, *2* – superimposed ice, *3* – glacier ice, *4* – moraine, *5* – ice-free area, *6* – sea. Composed on the basis of TerraSAR-X radar image from March 12, 2011 (the end of ablation period).

on the height of the dome were recorded. On the top of the dome, the growth of SI during active snow melting, could begin simultaneously with its growth at the lower part of the dome (2014/15 and 2016/17) or 1.5–2.5 weeks later. The end of the SI formation on the top of the dome could take place in 0.5–1.5 months after the end of this process at the lower part of the dome. The duration of the SI formation shortened considerably in summers with positive air temperatures, abundant and frequent rainfalls, and periods with thick fogs. The duration of the SI formation increased in summers with cold weather, solid (snow) precipitation, and blizzards alternating with periods of warm weather.

Distribution of superimposed ice

The greatest extent of SI on the dome was noted in periods with rapid exposure of the SI surface out of the snow cover. Then, the area of the SI distribution decreased (Fig. 4).

The area of SI distribution increased in the years with warm weather after a series of years with a positive mass balance (2016/17, 2017/18, 2019/20). In such cases, the strip of the simultaneously exposed SI was more than 300 m wide because of the melting of SI of considerable thickness accumulated during several years. The largest recorded width of the SI strip (900 m, more than half of the slope of the ice dome) was recorded on March 21, 2012 on the southeastern slope of the ice dome and on December 31, 2019 on the southern slope of the dome.

DISCUSSION

This study, as well as previous research [*Wadham, Nuttal, 2002*], demonstrates that the formation of SI can occur in one step (during the spring) or in two steps (in the autumn at the end of melting on the dome and in the spring). A greater part of the SI thickness forms during the spring stage. In the spring, SI formation occurs everywhere, whereas in autumn it only takes place within the fields of snow, in the course of freezing of snowmelt during autumn (in some cases, also summer) cooling. Below on slope of the snow fields, the freezing of meltwater flowing from them leads to the formation of a congelation ice layer above the glacier ice [*Koreisha, 1991*]. The thickness of the autumn SI depends on the water saturation of the snow higher up the slope and on the degree of cooling at the end of the ablation season. More favorable conditions for the formation of SI are created if rainy weather is abruptly changed by cooling in autumn. In that case, rainwater seeping through the snow joins snowmelt runoff.

In the ablation zone, SI can be seasonal, but it can easily survive for two years (pereletok) or more, if the snow cover on some area or on the entire surface of the ice dome does not melt during the summer season. At negative mass balance on the ice dome, the SI is exposed on the surface as a strip of varying width at the boundary between the glacier ice and snow (Fig. 2*b*, *c*). At even melting of a consistently thick snow cover, vast surfaces of the ice dome can become simultaneously covered by SI. This usually lasts a short time (depending on the weather, from one week and more). After a long period with a positive mass balance, at a large thickness of accumulated SI (75 cm and more), its melting on the surface of the glacier can take a long time. During the summer of 2016/17, melting of the SI in the lower part of the ice dome lasted over 46 days; in the upper part of the dome, it affected only the topmost part of the SI thickness, while its main part remained unchanged. In March 2019, the SI near stake R11 was more than 125 cm in thickness.

As SI characterizes accumulation and its lower boundary corresponds to the equilibrium line of the glacier, the melting of the long-term SI on the slopes of the ice dome complicates the determination of the equilibrium line for the particular year, because it is virtually impossible to separate between annual ice layers within continuous SI thickness. It is possible to determine the equilibrium line elevation only in individual places near measuring stakes and between them. The accumulation of SI over several years can become a reason for the lack of possibility to reliably determine the equilibrium line altitude of the Bellingshausen Ice Dome upon complete melting of the snow cover and exposure of the SI. This is true for all kinds of terrain research and remote sensing, if stake measurements are not conducted. Stake observations are a must on the glaciers and ice domes of the studied Antarctic region, because even studies of SI in pits and boreholes do not allow for accurate identification of the year to which a specific part of the SI layer belongs.

Two types of glacier feeding exist on the ice dome: (a) transformation of nonmelted snow into firn in the firn–ice zone and (b) accumulation of SI at the base part of the snow cover in the infiltration–congelation zone. In the latter case, direct transformation of snow into ice occurs during refreezing of meltwater. In the first case, the formation of glacier ice occurs in several steps. First, snow which has not melted during the summer, transforms into firn containing numerous ice grains, lenses and interlayers, as well as a layer of SI at the snow base. Subsequently, by to inner feeding, the amount of ice in the firn thickness increases, and the growth of SI in the lower part of the firn layer continues. In many cases, it was recorded (near stakes R6, R14, 9N, and IN) that the SI appears within the firn layer and isolates the underlying firn from meltwater. As a result, layers and lenses of firn are preserved inside the ice thickness. It is possible that future radar research of the snow–firn layer in the upper part of the ice dome will indicate how widespread is this phenomenon and what is the thickness of the suspended SI layer (or layers) in the firn–ice body. In particular, studies of ice cores from the top of the dome in 1992 demonstrated the presence of firn interlayers down to a depth of 7 m below the surface [*Wen et al., 1998*].

Regardless of the sign of mass balance of ice on the dome in general, in recent years, there always have been areas, where SI melted away entirely, and areas, where it continued to accumulate. In years with a positive mass balance, the accumulation of SI took place over a larger part of the dome, and in years with a negative mass balance, it took place only in the areas with preserved snow–firn thickness. During warmer periods, the role of the SI layer as a sink of moisture decreases, whereas during cooling it increases. Currently, the accumulation of SI is the only process of ice formation on the ice dome, because even in the upper part of the dome, the thickness of the accumulating snow and firn is clearly insufficient for their transformation into ice under their own weight.

The process of ice formation on the dome through growth of the SI thickness is typical not only for the present time. In some parts of the glacier (for example, near stakes R5 and FN), after melting of the snow cover and SI, glacier ice with ice crystals of 2–3 mm becomes exposed and quickly transforms into the snowlike mass of melting crust under the impact of solar radiation. This glacier ice was formed from the SI in the past. It differs from the modern SI by the presence of numerous crevasses filled by macrocrystalline ice (which formed during the freezing of water in crevasses) and cryoconite holes of varying sizes, which emerged upon melting of the ice enriched in volcanic ash particles. Such structures do not exist on the surface of modern SI.

If we take the average thickness of SI accumulating on the Bellingshausen Ice Dome over a year equal to 15 cm (or 12.2 cm w.e.) and assume that SI forms under the snow and firn of any thickness, it becomes possible to estimate the portion of SI in the water content of the snow of varying thickness (Fig. 5).

The portion of the SI layer in the winter mass balance on the ice dome depends on the snow thickness and decreases exponentially with an increase in the snow thickness. However, the curve in Fig. 5 is merely theoretical, because at a small snow thickness, such an SI layer is unlikely to form because of warming of the snow thickness by solar radiation. This means that at a small snow thickness, the SI layer should also have a smaller thickness, but its portion in the winter mass balance will be preserved. At an average thickness of annually accumulating snow of about 1.0–1.5 m, the SI layer portion in the winter mass balance can be estimated at 20–30%, which is confirmed by measurements at stakes (Table 1). If average values of snow and ice melting and the thickness of melted away SI measured at stakes on the dome are taken into account, then the portion of melting SI in the summer mass balance on the dome can be estimated. This melted part of the SI does not exceed 20% of the total mass balance; it increases in

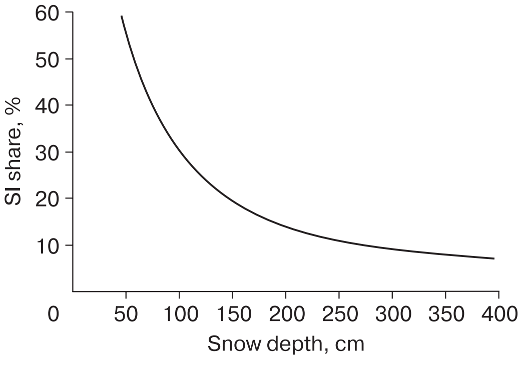

Fig. 5. Dependence of the water content of SI on the snow cover depth.

Annual water equivalent of SI 12.2 cm w.e., snow density 0.5 g/cm^3.

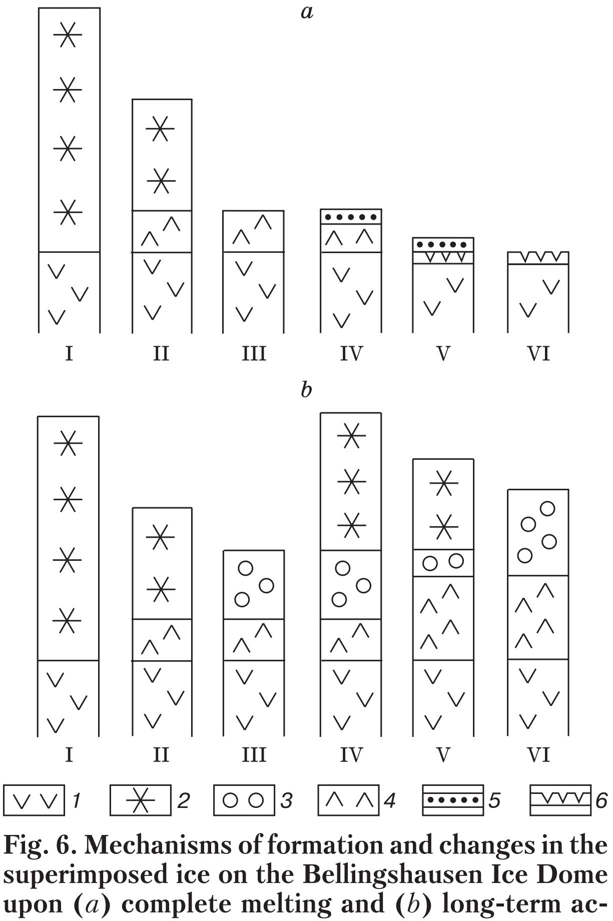

Fig. 6. Mechanisms of formation and changes in the superimposed ice on the Bellingshausen Ice Dome upon (*a*) complete melting and (*b*) long-term accumulation.

1 – glacier ice, *2* – snow, *3* – firn, *4* – SI, *5* – melting crust at the SI surface, *6* – melting crust at the glacier ice surface; (I–VI) sequence of changes.

years with a negative mass balance and decreases in years with a positive mass balance.

Two mechanisms of SI formation and change can be observed on the Bellingshausen Ice Dome: (1) the accumulation of SI at the base of the snow and firn layer and its complete melting after the disappearance of the snow–firn thickness during the ablation season; and (2) the accumulation of SI at the base of the snow and firn layer, its preservation under a layer of nonmelted snow and firn, and the continuing accumulation of a new SI layer over the SI layer of the previous year (Fig. 6). The first mechanism domi-

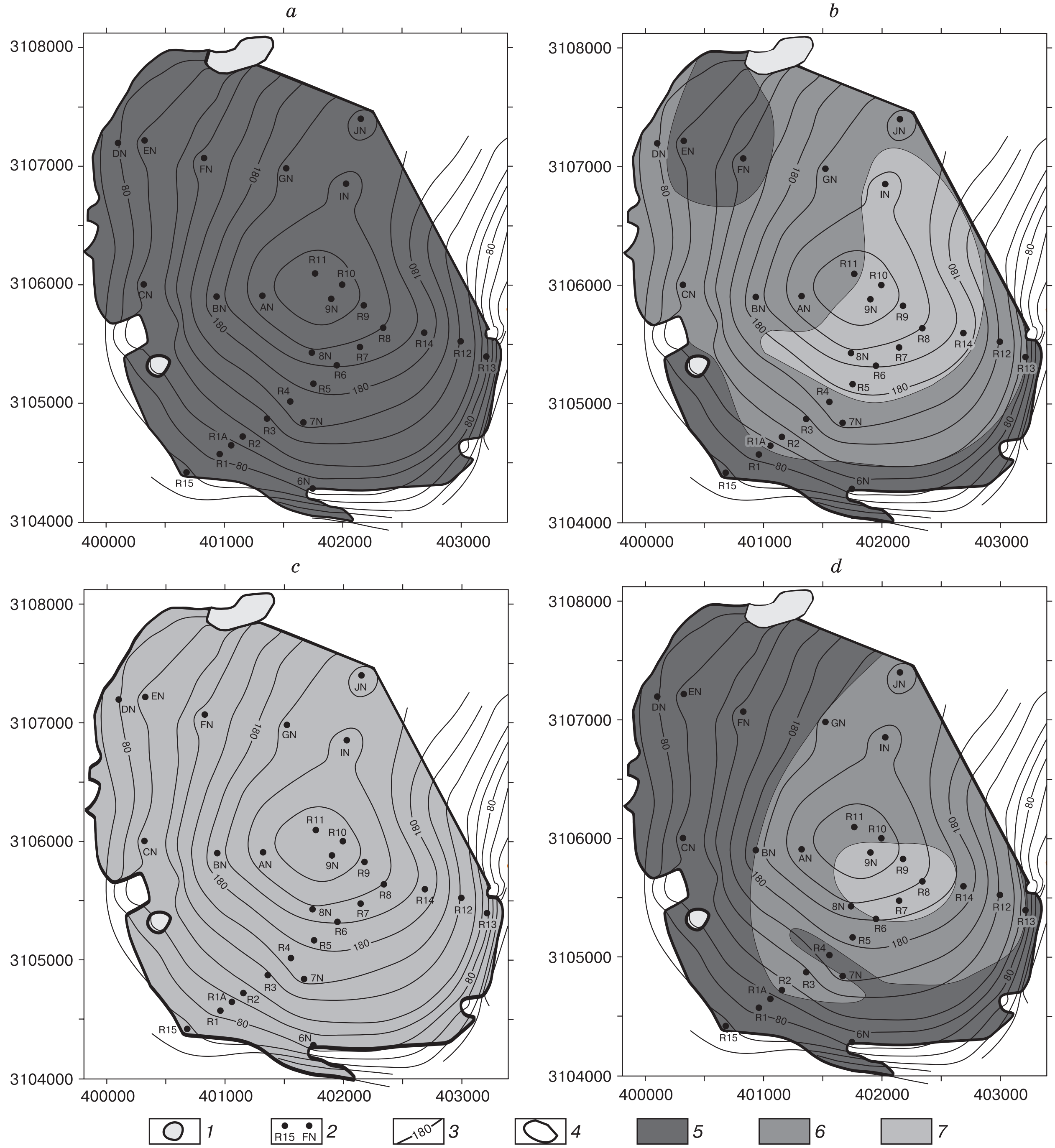
a
b
c
d
3108000
3107000
3106000
3105000
3104000
400000
401000
402000
403000
DN
EN
FN
GN
JN
IN
CN
BN
AN
R11
R10
9N
R9
R8
R14
R12
R13
8N
R7
R6
R5
R4
R3
7N
R1A
R2
R1
R15
6N
80
180
1
R15 FN
2
180
3
4
5
6
7

Fig. 7. Distribution of SI fields on the Bellingshausen Ice Dome in different periods: (*a*) 2007–2009, (*b*) 2009–2012, (*c*) 2012–2016, and (*d*) 2016–2021.

1 – nunataks, *2* – stakes and their numbers, *3* – contour lines on the dome surface, *4* – boundaries of the Bellingshausen Ice Dome; *5*–*7*, zones of SI accumulation (*5* – seasonal, *6* – melting, *7* – long-term).

nates in the periphery of the ice dome, and the second mechanism is observed in the upper part of the dome (Fig. 4).

At the dome surface area of 8.9 km^2 and the average thickness of SI of 15 cm (12.2 cm w.e.), the total volume of SI on the dome at the beginning of the summer can be estimated at $1.34 \cdot 10^6$ m^3, or $1.09 \cdot 10^6$ t. This is approximately equal to the annual increase in the amount of glacier ice (without snow and firn) in water equivalents in years with a positive ice mass balance. During the summer, the amount of SI accumulated in a particular year decreases. The higher the summer air temperature, the lesser the amount of SI preserved toward the end of the ablation season and vice versa. In recent years, during periods with a negative mass balance, approximately 400,000 t of SI have been preserved on the dome annually.

Three zones can be identified on the Bellingshausen Ice Dome: the zone of seasonal SI accumulation (the average thickness is 15 cm, regardless of the time of measurements), the zone of melting SI, and the zone of accumulating SI (Fig. 7).

In the first years of this study, the accumulation of only seasonal SI took place on the ice dome (Fig. 7*a*). After 2009, an area of continuous accumulation of SI with a total thickness of up to 45 cm appeared on the southeastern side of the dome; it was bordered by the transitional area of melting SI of 0–45 cm in thickness (Fig. 7*b*). In 2012–2016, a continuous growth of the SI thickness took place on the whole area of the ice dome, up to 60 cm on the periphery and up to 100 cm near the dome's top (Fig. 7*c*). In 2016–2021, a complete melting of SI took place along the periphery of the dome, where the SI thickness reached 150 cm. In the area of ablation stake R7, in a crevasse, the SI thickness measured in the summer of 2020/21 was up to 300 cm (Fig. 7*d*). Thus, the distribution and thickness of the SI on the dome changed in time and in space. The further accumulation of SI and its distribution within the dome will depend on climate changes.

CONCLUSIONS

Superimposed ice plays the same role in the ice dome's mass balance as nonmelted snow: about 20–30% of the winter balance and up to 20% of the summer balance.

The functioning of SI can be summarized as follows:

(1) Superimposed ice levels the surface of glaciers, which is favorable for the development of flush flows that accelerate the removal of snow from the surface of glaciers. Because of the leveling of the glacier surface by SI, water flows may change the position of their channels in space. Sometimes, meandering former channels of water streams can be seen on the exposed glacier surface. Such channels remain filled with SI for a long time.

(2) Superimposed ice contributes to the transformation of the outer layer of glacier ice under it. The ice of the Bellingshausen Ice Dome is greatly contaminated by volcanic ash particles derived from eruptions of the Deception Volcano. As a result of partial melting and decreasing thickness of SI, the underlying glacier ice becomes subjected to the action of direct solar radiation. First of all, dark ash particles are heated and favor ice melting. Therefore, the surface of glacier ice under SI is often dissected by vertical microchannels containing ash particles on the bottom. Thus, a specific melting crust is formed in the glacier ice; the latter becomes less dense (0.3 g/cm^3 and less) and acquires openwork structure because of the presence of a large number of voids. Similar phenomenon was described by the author for Spitsbergen glaciers [*Mavlyudov, 2008*]. Rapid melting of such ice after the disappearance of SI contributes to the leveling of the surface of glacier ice.

(3) Superimposed ice accelerates the transformation of snow and firn into ice without considerable growth in their thickness.

(4) The forming SI suspends snow melting; despite settling of the snow surface, the water content of the snow remains relatively stable in the period of SI formation. If this SI becomes exposed to the surface, its melting requires more energy than the melting of snow, which was indicated in [*Koreisha, 1991*].

(5) In contrast to many other areas, the strip of exposed SI on the Bellingshausen Ice Dome has a significant width (tens and hundreds of meters) at the end of the ablation season, which is related to the simultaneous melting of snow and firn over large areas and to the long-term accumulation of SI.

(6) Regardless of the density of SI on the Bellingshausen Ice Dome, the melting crust on its surface represents a firn-like friable mass of rounded ice grains of 1–3 mm in diameter, which can serve as evidence of the mainly infiltration origin of the SI. The role of congelation in the SI formation is less significant.

The formation of SI on glaciers plays an important role in slowing the response of the glacier mass balance to climate change [*Wang et al., 2015*]. With climate warming, which is observed in many regions, the amount of forming and preserved SI should decrease; SI is unlikely to influence the mass balance of glaciers more in the future than it currently does. It is probable that the role of SI in glacier mass balance should decrease with further warming. However, it may also increase upon climate cooling, when the ice temperature under the snow becomes lower, whereas summer melting of the accumulated snow does not change much. This is possible upon winter cooling and preservation of summer temperatures. At the same time, as SI is a transformed part of the snow cover, the change in its share in the snow cover upon climate changes should be reflected in the glacier mass balance value. An additional possibility of slower snow melting in the areas of SI accumulation can be related to the formation of SI not only from local meltwater but also from dammed meltwater flowing down the slope from upslope positions. The redistribution of meltwater on slopes can lead to some increase in the SI thickness and retard snow melting. The particular patterns of meltwater flows depend on the local features of the relief of the glacier rather than on climate changes.

It is believed that SI formation decreases runoff from glaciers as compared with that under conditions without refreezing [*Wang et al., 2015*]. Indeed, in polar and alpine regions, SI thickness increases, while its decrease in observed in the middle latitudes. This means that the amount of water stored in SI decreases as we move away from polar and alpine regions. At the same time, no significant amounts of SI are formed on warm glaciers, where the role of SI in the regulation of water discharge from the glaciers is relatively small.

Annually accumulating SI layer (of any thickness) preserved on the dome at the end of summer is indicative of a positive ice mass balance, while the complete melting of SI layer attests to negative mass balance at each particular point of the glacier.

Previous researchers do not note the exposure of SI to the surface of the Bellingshausen Ice Dome. Nonetheless, there is no doubt that SI formed and was exposed to the surface in the past, as well as at present. In 1968–1970, the equilibrium line altitude of the ice dome was at 120–145 m asl [*Zamoruev, 1972*], so the strip of SI exposed after melting of snow and firn could exist along this line. Undoubtedly, in the upper part of the dome, where a warm firn zone was found, SI, together with the innerfeeding partially or completely blocked water discharge from the upper zone.

Thus, the origin, current state, and dynamics of SI on the Bellingshausen Ice Dome are considered in this article. It is demonstrated that the SI layer in the lower part of the snow cover is distributed everywhere throughout the dome; in some parts of the dome, it has a seasonal character and melts away by the end of summer. The SI layer is preserved under the snow cover and merges together with the SI formed in the previous year(s). At the average annual accumulation of SI of about 15 cm, the presence of areas, where the SI layer has a thickness of 145–150 cm and even 300 cm in some places, confirms its long-term accumulation. The presence of areas with a long-term accumulation of SI creates a problem for the exact determination of the equilibrium line altitude in particular positions on the dome. In fact, it cannot be determined by field or remote sensing methods, except for regular measurements at ablation stakes.

Acknowledgments. *The author extends his gratitude to directorship of the Institute of Geography, Russian Academy of Sciences, and to the Russian Antarctic Expedition for the opportunity to conduct long-term monitoring of glaciers on King George (Waterloo) Island in Antarctica.*

Funding. This study was performed within the framework of state assignments of the Institute of Geography, Russian Academy of Sciences no. AAAA-A19-119022190172-5 (FMGE-2019-0004) "Glaciation and Associated Natural Processes during Climate Change".

References

Baird P.D., 1952. The glaciological studies of the Baffin Island Expedition, 1950. Part I: Method of nourishment of the Barnes Ice Cap. *J. Glaciol.* **2** (11), 2–9, 17–19.

Bazhev A.B., 1973. The role of infiltration feeding in glacier mass balance and the methods of its measurements. *Mater. Glyatsiologich. Issled.* **21**, 219–231 (in Russian).

Bazhev A.B., 1980. Methods for determining infiltration feeding of glaciers. *Mater. Glyatsiologich. Issled.* **39**, 73–81 (in Russian).

Bolshiyanov D.Y., Sokolov V.T., Yozhikov I.S. et al., 2016. Alimentation conditions and variability of glaciers of the Severnaya Zemlya Archipelago according to observations in 2014–2015. *Led i Sneg* **56** (3), 358–368 (in Russian).

Brandt O., Kohler J., Lüthje M., 2008. Spatial mapping of multiyear superimposed ice on the glacier Kongsvegen. *Svalbard. J. Glaciol.* **54** (184), 73–80.

Chernov R.A., Vasilyeva T.V., Kudikov A.V., 2015. Temperature regime of the upper layer of the Eastern Grönfjordbreen Glacier (West Spitsbergen). *Led i Sneg* **55** (3), 38–46 (in Russian).

Cogley J.G., Hock R., Rasmussen L.A. et al., 2011. *Glossary of Glacier Mass Balance and Related Terms*. IHP-VII Technical Documents in Hydrology, No. 86, IACS Contribution No. 2, UNESCO-IHP, Paris, 115 pp.

Cuffey K.M., Paterson W.S.B., 2010. *The Physics of Glaciers*. Fourth ed. Amsterdam, Academic Press, 704 pp.

Dunse T., 2011. Glacier Dynamics and Subsurface Classification of Austfonna, Svalbard: Inferences from Observations and Modeling. PhD Diss., University of Oslo, Oslo, Norway, 175 pp.

Fujita K., Seko K., Ageta Y. et al., 1996. Superimposed ice in glacier mass balance on the Tibetan Plateau. *J. Glaciol.* **42** (142), 454–460.

Gardiner M., Ellis-Evans J.C., Anderson M.G., Tranter M., 1998. Snowmelt modelling on Signy Island, South Orkney Islands. *Ann. Glaciol.* **26**, 161–166.

Gonera P., Rachlewicz G., 1997. Snow cover in the vicinity of Arctowski Station, King George Island, in winter 1991. *Polish Polar Res.* **18** (1), 3–14.

Jiankang H., Zichu X., Fengnian D., Wanchang Z., 1999. Volcanic eruptions recorded in an ice core from Collins Ice Cap, King George Island, Antarctica. *Ann. Glaciol.* **29**, 121–125.

Jonsson S., Hansson M., 1990. Identification of annual layers in superimposed ice from Storöyjokelen in northeastern Svalbard. *Geografiska Annaler* **72A**, 41–54.

Koreisha M.M., 1991. *Glaciation of the Verkhoyansk–Kolyma region. Results of the IGY Investigation*. Moscow, Interagency Geophysical Committee, 143 pp. (in Russian).

Kotlyakov V.M. (ed.), 1984. *Glaciological Glossary*. Leningrad, Gidrometeoizdat, 528 pp. (in Russian).

Mavlyudov B.R., 2008. Melting crust on Aldegonda Glacier, Spitsbergen. *Arktika i Antarktika* **40** (6), 33–54 (in Russian).

Mavlyudov B.R., 2016. Bellingshausen Dome, Antarctic. *Geography of Polar Regions. Problemy geografii* **142**, Moscow, Kodeks, pp. 629–648 (in Russian).

Mavlyudov B.R., Ananicheva M.D., 2016. Glacier dynamics in the northern massif of the Suntar-Khayata Mountains: modern conditions and dynamics from the end of the 1950s. *Led i Sneg* **56**(3), 345–357 (in Russian).

Narozhnyi Yu.K., 2001. Zones of ice formation and specificity of the structure of snow–firn deposits on Aktru glaciers. *Vestn. Tomsk. Gos. Univ.* **274**, 40–50 (in Russian).

Obleitner F., Lehning M., 2004. Measurement and simulation of snow and superimposed ice at the Kongsvegen glacier, Svalbard (Spitzbergen). *J. Geophys. Res.* **109**, D04106.

Rabus B.T., Echelmeyer K.A., 1998. The mass balance of McCall Glacier, Brooks Range, Alaska, USA; its regional relevance and implications for climate change in the Arctic. *J. Glaciol.* **44** (147), 333–351.

Rachlewicz G., 1999. Glacial relief and deposits of the western coast of Admiralty Bay, King George Island, South Shetland Islands. *Polish Polar Res.* **20** (2), 89–130.

Shumskii P.A., 1955. *Basics of Structural Ice Studies*. Moscow, Izd. Akad. Nauk SSSR, 492 pp. (in Russian).

Solovyanova I.Yu., Mavlyudov B.R., 2006. Studies of superimposed ice on glaciers of Spitsbergen. In: *Multiple Investigation of Spitsbergen Nature*. Apatity, Kola Sci. Center, Russian Acad. Sci., iss. 6, pp. 279–290 (in Russian).

URL: www.aari.aq (last visited: December 15, 2021).

Ushnurtsev S.N., Dyurgerov M.B., Xie Zichu, 1995. Role of superimposed ice in mass exchange of Tien-Shan glaciers. In: *Glaciation of Tien-Shan*. Moscow, pp. 114–120 (in Russian).

Wadham J.L., Nuttal A.-M., 2002. Multiphase formation of superimposed ice during a mass-balance year at maritime high-Arctic glacier. *J. Glaciol.* **48** (163), 545–551.

Wakahama G., Kuroiwa D., Hascmi T., Benson C.S., 1976. Field observations and experimental and theoretical studies on the superimposed ice of McCall Glacier, Alaska. *J. Glaciol.* **16** (74), 135–149.

Wang C., Cheng B., Wang K., Gerland S., Pavlova O., 2015. Modelling snow ice and superimposed ice on landfast sea ice in Kongsfjorden, Svalbard. *Polar Res.* **34**, 20828. DOI: 10.3402/polar.v34.20828.

Wen J., Kang J., Xie Z. et al., 1998. Glaciological studies on the King George Island ice cap, South Shetland Islands, Antarctica. *Ann. Glaciol.* **27**, 105–109.

Wright A., Wadham J., Siegert M. et al., 2005. Modelling the impact of superimposed ice on the mass balance of an Arctic glacier under scenarios of future climate change. *Ann. Glaciol.* **42**, 277–283.

Wright A.P., Wadham J.L., Siegert M.J. et al., 2007. Modeling the refreezing of meltwater as superimposed ice on a high Arctic glacier: A comparison of approaches. *J. Geophys. Res.* **112**, p. F04016.

Zamoruev V.V., 1972. Results of glaciological observations on Bellingshausen station in 1968. *Tr. Sovetsk. Antarktich. Ekspeditsii* **55**, 135–144 (in Russian).

Received November 22, 2021
Revised February 18, 2022
Accepted September 13, 2022

Translated by M.A. Korkka

EARTH’S CRYOSPHERE
SCIENTIFIC JOURNAL

Earth’s Cryosphere, 2022, vol. XXVI, No. 5, pp. 61–63

CHRONICLE

ALEKSEY ALEKSANDROVICH GALANIN
(*February 25, 1969–September 8, 2022*)

V.M. Lytkin[1,*], M.R. Pavlova[1], G.I. Shaposhnikov[1], A.N. Vasilieva[1], I.A. Galanina[2]

[1] *Melnikov Permafrost Institute, Siberian Branch of the Russian Academy of Sciences,*
Merzlotnaya St. 36, Yakutsk, 677010 Russia
[2] *Federal Scientific Center of the East Asia Terrestrial Biodiversity, Far East Branch of the Russian Academy of Sciences,*
pr. Stoletiya Vladivostoka 159, Vladivostok, 690022 Russia

Corresponding author; e-mail: gidro1967@mail.ru

Doctor of Geographical Sciences, chief researcher of the Laboratory of General Geocryology of the Melnikov Permafrost Institute, Siberian Branch of the Russian Academy of Sciences, Aleksey Aleksandrovich Galanin passed away on September 8, 2022. A well-known specialist in geomorphology, evolutionary geography, and paleogeographic reconstruction of periglacial landscapes of the northeast of Russia in Pleistocene and Holocene, Aleksey Galanin will be remembered as a talented researcher with lively mind, enthusiasm, and passion for science, a warm-hearted and wonderful person.

Keywords: *periglacial geomorphology, paleogeography of glacial landscapes, Quaternary geology, Northeast Russia, Aleksey Aleksandrovich Galanin.*

Recommended citation: Lytkin V.M., Pavlova M.R., Shaposhnikov G.I., Vasilieva A.N., Galanina I.A., 2022. Aleksey Aleksandrovich Galanin (February 25, 1969–September 8, 2022). *Earth’s Cryosphere* **26** (5), 61–63.

> As long as there is wind and there is motion,
> The world is full and Being flows...
> And inspiration power of mind
> Will not accept Eternity ahead of schedule.
>
> *A.A. Galanin*

Aleksey Aleksandrovich Galanin was born on February 25, 1969 in Yaroslavl in the family of a well-known geobotanist, Doctor of Biological Sciences, Professor A.V. Galanin. From childhood, thanks to his father, he learned the love of nature, the romance of field research and craving for scientific knowledge, which predetermined his future destiny. In 1986, after graduating from secondary school No. 53 in Irkutsk, he entered the geological faculty of Irkutsk State University, from which he graduated with hon-

Copyright © 2022 V.M. Lytkin, M.R. Pavlova, G.I. Shaposhnikov, A.N. Vasilieva, I.A. Galanina, All rights reserved.

ors. During student field practice, Aleksey Galanin worked in the Soil Science Laboratory of the Institute of Biological Problems of the North, Far Eastern Branch of the Russian Academy of Sciences (Magadan), where he studied the geochemistry of landscapes, soils, and certain types of vegetation in the northern Okhotsk region.

After graduating from the university in 1993, Aleksey Galanin began working in Anadyr as a junior researcher in the Laboratory of Geomorphology and Seismology of the Chukotka Research Center (branch of the North-Eastern Integrated Research Institute (SVKNII)) of the Far Eastern Branch of the Russian Academy of Sciences. During this period, Aleksey Galanin participated in the Russian-American Ecological and Geographical Expedition in eastern Chukotka to study nature and delineate the boundaries of the Bering National Park, in mapping and monitoring the pollution of the soil cover of the Kubaka gold–silver deposit, as well as in multiple research expeditions to the Koryak Uplands, Mt. Pekulney, and the Chukchi Peninsula to collect data on the dynamics of modern periglacial morphosculpture and lichenometry.

In 1996, at the invitation of the Magadan Experimental and Methodological Seismological Party of the Geophysical Service of the Russian Academy of Sciences, Aleksey Galanin participated in the restoration of the Chukotka segment of seismic stations and subsequently headed them. Since that time, Aleksey Galanin has focused his scientific interests on the study of paleogeography and the chronology of the collapse of the last glaciation, morpholithodynamics, and periglacial geomorphology. Together with specialists from the SVKNII, he proved that within the limits of the glacial relief, many of the paleoseismodislocations identified by previous studies have a different nature. They turned out to be morphosculptures of complex glacial and permafrost genesis: various types of cirque and slope rock glaciers. For their dating, he used promising methods: lichenometry, dendrochronology, and cosmic isotope analysis. The new data obtained during this period formed the basis of his PhD thesis *Lichenometric Method in the Study of Modern Geomorphological Processes in the Northeast of Russia*, which was successfully defended in 1997.

In 1997–1998, Dr. Galanin worked as the head of the Laboratory of Geology and Seismology, and then the Laboratory for the Evolution of Biogeosystems in Beringia. At the end of 1998, he transferred to the Laboratory of Neotectonics, Geomorphodynamics, and Placer Geology of the SVKNII and moved with his family to the city of Magadan, where he continued to study periglacial geomorphology, paleogeography, and climatic changes in Pleistocene and Holocene.

From that time until 2008, within the framework of various research projects, Aleksey Galanin conducted studies of the dynamics of modern glaciers and rock glaciers in the northeast of Russia using lichenometric and radiocarbon data, studied the issues of the paleoclimate of Arctic lakes and estuaries within the framework of the International PALE project. He took part in the environmental support of various mining and geological works at the gold deposits of the Magadan region (Kubaka, Birkachan, Julietta, Matrosov mines), Chukotka Autonomous Okrug (Kupol, Maiskoye) and Yamalo-Nenets Autonomous Okrug (Ray-Iz massif); he also studied seismic hazard of the eastern part of the Chukotka Peninsula and its settlements. The original data obtained by Galanin made it possible to establish signs of the active impact of seismicity on glacial morphosculpture and to identify new morphodynamic types of formations.

Under the leadership of Dr. Galanin two candidate dissertations were prepared: *Climate and Vegetation of the Anadyr Plateau over the Last 350 Thousand Years (Palynological Characteristics of the Sediments of Lake Elgygytgyn)* by T.V. Matrosova and *Composition, Structure, and Temperature Regime of Freezing Rock Dumps and the Possibility of Their Evolution into Rock Glaciers (on the Example of the Omolon Massif, Magadan region)* by O.V. Motorov. These works were successfully defended at the Institute of Geography of the Russian Academy of Sciences (Moscow) and the Melnikov Permafrost Institute, Siberian Branch of the Russian Academy of Sciences (Yakutsk).

In 2009, Aleksey Aleksandrovich Galanin defended his doctoral thesis *Rock Glaciers of the Northeast of Russia: Structure, Genesis, Age, Geographical Analysis* at the Pacific Geographical Institute, Far Eastern Branch of the Russian Academy of Sciences. In his dissertation, the results of field observations of these formations in various mountain structures of the northeast of Russia were presented; sections were investigated; data on age and modern dynamics were obtained; a geographical analysis of these formations was carried out using geoinformatics and mathematical statistics; spatial and genetic relationships of rock glaciers with relief, climate, Pleistocene glaciations, recent tectonics and modern seismicity were identified and quantitatively characterized. For the first time, a geoinformation system on rock glaciers was developed and their classification based on the integration of paleogeographic and geomorphological data was suggested; their age and history of formation in the region were characterized.

In 2011, Dr. Galanin was invited to the position of the head of the Laboratory of Regional Geocryology and Cryolithology of the Melnikov Permafrost Institute, Siberian Branch of the Russian Academy of Sciences in Yakutsk. He continued to study the issues of periglacial geomorphology of the Suntar-Khayata, Zailiyskiy Alatau and Severo-Chuyskiy ridges. Based on the results of their comprehensive study, Aleksey Galanin proposed a completely new mechanism for the movement of Tien Shan rock glaciers; new data on glaciation of the Suntar-Khayata Range in the

Little Ice Age were obtained, and rock glaciers in this region were mapped. The materials of these studies formed the basis of V.M. Lytkin's dissertation *Dynamics of Glaciers and Rock Glaciers of the Suntar-Khayata Range in the Late Holocene*, which was defended under the supervision of Dr. Galanin in 2016.

Since 2012, Aleksey Galanin has been studying the Late Quaternary eolian deposits of Central Yakutia. He led a number of joint research expeditions in the lower reaches of the Vilyui River, where a new reference section of cover dune deposits – the Kysyl-Syr tukulan – was discovered and thoroughly investigated. He studied in detail a number of outcrops and Late Quaternary sand massifs in the middle reaches of the Lena River (Sandy Mountain, Ust-Buotamskoye, Kharyyalakhskoye, Meginskoye), thanks to which phenomenal features of the structure, permafrost-hydrogeological conditions, geomorphology and paleogeography of Late Quaternary dune formations in this area were established. Significant emphasis in these studies was placed on obtaining data on the age of deposits by radiocarbon dating. This work was carried out under the supervision of Dr. Galanin in the Radiocarbon Laboratory of the Melnikov Permafrost Institute. The original materials obtained at the beginning of these studies became the basis of A.A. Kut dissertation *Eolian Permafrost Formations (Tukulans) of Central Yakutia: Structure, Genesis, Age, Patterns of Distribution,* successfully defended under the guidance of Dr. Galanin in 2014 at the Melnikov Permafrost Institute.

During his entire creative career, Aleksey Galanin published 260 scientific works; he was the author and coauthor of six monographs: *Lichenometric Studies in the Northeast of Russia* (1995); *Nature and Resources of Chukotka* (1997); *Lichenometry: Current State and Directions of Development of the Method (Analytical Review)* (2002); *Landscapes, Climate and Natural Resources of the Taui Bay of the Sea of Okhotsk* (2006); *River Systems of the Russian Far East: Quarter of Century of Research* (2015); *Where Should I Go to Get to Know Russia. Book II* (2017). Dr. Galanin supervised 15 research grants. He was a member of the Dissertation Council of the Melnikov Permafrost Institute, Siberian Branch of the Russian Academy of Sciences; the Joint Scientific Council on Earth Sciences of the Yakutsk Science Center, Siberian Branch of the Russian Academy of Sciences; the Presidium of the Association of Geomorphologists of Russia; an expert of the Russian Foundation for Basic Research and Federal Research Programs in the field of paleogeography and geomorphology.

Aleksey Aleksandrovich Galanin was a talented scientist, friend and teacher of young researchers. He will remain in our hearts as a bright wonderful person!

Received October 10, 2022

Translated by A.V. Muravyev